A Novel Apparatus Design, Experimental Methods and Validation for Temperature Controlled Directional Crystallization of High-Pressure Gas Hydrate Systems

Conception d'un réacteur novateur, méthodes expérimentaux et validation pour la cristallisation dirigée d'hydrates gazeux à haute pression

A Thesis Submitted to the Division of Graduate Studies
of the Royal Military College of Canada
by

James Robert DuQuesnay

In partial fulfillment of the requirements of the degree of
Master of Applied Science in Chemical Engineering

December 2014

Acknowledgements

I would like to express my gratitude to my supervisor Juan Beltran for the guidance and excellent advice through the learning process of this master's thesis. I would like to thank Clarence McEwen, Brent Ball and Dave Twigg for all their help in fabricating and setting up the apparatus. I am grateful to my parents for their love and support. Finally, I would like to thank Kiah for all her love, kindness and support.

Abstract

A novel, high-pressure, bilateral temperature control stage (HP-BTCS) was developed to study gas hydrate growth and dissociation. The design allowed for tight control of the crystallization substrate temperature, independent of the ambient conditions. Using the HP-BTCS, methane hydrate formation was investigated on a surface with a uniform temperature and on a surface with a constant temperature gradient. The uniform temperature experiments showed a previously unreported transition point in methane hydrate morphology and displayed closely reproducible film morphologies. A single temperature-gradient experiment showed transitions in morphology with respect to driving force. These transitions were found to be consistently reproducible, and occurred due to a change from continuous crystal growth to polycrystalline adhesive type growth. The temperature gradient was also used to control solid-liquid interface position during gas hydrate dissociation. The controlled dissociation allowed for stationary observations of hydrate-liquid-vapour (H-L-V) equilibrium, providing a simple and fast method for phase equilibrium measurements. The temperature gradient was used to correlate film velocity (apparent growth kinetics) and supercooling. Thus, the ability to observe gas hydrate growth on tightly controlled temperature gradients was found to reduce multi-trial methods to a single experiment that: (1) quantifies morphology/growth mechanism transitions with respect to temperature, (2) measures the H-L-V equilibrium temperature at the experimental pressure, and (3) correlates the apparent kinetics with respect to temperature. This could provide a quick way to screen the agglomeration, thermodynamic and kinetic effects of a potential hydrate inhibitor/promoter.

Résumé

Une nouvelle platine avec contrôle bilatérale de la température à haute pression, (PCBT-HP) a été conçue pour étudier la croissance des hydrates de gaz ainsi que leur dissociation. Le concept innovateur a permis un contrôle strict de la température du substrat de cristallisation, indépendamment des conditions ambiantes. En utilisant la PCBT-HP, la formation d'hydrate de méthane a été étudiée sur une surface avec une température de surface uniforme et sur une surface avec un gradient de température constant. Les expériences de température uniformes ont montré un point de transition précédemment non déclarées dans la morphologie de l'hydrate de méthane et ils sont affichés des morphologies de films étroitement reproductibles. Une seule expérience avec un gradient de température a permis de monter transitions dans la morphologie par rapport à la force d'entrainement. Ces transitions sont avérées être toujours reproductibles et ils se sont produites en raison d'un changement de croissance des cristaux continue à une croissance polycristalline de type adhésif. Le gradient de température a également été utilisé pour contrôler la position de l'interface solide-liquide au cours de la dissociation des hydrates gazeux. Le réglage de la dissociation a permis des observations stationnaires de l'équilibre hydrate-liquide-vapeur (HLV), fournissant une méthode simple et rapide pour les mesures d'équilibre de phase. Le gradient de température a été utilisé pour établir une corrélation entre la vitesse du film (cinétique de croissance apparente) et le sur-refroidissement. Ainsi, la capacité d'observer la croissance des hydrates de gaz sur des gradients de température étroitement contrôlés réduit les méthodes multi-essais à une seule expérience qui : (1) quantifie les transitions morphologie/mécanisme de croissance par rapport à la température, (2) mesure la température d'équilibre HLV à la pression expérimentale et (3) corrèle la cinétique apparente en fonction de la température. Cela pourrait fournir un moyen rapide pour dépister l'agglomération, ainsi que les effets thermodynamiques et cinétiques d'un potentiel inhibiteur / promoteur des hydrates gazeux.

Contents

List of Tables

List of Figures

Chapter 1

Introduction

Gas hydrates (abbreviated as hydrates) are crystalline compounds composed of hydrogen bonded water cages enclosing small guest molecules. Hydrates typically form at high pressures and low temperatures.

In industry, inhibiting gas hydrate plug formation in oil and gas pipelines represents a significant cost associated with fossil fuel production. An estimated $220 million USD is spent per year worldwide just on 'production chemicals', such as methanol or glycols, to prevent hydrate plug formation (Sloan, 2003). These additives are known as thermodynamic hydrate inhibitors and they require generally high concentrations (20 – 50 wt %) to function. As such, there is a demand for alternative, more cost effective hydrate inhibitors. Recent research in this area has focused on low dosage (0.1 – 1 wt % in the aqueous phase) hydrate inhibitors, such as anti-agglomerates and kinetic inhibitors (Kelland, 2006).

In nature, hydrates of natural gas are abundant in oceanic and permafrost regions. Conservative estimates of the energy stored as naturally occurring gas hydrates are twice that of all other fossil fuels combined (Koh *et al.*, 2012). These reserves represent a significant source of unconventional fossil fuel. As well, there are environmental concerns due to the potential of these hydrates to destabilize and release large quantities of methane into the atmosphere. In both oceanic and arctic regions, the hydrates form within a host sediment. Interactions between the hydrate and the sediment particles are studied to better understand hydrate formation, dissociation and stability for practical hydrate applications (*e.g.*, drilling for the natural gas and sequestering carbon dioxide as a hydrate).

The effects of a hydrate inhibitor, as well as, the interactions between hydrate and sediment depend significantly on the driving force for formation. For example, at high driving forces, kinetic inhibitors typically lose their effectiveness and at low driving forces, anti-agglomerate/hydrate slurries become too viscous to properly flow through pipelines (Kelland, 2006). The growth velocity of a hydrate is also dependent on the driving force. As with other crystallizing systems within sediment (*e.g.*, ice), crystallizing hydrates at low velocities can reject and push foreign particles. At sufficiently high growth velocities, the foreign particles will always be engulfed by the advancing crystal front (Uhlmann *et al.*, 1964). Research in both hydrate prevention and hydrate recovery applications benefit greatly from precise control of the conditions at formation (and therefore precise control of driving force).

Observations of hydrate growth provide a picture of the events that occur upon hydrate formation. This can lead to insights into how certain inhibitors function or characterize hydrate interactions with foreign particles. These sorts of measurements can aid in the development of appropriate hydrate growth models.

Morphology hydrate reactors are often used to assess the effect of driving force on hydrate morphology (Servio and Englezos, 2003a; Tanaka *et al.*, 2009; Beltran and Servio, 2010) and to measure apparent growth kinetics through hydrate film velocity (Freer *et al.*, 2001; Taylor *et al.*, 2007; Peng *et al.*, 2007; Kitamura and Mori, 2013; Li *et al.*, 2014). In general, these reactor designs consist of a pressurized sample cell, with temperature control via a coolant jacket or bath. This type of design offers little control over crystal growth beyond the target conditions at hydrate formation.

One means of controlling crystal growth is directional crystallization (or directional solidification). Current methods involve a motor that pulls a sample slide across a directional crystallization stage. The stage applies a thermal gradient across the sample using two constant temperature plates spaced apart such that the thermal gradient is constant over the gap. The temperature is set above and below solid-liquid equilibrium at either end of the gap. The solid-liquid interface must remain at some position between the two plates. Dragging the sample across the plates (toward the colder plate) results in crystallization of the sample at a rate equivalent to the pulling velocity; however, this type of apparatus is limited to low pressure experiments due to the moving parts required for velocity control. As such, research in this area has been limited to ice and hydrates that can form at atmospheric pressure (*e.g.*, tetrahydrofuran hydrates) (Muraoka and Nagashima, 2012).

The objective of this work was to design an observation vessel that can perform directional crystallization and other temperature-controlled experiments for high-pressure gas hydrate systems. The design was assessed by observing methane hydrate formation on water droplets with a controlled temperature gradient at constant pressure.

Chapter 2

Background

Gas hydrates − also known as clathrate hydrates − are crystalline compounds composed of hydrogen bonded water cages enclosing small guest molecules. Gas hydrates typically form at low temperatures and high pressures. They differ from other hydrates in that there is no chemical bond between the water molecules and the molecule being hydrated. Clathrate hydrates are known to be non-stoichiometric, due to the occurrence of unoccupied cages. Clathrate hydrate composition varies with temperature, pressure and fluid phase composition. The hydration number for a gas hydrate refers to the number of water molecules per guest molecule. Since clathrate hydrates mainly consist of water molecules, their physical properties are often compared with those of water and ice.

Natural gas hydrates are known to form plugs in oil and gas pipelines and are a major problem in deep ocean drilling. The most common inhibitors used by industry are methanol, electrolytes and glycols. Compounds for gas hydrate prevention are categorized into either thermodynamic inhibitors, kinetic inhibitors or anti-agglomerants.

Natural gas hydrates occur in large quantities in ocean sediment and, to a lesser extent, in arctic permafrost regions. It is estimated that the amount of energy stored in gas hydrates is twice that of all other fossil fuels combined Koh *et al.* (2012). Each volume of hydrate can contain up to 180 volumes of gas at STP. Dissociation of naturally-occurring methane hydrates as a result of warming oceans could therefore have a significant impact on climate change.

Table 2.1 – Size ranges for hydrate guests of a given structure (adapted from Sloan and Koh (2008)).

Structure	Molecular diameters of guests	Guest examples
sI	4.2 Å $< d <$ 6 Å	methane, carbon dioxide, ethane
sII	$d <$ 4.2 Å	nitrogen, hydrogen
	6 Å $< d <$ 7 Å	propane, iso butane
sH	7 Å $< d <$ 9 Å	isopentane, neohexane

Note: sH also requires a small molecule, such as methane, to be stable.

2.1 Crystal Structure of Gas Hydrates

The common crystal structures of clathrate hydrates are structure I (sI, primitive cubic), structure II (sII, face centred cubic) and structure H (sH, hexagonal). All three structures consist of about 85% water on a molecular basis (Sloan, 2003). Table 2.1 shows the size range of guest molecules for each of the common structures. These structures are made up of hydrogen bonded water cavities. A regular pentagonal dodecahedron (5^{12}) cage is the smallest cage and is common to all three structures. All three structures have small and large cages, though structure H also has a medium size cage. Structure H requires both a large guest and a small guest. The large guest occupies the largest cavity and the small guest occupies the small and medium sized cavities to stabilize the large cavity. Hydrate guests can multiply occupy a hydrate cavity, typically at very high pressures (*e.g.*, hydrogen in a structure II hydrate) (Ripmeester *et al.*, 1987).

2.2 Phase Equilibria of Gas Hydrates

Figure 2.1 is a schematic of a pressure-temperature phase diagram for a carbon dioxide and water system. Following Gibbs' Phase Rule for this system: two phases in equilibrium are represented as an area, a line represents three phases in equilibrium and a point represents four phases in equilibrium. Only two intensive variables (p and T) are needed to specify the system. For more complex systems, composition is added as the third axis. Hydrates will form in the region to the left of the I-H-V (Ice - Hydrate - CO_2 Vapour), L_W-H-

V (Liquid Water - Hydrate - CO_2 Vapour) and L_W-H-L_{HC} (Liquid Water - Hydrate - Liquid CO_2) lines.

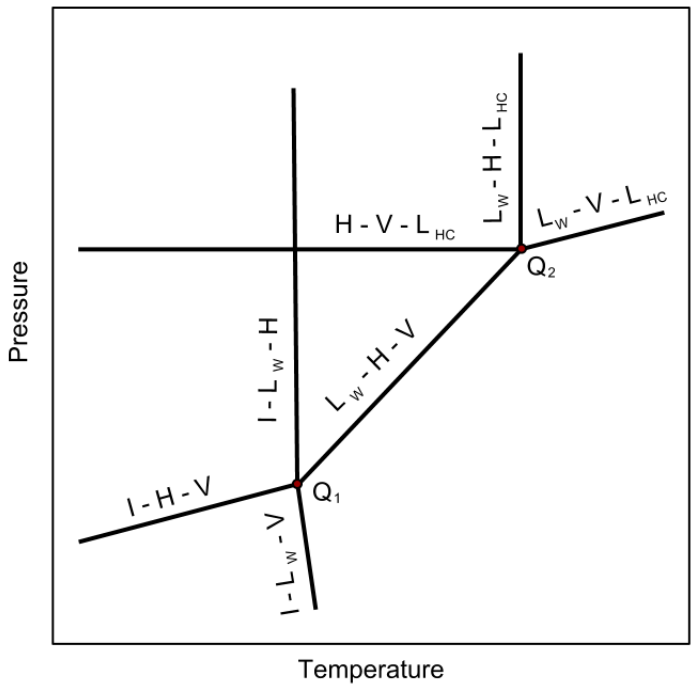

Figure 2.1 − Pressure-temperature phase diagram for a carbon dioxide + water system (Sloan and Koh, 2008).

Points Q_1 and Q_2 in Figure 2.1 are the quadruple points where four phases exist. The temperature for Q_1 is approximately 273 K for all hydrate formers and pressures vary widely among hydrate formers. The phases present in regions between three-phase lines are those in common with the lines bounding the region. For example, the area between the I-L_W-H and L_W-H-V lines is the L_W-H. Similarly, I-H is the region between the I-L_W-H and I-H-V lines and V-H is the region between I-H-V and L_W-H-V. In Figure 2.1 these regions appear to overlap. This is because the regions have been projected onto the two-dimensional plot. In reality the three-phase lines are not all on the same plane, with the third dimension being composition (Song *et al.*, 1987).

The addition of thermodynamic inhibitors (e.g., electrolytes or alcohols) to the system shifts the L_W-H-V and I-L_W-V lines to the left. There is also a drop in the temperature and pressure of Q_1 (corresponding to a lower freezing point of the inhibitor-water mixture) (Englezos and Bishnoi, 1988).

2.3 Hydrate Formation and Dissociation Processes

2.3.1 Hydrate Formation Kinetics

The time-dependent hydrate phenomena occur in three main areas: nucleation, growth and dissociation. One method for the time-dependent study of hydrates is the measurement of gas consumption versus time. Hydrates are formed in a pressurized sample of water. Gas is fed from a reservoir to maintain constant pressure in the growth cell as hydrates are formed. The change in pressure of the reservoir over time is then related to moles of gas consumed by an equation of state. Figure 2.2 shows the gas consumption profile over time for this type of experiment.

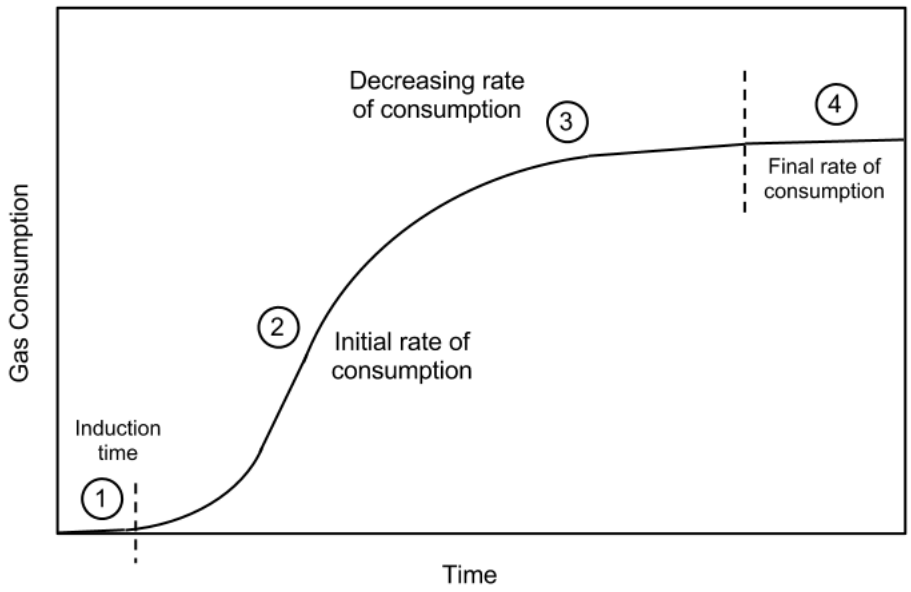

Figure 2.2 – Gas consumption versus time for hydrate formation. (adapted from Lederhos *et al.* (1996))

The first section in Figure 2.2 corresponds to the induction time. This is the time required until macroscopically visible crystals are formed or a detectable amount of gas has been consumed. This region is dominated by hydrate nucleation, a process that is not observable by macroscopic measurements. The temperature and pressure during induction are within the hydrate stability region. However, the non-equilibrium state is still present in the system due

to metastability. Induction is followed by rapid hydrate growth. This change is known as the turbidity point. The clathrated guest molecules are packed at a higher density than those in the gas phase resulting in an observable consumption of gas. The hydrate growth rate then levels off due to mass transfer limitations.

2.3.2 Hydrate Nucleation

During hydrate nucleation, guest and water molecule clusters arrange and disperse until a critical size for continued growth is reached. A supersaturated solution is one where the concentration of solute is greater than the equilibrium solubility for a given set of conditions. At higher degrees of supersaturation there will be more crystal nuclei Mullin (2001). Miers and Isaac (1907) proved that there is a limit to metastability for a given solute-solvent mixture called the thermodynamic spinodal. Typically, hydrate nucleation will occur before this limit is reached (in the metastable region). Crystallization will occur once the spinodal region is reached. Figure 2.3 is a schematic of a pressure versus temperature phase diagram for a gas hydrate. Hydrates will not form in the area to the right of the H-L-V line. To the left of the H-L-V line is the supersaturated metastable zone, where hydrates are likely to form. Further to the left is the spinodal (or labile) region, where hydrate crystals will form spontaneously.

Site of Nucleation

Long and Sloan (1996) found that hydrates will preferentially form at the gas-water interface. This occurs because of the large concentration gradient at the interface. The water mole fraction in the gas phase is typically around 0.05 and the mole fraction of guest in the water phase is lower than 0.001. The low concentration of either the guest or the host in the bulk phases means that critical nuclei are unlikely; however, at the interface there is a large concentration of both host and guest which makes the formation of a crystal of critical size more likely.

Stochastic Nucleation

Hydrate nucleation is stochastic. Given a set of conditions, there is no definite value for the time from nucleation until hydrate formation can be detected.

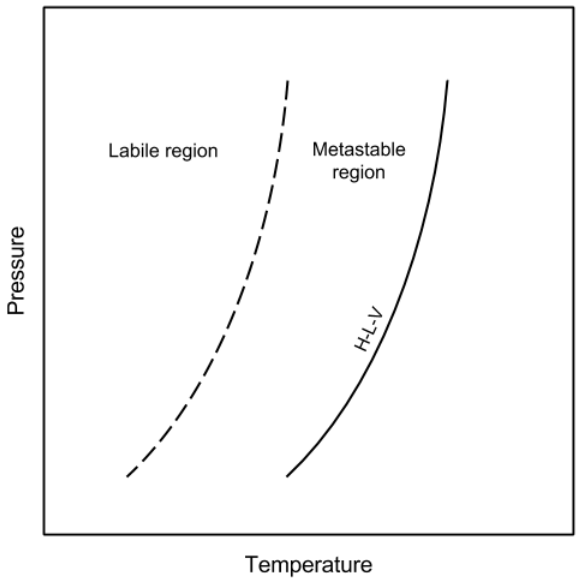

Figure 2.3 – Partial hydrate phase diagram showing the H-L-V line (solid line) and spinodal line (dashed line) (Sloan and Koh, 2008).

This probability distribution is wider (higher variance) in the metastable region to the left of the H-L-V in Figure 2.3 and becomes more narrow (lower variance) past the spinodal line.

An automated lag-time apparatus (ALTA) was used by Wilson *et al.* (2005) to obtain a distribution of supercooling point data for tetrahydrofuran hydrate formation. The ALTA works by continually freezing and melting a single water sample upwards of 300 times. This generates a statistically significant data set for the supercooling point for tetrahydrofuran hydrate formation. More recently, Wilson and coworkers developed a high pressure version of the ALTA (HP-ALTA) (Maeda *et al.*, 2011). This HP-ALTA would now be able to perform the same sorts of measurements of nucleation with the formation of gas hydrates from water at high pressures.

Studies have found that hydrate induction times have a wider distrubition when the water sample is held at a constant temperature (Ohmura *et al.*, 2003). There is a noticeably narrower induction time distribution for samples formed under a constant cooling rate (Wilson *et al.*, 2005).

Table 2.2 – Various representations of the driving force for nucleation (reproduced from Sloan and Koh (2008)).

Investigators	Year	Driving Force Metric
Vysniauskas and Bishnoi	1983	$T^{eq} - T^{exp}$
Skovborg and Rasmussen	1992	$\mu_{WH}^{exp} - \mu_{WL}^{exp}$
Natarajan et al.	1994	$f_i^{exp}/f_i^{eq} - 1$
Christiansen and Sloan	1995	Δg^{exp}
Kashchiev and Firoozabadi	2002	$\Delta\mu$, supersaturation
Anklam and Firoozabadi	2004	Δg
Arjmandi et al.	2005	$T^{eq} - T^{exp}$

Driving Force for Nucleation

There have been a number of different measures used for the driving force for hydrate nucleation. They are summarized in Table 2.2. The general case driving force that incorporates all of these driving forces is the total molar change in Gibbs energy of hydrate formation, ΔG (Christiansen and Sloan, 1994).

Arjmandi *et al.* (2005) investigated the effect of pressure on the driving force and the relationship between supercooling and driving force using the equations from the authors in Table 2.2. Using a methane-water system, the supercooling was found to be proportional to driving force. At constant supercooling, the driving force was found to decrease with increasing pressure.

The Memory Effect

The 'memory effect' refers to the phenomenon that hydrates retain a memory of their structure for a short period after dissociation. Researchers have noted that hydrates form more readily from gas and water dissociated from a hydrate compared to water without hydrate history (Makogon, 1981; Servio and Englezos, 2003b). This phenomenon is not observed when the system is heated sufficiently above the hydrate formation conditions. Hypotheses on why this occurs centre around hydrate structure (Makogon, 1981; Buchanan *et al.*, 2005) or dissolved gas (Rodger, 2000) remaining in solution.

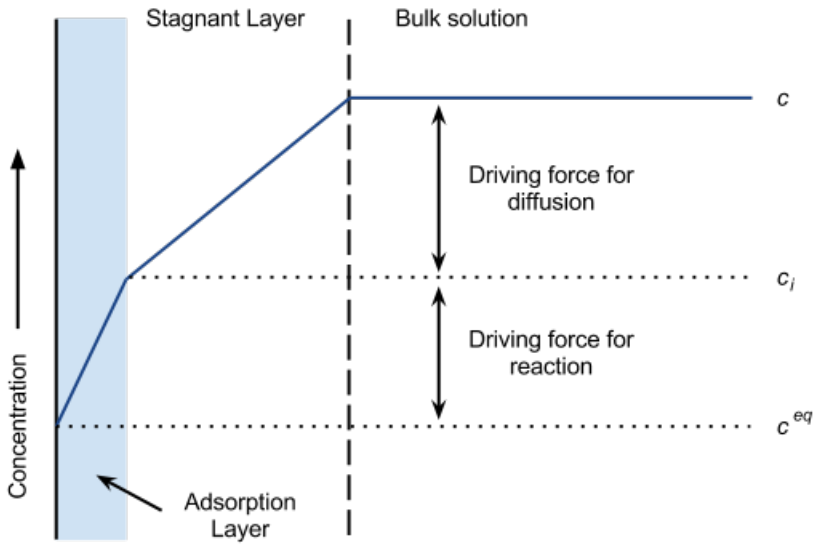

Figure 2.4 – Mass transfer model for the diffusion of gas from the bulk phase to the crystal interface (reproduced from Sloan and Koh (2008)).

2.3.3 Hydrate Growth

After the stochastic nucleation of hydrate crystals, there is a period of continual hydrate propagation where heat and mass transfer become major contributors. As the hydrate grows, gas is being incorporated into the hydrate phase. The gas fraction in the hydrate phase is typically greater than the solubility of the gas in water. Therefore, mass transfer to the hydrate surface can be one of the rate limiting factors. As well, solidification is an exothermic process, so heat can also control the rate of growth.

Mass Transfer Boundary Layer

The transport of gas through the bulk phases to the crystal surface can be expressed as a diffusional boundary layer problem. The crystal growth rate is controlled by two steps: (1) diffusion to the interface and (2) reaction at the interface. This boundary layer model is graphically represented in Figure 2.4.

Hydrate Crystal Growth

Hydrate growth processes fall into three main categories: (1) single crystal growth, (2) hydrate film growth and (3) multiple crystal growth in an agitated system.

Single crystal processes are commonly used to study the effects of additives on crystal growth and morphology. As well, single crystals are required for X-ray and neutron diffraction in structural analysis.

Film growth processes at the guest-water interface provide insight into hydrate growth mechanisms. These mechanisms can then be applied to hydrate growth models. In the past, studies in this area have found that − for guests that form the same crystal structure (*e.g.*, sI) − hydrate morphology generally does not depend on the guest and that the driving force affects the morphology (Servio and Englezos, 2003a, 2003b); however, Decarie (2012) observed significantly different morphologies for carbon dioxide hydrates compared to methane hydrates, which are both sI hydrate formers. Servio and Englezos performed film growth experiments for carbon dioxide and methane hydrates from water droplets. The general mechanism observed for the film growth is: (1) Formation of hydrate layer and dendrites, (2) Dendrites collapse onto the hydrate layer and (3) Depressions form in the hydrate surface. High driving force experiments resulted in a rough morphology with needle-like dendrites extruding from the hydrate surface. The low driving force experiments resulted in a much smoother morphology with growth occurring slowly across the droplet surface. The appearance of the depressions in the hydrate surface is most likely due to the interior of the droplet reducing in volume when the liquid water is converted into hydrate. Microimaging studies have shown that film thickening is limited by gas diffusion though the hydrate layer (Moudrakovski *et al.*, 2004).

Crystal growth with surface agitation experiments typically measure gas consumption over time during hydrate formation. Studies with this type of process measure intrinsic and apparent hydrate kinetics (Englezos *et al.*, 1987; Englezos and Bishnoi, 1988; Clarke and Bishnoi, 2005) and compare the effects of electrolytes, kinetic inhibitors and anti-agglomerates.

Correlations for Hydrate Growth

There are three main correlations for hydrate growth: (1) intrinsic growth kinetics, (2) mass transfer, and (3) heat transfer. On larger scales, intrinsic

kinetics play a much smaller role than heat and mass transfer in hydrate growth.

Most heat transfer models for hydrate growth are based on a lateral growth mechanism. The most common model is by Mochizuki and Mori (2006), which is a transient two-dimensional conductive heat transfer model. Heat is transferred from the hydrate film to the gas and liquid phases. This is shown graphically in Figure 2.5. The thick black line is the hydrate forming site. This is where the heat is generated and the temperature is equal to the triple point.

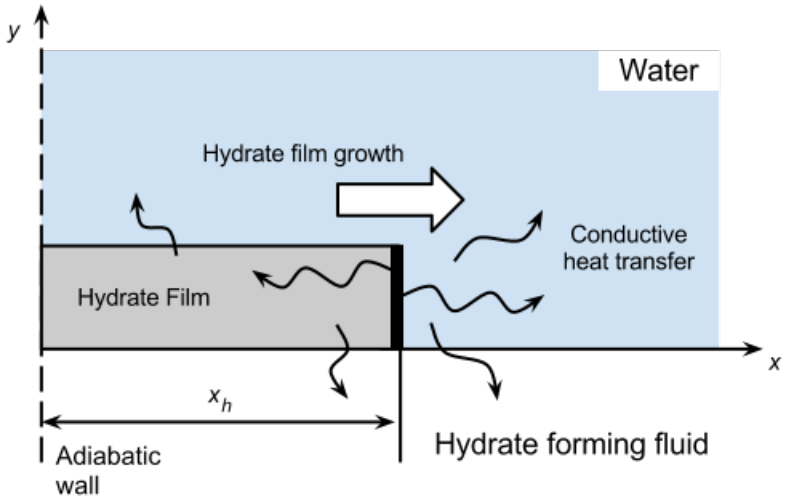

Figure 2.5 – Hydrate film heat transfer model (Mochizuki and Mori, 2006).

2.3.4 Hydrate Dissociation

Hydrate dissociation is an endothermic process controlled by heat transfer. The hydrate guest's solubility in water is an important factor in hydrate dissociation rate, with more soluble guests dissociating faster (Rehder *et al.*, 2004). Hydrates are known to be capable of 'self-preservation'. This is the phenomenon where methane or carbon dioxide (sI) hydrates remain stable at atmospheric pressure for extended periods of time (Davidson *et al.*, 1986). This 'self-preservation' has been found not to occur for sII hydrates (Stern *et al.*, 2003).

2.4 Hydrates in Industry

The primary concern with hydrates in industry is flow assurance in oil and gas pipelines because hydrate plugs have a major economic impact on the operation of oil and gas pipelines.

2.4.1 Flow Assurance

For hydrate plugs to form, there must be a hydrate guest and water in the pipeline. Also, temperature and pressure must be within the hydrate equilibrium region. Hydrate formation commonly occurs when water rich gas is throttled (cooling by adiabatic expansion) through an orifice or valve. Pipelines are designed so that they do not allow hydrate formation under normal operation through the addition of inhibitors and upstream dehydration. Regular thermodynamic inhibitors, like methanol, are injected during operation only for gas dominated systems. Oil dominated systems have a higher heat capacity, so they can usually maintain temperatures that do not permit hydrate formation (Zerpa *et al.*, 2012).

Hydrate Formation in Oil Dominated Systems

Water is emulsified in the oil phase, with a droplet size in the order of 10 μm (Turner *et al.*, 2009). Thin hydrate shells grow around the water droplets from gas molecules dissolved in the oil phase. Further thickening is a very slow process (in the order of days) due to diffusion restrictions. Capillary forces of attraction cause the hydrate shells to agglomerate. The effective viscosity of the mixture and the pressure drop across the forming hydrate increase. The hydrate mass accumulates until the plug is fully formed and the flow is shut in (Davies *et al.*, 2010). The plug then solidifies further. This formation mechanism is shown in Figure 2.6.

Hydrate Formation in Gas Dominated Systems

Hydrates form at the walls of the pipe via deposition from water vapour. This is a result of heat transfer from the pipe to the colder surroundings. The deposited hydrate layer becomes thicker and the annulus formed is generally non-concentric with the pipe. The pressure drop past the annulus is increased. As fluid passes through the annulus some of the hydrate is sloughed away.

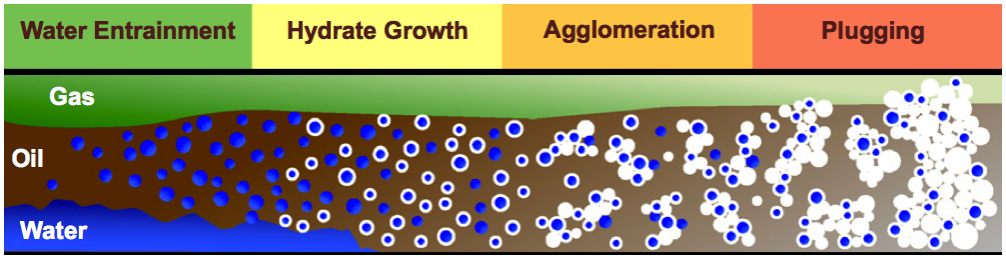

Figure 2.6 – Hydrate plug formation mechanism in oil dominated systems (reproduced from Zerpa *et al.* (2012)).

Down stream these particles can accumulate into a plug (Zerpa *et al.*, 2012). This formation mechanism is shown in Figure 2.7.

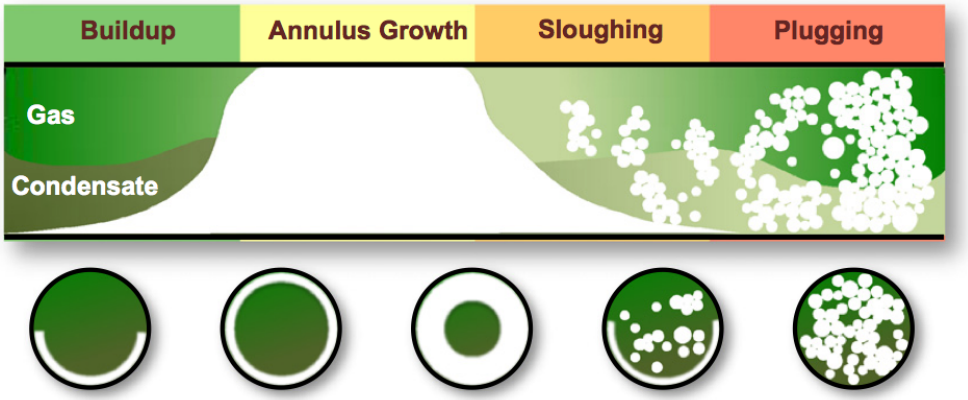

Figure 2.7 – Hydrate plug formation mechanism in gas dominated systems (reproduced from Zerpa *et al.* (2012)).

Alternative Plug Prevention

The standard method for hydrate inhibition is to inject thermodynamic inhibitors like methanol and glycols. Their inhibition mechanism was described in section 2.2. Yousif (1998) reported that systems that were under-inhibited with methanol could actually promote hydrate growth. This finding was confirmed for both laboratory and field studies. Pipeline plugging is worse for under-inhibited systems than for systems with no thermodynamic inhibitors added.

Generally large volumes of thermodynamic inhibitors (20 – 50 wt %) are required to prevent hydrate formation (Kelland, 2006). The cost and additional volume to pump make thermodynamic inhibitors an expensive part of pipeline operation. There are two main alternatives to thermodynamic inhibitors: kinetic inhibitors and anti-agglomerates.

Kinetic inhibitors are low molecular weight polymers dissolved in a carrier solvent. These inhibitors bond to the hydrate surface and slow further propagation. They have been found to be active at significantly lower concentrations (0.1 – 1.0 wt %) than thermodynamic inhibitors. However, they are generally only effective when supercooling is below 10 K (Kelland, 2006).

Anti-agglomerates (AAs) prevent hydrate cluster accumulation in oil-dominated systems at low concentrations ($<$ 1 wt%). They are surfactants (i.e. they reduce hydrate cluster adhesive forces) that provide stable water in oil emulsions. A typical AA is a quaternary ammonium salt where two to three of the branches are short (e.g., C4 ammonium) and one to two of the branches are long (e.g., C8 to C18 ammonium). A short branch acts as a candidate for hydrate inclusion and a long branch allows for solubility in the oil phase (Xu *et al.*, 2007).

2.4.2 Gas Hydrate Technology

Clathrate hydrates have been suggested as a means of gas storage and transport. For natural gas, the energy density for gas hydrates lies between that of a gas and a liquid. However, the conditions required for gas hydrate storage are much milder than liquefied natural gas and have been found to be more economical (Gudmundsson and Borrehaug, 1996). Storage methods have also been proposed for hydrogen gas with high pressure (Dyadin *et al.*, 1999), multiple occupancy (Mao *et al.*, 2002) and tetrahydrofuran and hydrogen mixed hydrate (Florusse *et al.*, 2004) methods. Hydrates have also been used as a separation mechanism for purifying gasses (e.g., sulfur dioxide) (Eslamimanesh *et al.*, 2011) or sequestering combustion products (e.g. carbon dioxide and hydration sulfide) (Kang and Lee, 2000; Yamamoto *et al.*, 2002; Park *et al.*, 2006).

2.5 Hydrates in Nature

Gas hydrates of methane are abundant in oceanic sediment and arctic permafrost locations where both methane and water are present at low temperatures and high pressures. The amount of methane gas stored in hydrates is estimated to be twice that of all other fossil fuel sources combined (Koh *et al.*, 2012). Hydrates in nature represent a significant source of unconventional fuel, have the potential to impact climate change and are possible geological hazards.

2.5.1 Occurrence of Hydrates in Nature

Knowledge of hydrate deposit locations is incomplete and is obtained by direct (core sampling) and indirect (bottom simulating reflectors) evidence. The initial estimate of the amount of methane gas stored as hydrate was 3.053×10^{18} m^3 (STP) (Trofimuk *et al.*, 1973) Subsequent estimates became progressively lower to values of 1.2×10^{17} m^3 (STP) by Klauda and Sandler (2005) and 2×10^{14} m^3 (STP) by Soloviev (2002). Regardless, even the lowest estimate is significantly larger than the estimates for conventional gas reserves (1.5×10^{14} m^3 (Radler, 2000)). Kvenvolden (2002) stated that with current natural gas hydrate estimates, the amount of methane stored in hydrates is twice that of the methane equivalent of all other fossil fuels combined. Since hydrates take a long time to form, they should not be considered a renewable resource. Figure 2.8 is a map indicating all of the known hydrate deposits.

2.5.2 Hydrate Formation

Methane availability limits hydrate growth in reserves. More than 99% of the methane in these reserves is biogenetic (bacterially generated). Conventional methane gas reservoirs consist mainly of thermogenic methane (Hester and Brewer, 2009).

Thermogenic hydrates form from faults that channel the methane from its (high temperature) source. Biogenic hydrates are more dispersed in coarse sediment. Malone (1985) categorized hydrates into four main categories: Disseminated (the most common type of deposit), nodular (deposits up to 5 cm in diameter), layered (layers of hydrate and sediment) and massive (as thick as 3-4 m and greater than 95% hydrate). Biogenic hydrates tend to be the disseminated type and thermogenic hydrates tend to be the massive type.

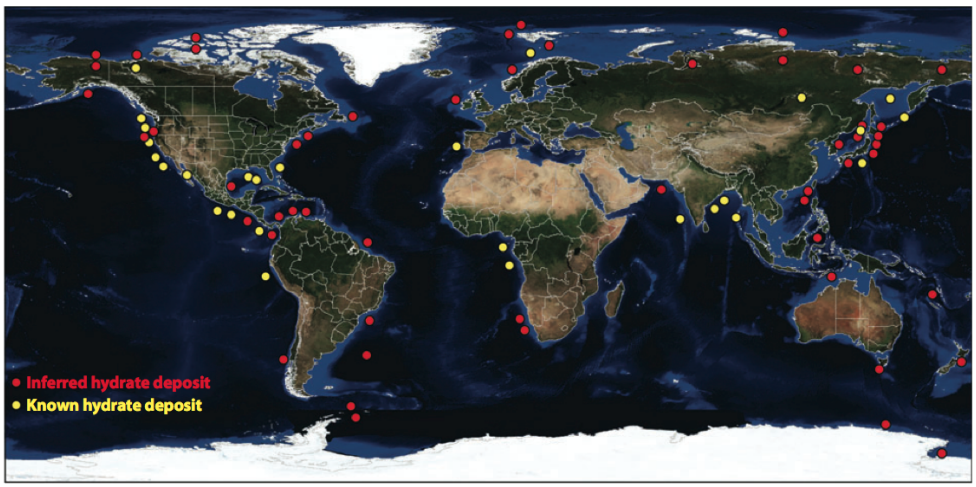

Figure 2.8 – Inferred and recovered hydrate locations in the world (reproduced from Hester and Brewer (2009)).

Gas hydrates are distributed heterogeneously and can fill the pore space in the sediment or heave the sediment to form lenses. Hydrates will form preferentially in coarse-grained sands (Tréhu *et al.*, 2006). There are three categories for the interaction between hydrate and the host sediment (shown in Figure 2.9)(Winters *et al.*, 2004): (1) Hydrate floating in the pore space of the sediment. (2) Hydrate supporting the pore structure. (3) Hydrate coating and cementing the sediment particles.

2.5.3 Estimation of Hydrate Regions

The maximum stability depth is determined by the overlap of the hydrate region in pressure-temperature equilibrium data and the geothermal gradient (Figure 2.10). Methane solubility/availability determines the top and bottom boundaries to this hydrate region.

2.5.4 Natural Gas Recovery From Hydrate Deposits

Makogon (1997) described three common means of hydrate dissociation: depressurization, inhibitor injection, and thermal injection. In each dissociation process there are heat transfer, kinetic dissociation of hydrates and flow of fluids away from the hydrate interface steps. Of the three dissociation methods,

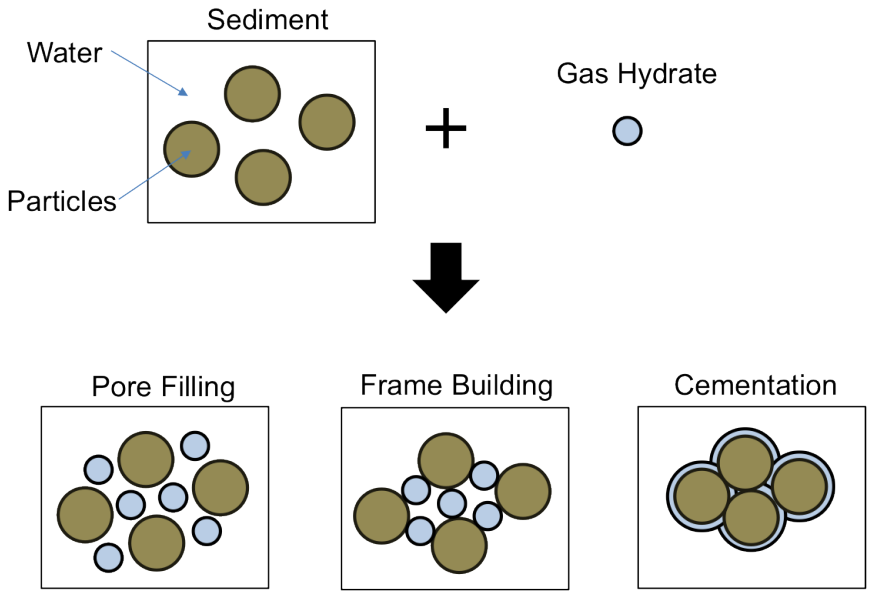

Figure 2.9 – Disseminated hydrate and sediment structure interaction model (Winters *et al.*, 2004)

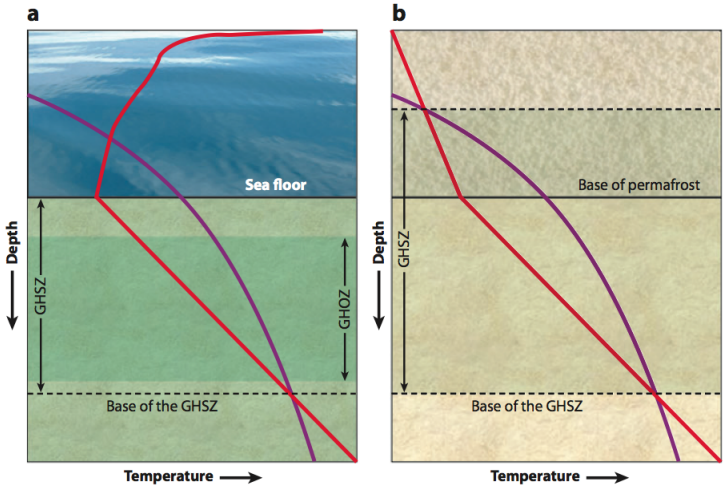

Figure 2.10 – Hydrate stability regions in (a) marine and (b) arctic permafrost sediments (Hester and Brewer, 2009).

depressurization is the most economical (Howe *et al.*, 2004). A study by Hong and Pooladi-Darvish (2005) found that conductive heat transfer controls the

rate of hydrate dissociation in these processes.

2.6 Experimental Apparatuses and Methods

This section discusses methods for laboratory studies of gas hydrates. These include: microscopic (e.g., molecular structure) and macroscopic (e.g., thermodynamics, transport phenomena, morphology and distribution of the hydrate phase) measurements.

2.6.1 Microscopic Methods

X-ray diffraction has been used to determine the crystal structure of hydrate formers. Synchrotron X-ray diffraction measurements have higher sensitivity than laboratory X-ray measurements. Neutron diffraction has been used to determine thermal expansion in hydrates (sI, sII and sH) (Rawn *et al.*, 2003), as well as, guest and host positions. Neutron diffraction methods include high resolution neutron powder diffraction (to determine structural transitions during hydrate formation (Staykova *et al.*, 2003)), small angle neutron scattering (to determine hydration structures during hydrate formation (Thompson *et al.*, 2006)) and neutron spectroscopy (to determine guest-host interactions in a hydrate lattice (Baumert *et al.*, 2003)).

2.6.2 Macroscopic Methods

Laser scattering has been applied to hydrate studies using the focused beam reflectance method (FBRM). Clarke and Bishnoi (2005) used the FBRM to measure hydrate particle size distribution during formation and dissociation. The FRBM uses a cylindrical probe containing a near-infrared (785 nm wavelength) laser. The laser is rotated at a high velocity. During an experiment the laser hits particles and is reflected back. The chord length of a particle is equal to the product of the laser velocity and the measured intersecting time with the particle.

X-ray computed tomography (CT) has recently been used to measure hydrate transport properties (e.g., thermal conductivity, thermal diffusivity and permeability) as well as the density of hydrate, water and gas phases (Moridis *et al.*, 2005; Kneafsey *et al.*, 2005, 2007).

Solid-state NMR spectroscopy has been used for structure identification, quantifying cage occupancy, identifying structure changes in hydrate formation and dissociation, and measuring molecular reorientation and diffusion. Raman spectroscopy has been applied to structure identification, cage occupancies and formation kinetics of hydrate structures (Sum *et al.*, 1997; Tulk *et al.*, 2000; Susilo *et al.*, 2007).

Phase Equilibria

Hydrate phase equilibria can be determined by indirect methods such as an associated pressure drop or temperature increase in the fluid phase or direct methods such as visual observation of the hydrate phase.

Due to metastability, hydrate formation will occur at conditions well past hydrate equilibrium; however, metastability is not observed for hydrate dissociation. For a system with multiple gas components, there will often be preferential encapsulation of one component (Linga *et al.*, 2007; Kobayashi *et al.*, 2007), then the system returns to the initial gas composition after hydrate dissociation. The melting point is therefore the best measurement of hydrate equilibrium (or the lower limit of hydrate formation).

A stirred pressure vessel with temperature and pressure control is often used to determine hydrate phase equilibria. The equilibrium is determined by observation and/or temperature and pressure changes (Beltrán and Servio, 2008). Figure 2.11 is a schematic of a stirred vessel for equilibrium measurements.

A novel equilibrium measurement method was developed by Mohammadi *et al.* (2003) which uses a Quartz Crystal Microbalance (QCM). A quartz disk is sandwiched between two electrodes. The crystal oscillates at a resonant frequency when an electric current is passed through it. This frequency changes if any mass is adhered to the crystal surface. This mechanism is placed inside a pressure vessel. A drop of water is added to the surface of the quartz and temperature or pressure is controlled to induce hydrate formation. Formation is indicated by a change in the resonant frequency of the quartz. One problem with this method is that it requires that the hydrate formation occurs at the quartz surface, which is not always the case.

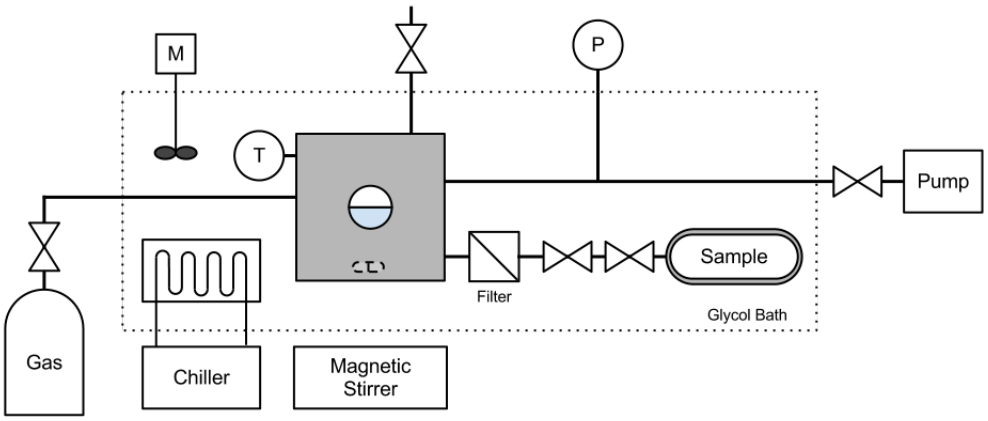

Figure 2.11 – Schematic of a stirred reactor for equilibrium measurements (based on Servio and Englezos (2002)).

Thermal Properties

Thermal properties are more difficult to measure due to the uncertainty of system composition and hydrate decomposition in atmospheric conditions. One method for determining the thermal properties of hydrates is to use cyclic ethers (e.g., ethylene oxide for sI and tetrahydrofuran for sII) because they form at atmospheric pressure at temperatures above 273 K; however, measurements of high pressure hydrate systems (e.g., methane and carbon dioxide) are still desired. Commercial high pressure calorimeters are now available for heat of dissociation and heat capacity measurements of these hydrate systems (Gupta *et al.*, 2008).

Two common methods for measuring thermal conductivity are the transient needle probe method and the steady-state guarded hot-plate method. In the transient needle probe method a probe containing heater wire and a thermistor is surrounded by a hydrate sample. With a step change in the heater input power, the surrounding temperature will vary with thermal conductivity (Waite, 2002). In the steady state method a hydrate sample is placed on a heating plate and thermocouples at the top and bottom of the sample measure the thermal gradient.

Formation Kinetics

A large number of kinetics experiments have been performed in flow loops to simulate field conditions. The results from these tests indicate the most probable locations for hydrate plug formation in pipelines Zerpa *et al.* (2012).

Smaller scale apparatuses like the one shown in Figure 2.12 are used to study the apparent and intrinsic kinetics of hydrate growth and dissociation. The original design for this type of apparatus was by Vysniauskas and Bishnoi (1983). It has been modified by other researchers over the years. During hydrate formation the system remains at constant pressure through the use of a control valve feeding gas from a reservoir. The rate in change of pressure over time can be correlated to the molar rate of gas converted into hydrate. Differential pressure is measured from the reservoir to a reference instead of to atmospheric pressure. This shortens the differential span, increasing the accuracy of the measurement (Bergeron and Servio, 2009).

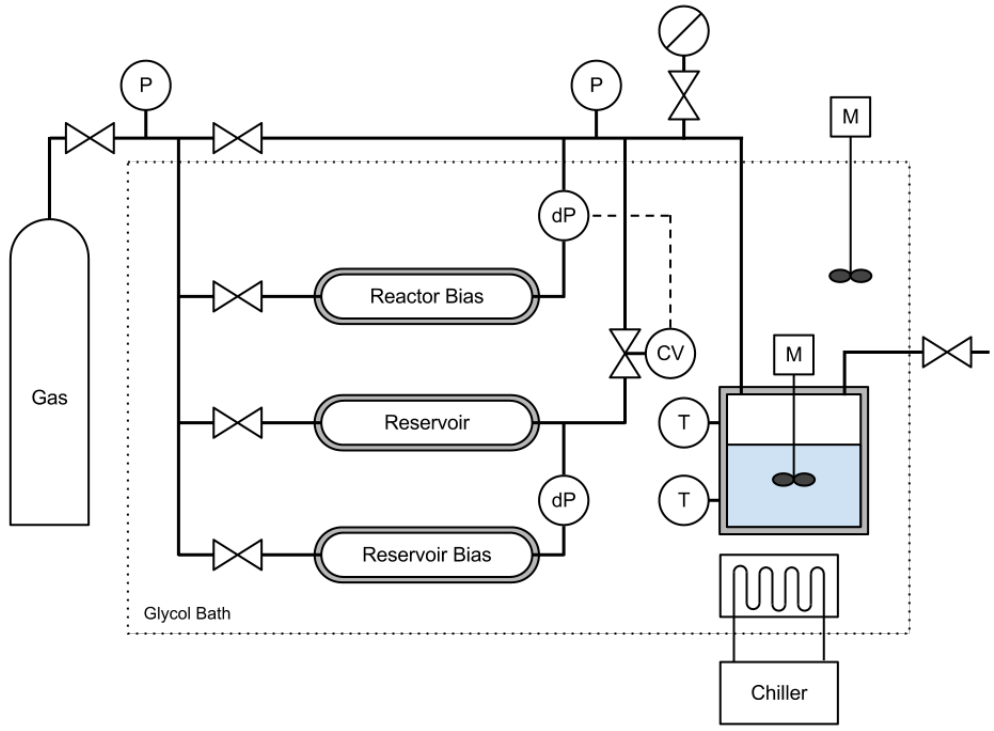

Figure 2.12 – Schematic of a stirred reactor for kinetics measurements (based on the design by Bergeron and Servio (2009)).

Nucleation times for gas hydrates are stochastic in nature and are therefore difficult to measure. A recent method by Maeda *et al.* (2011), discussed in section 2.3.2, uses the HP-ALTA. The sample is frozen and thawed upwards of 300 times to generate a data set large enough for statistical analysis.

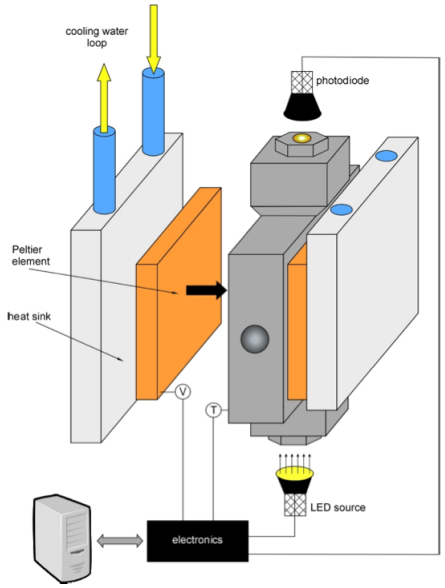

Figure 2.13 – Schematic of the High-Pressure Automated Lag Time Apparatus (Reproduced from Maeda *et al.* (2011)).

Morphology

Observations of hydrate growth morphology provide a picture of the events that occur upon hydrate formation. These experiments can aid in the development of appropriate hydrate growth models.

Morphology hydrate reactors are often used to assess the effect of driving force on hydrate morphology and to measure apparent growth kinetics though hydrate film velocity (Freer *et al.*, 2001; Servio and Englezos, 2003a; Taylor *et al.*, 2007; Peng *et al.*, 2007; Tanaka *et al.*, 2009; Beltran and Servio, 2010; Kitamura and Mori, 2013; Li *et al.*, 2014). In general, the reactor designs consist of a pressurized (stirred or quiescent) sample cell, with temperature control via a coolant jacket or bath. The vessel sight widows are typically oriented horizontally to view the guest-water interface. Beltran and Servio

2010 designed a reactor with vertically oriented sight windows, which allowed for observation of hydrate spreading onto glass surfaces (Figure 2.14).

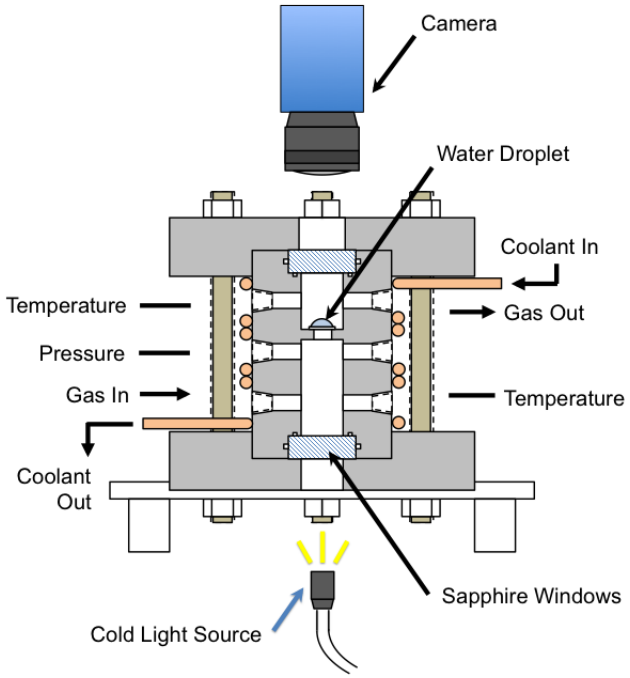

Figure 2.14 – Schematic of a hydrate morphology reactor with vertically oriented sight windows (Beltran and Servio, 2010).

Solid-Liquid Interface Interaction with Foreign Particles

In nature, hydrates are often found within porous media, such as soil or other sediment. Measurements in this area focus on the effect of gas hydrates on the mechanical and thermal properties of the sediment and hydrate growth mechanisms in sediment.

Apparatuses designed to measure hydrate/sediment interactions are unidirectionally cooled to generate a thermal gradient through the sample. In nature, solidification tends to occur at areas with high thermal gradients (Körber

et al., 1985). For mechanical property measurements, the hydrate/sediment sample must be kept under an external confining pressure (often applied by a piston). The internal pressures include gas pressure, pore pressure and the back pressure (depending on the apparatus design) (Winters *et al.*, 2004). The measured properties are dependent on the physical interaction between the hydrate phase and the sediment structure.

The interaction between foreign particles and hydrate-liquid water interface growth has recently begun to be studied for hydrates that form at atmospheric pressure above the ice point (*e.g.*, tetrahydrofuran hydrates) (Suzuki *et al.*, 2011; Muraoka and Nagashima, 2012). These particle interface interactions have been studied extensively for other systems (*e.g.*, foreign particles and ice or metallic crystals) (Uhlmann *et al.*, 1964; Körber *et al.*, 1985; Rubinsky and Ikeda, 1985). The particle interface interaction is measured by observation of hydrate growth on a directional solidification stage. The growing hydrate front will either reject or engulf the foreign particle depending on the growth velocity, the mass of the particle and surface thermodynamics. Directional growth is achieved by applying a thermal gradient across the sample stage. Figure 2.15 is a schematic of a typical directional growth stage.

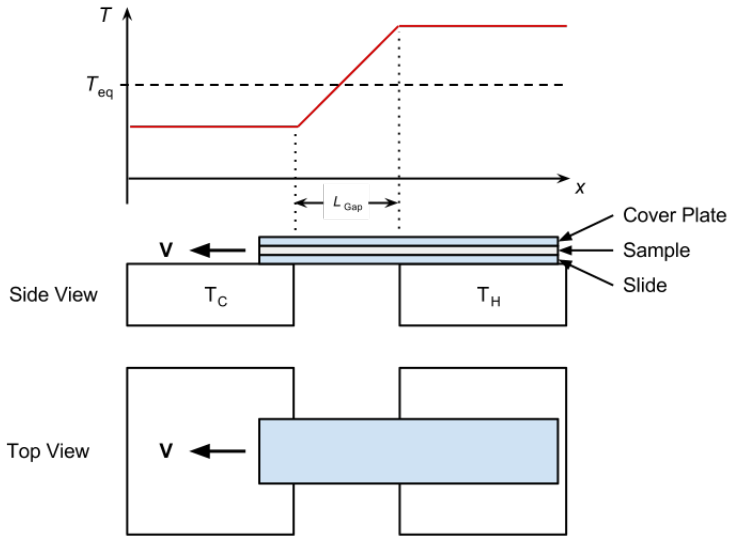

Figure 2.15 – Schematic of a directional growth stage with temperature profile.

In the standard design, a sample slide is pulled by a motor across a gap

between two constant temperature plates. The temperatures are set above and below solid-liquid equilibrium. As the sample is moved across the gap, crystallization will occur in the opposite direction at a similar velocity. The plates are made out of a very thermally conductive metal (e.g., copper). The slide must be transparent and must also be thermally conductive to allow for linear temperature gradients at reasonable gap lengths. Most older designs use glass slides ($l_{gap} \approx 5$ mm); however, sapphire is a much better choice because it has a higher thermal conductivity($l_{gap} \approx 12$ mm) (Liu *et al.*, 2003).

Temperature Control Methods

Typically, the experimental temperature of the hydrate system is controlled though the pressure vessel by a coolant jacket or coolant bath. This design can lead to slow response times (in the order of minutes) for a change in set-point temperature. As well, the temperature control stability is typically not very precise (often ±0.5 °C). For fast, precise, temperature control, current setups use thermoelectric cooler modules (TECs) (Liu *et al.*, 2003; Lee *et al.*, 2010; Maeda *et al.*, 2011; Muraoka and Nagashima, 2012). A TEC uses the Peltier effect to control the heat transfer rate from its top surface to its bottom surface. Direct current is applied through n and p-type semiconductors connected in series resulting in heat being absorbed through one side of the module and rejected on the other. These TEC assemblies typically have temperature control stability within ±0.01 °C. Figure 2.16 shows the design from the patent application by Lee *et al.* (2010) for a hydrate morphology reactor cooled externally by a TEC assembly.

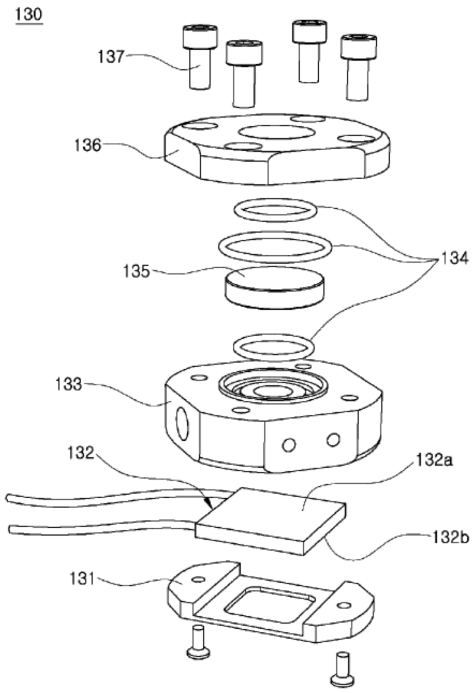

Figure 2.16 – Diagram for a hydrate morphology reactor cooled externally by a TEC assembly (Lee *et al.*, 2010).

Chapter 3

Experimental

3.1 Apparatus

A new experimental set-up was designed to control gas hydrate crystal growth at pressures up to 20 MPa (Figure 3.1).

The central part of the apparatus consisted of a pressure vessel that contained a bilateral temperature control stage (High-Pressure Bilateral Temperature Control Stage or HP-BTCS). The stage controlled the temperature across a sample of water that was pressurized in an atmosphere of a hydrate forming gas.

A 316 stainless steel cell (designed in accordance to the ASME BPVC, see Appendix B) was fitted with sapphire sight windows and wrapped in a coolant jacket. Several radial ports allowed for gas in, gas out, temperature measurement, pressure measurement and gland seal fittings.

Sapphire sight widows (Rayotek, CA, USA) were oriented on the vertical axis for a 'bird's eye' view of the sample stage. Sapphire was chosen as the widow material for its high transmittance (98.5%) in the visible light region and scratch resistance. The stage was illuminated from the bottom window with a Schott KL2500 LCD cold light source (Optikon, ON, Canada). Images were acquired through the top window with a PCO.edge 5.5 sCMOS camera (Optikon, ON, Canada). A Nikon AF-Micro-Nikkor 60 mm lens (Optikon, ON, Canada) was used for low magnification images. An Infinity KC microscope and IF series objectives (Optikon, ON, Canada) were used for high magnification images.

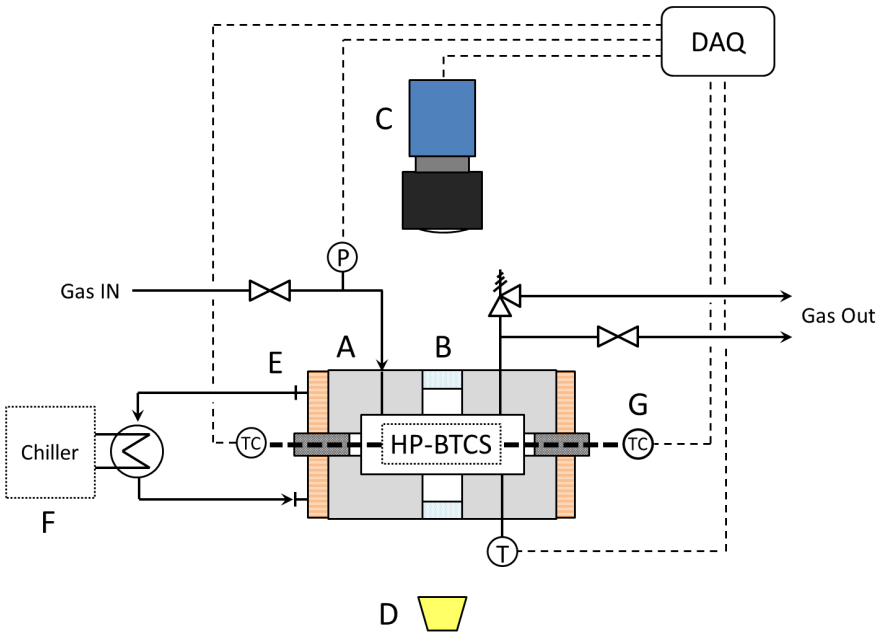

Figure 3.1 – Simplified piping and instrumentation diagram for the gas hydrate crystallizer. (A) 316 stainless steel pressure vessel. (B) Sapphire sight windows. (C) Video camera. (D) Cold light source. (E) Coolant jacket. (F) Refrigerated circulator. (G) Bi-polar PID temperature controllers.

The pressure vessel was cooled by a Thermo Scientific AC200 refrigerated circulator (Fisher Scientific, Canada), which was used to circulate a 50/50 (v/v) mixture of ethylene glycol and water through a copper coil wrapped around the external circumference of the vessel.

The pressure of the cell was measured by a Rosemount 3051s pressure transmitter (Laurentide Controls, QC, Canada) with an accuracy of $\pm 0.025\%$ of the span. The temperature of the cell was measured with a platinum RTD probe (Omega Engineering, QC, Canada) with an accuracy of ± 0.32 °C.

Two Conax Technologies transducer gland seal fittings (Electro-Meters, ON, Canada) were used to seal a total of eight wires through the vessel wall.

3.1.1 High-Pressure Bilateral Temperature Control Stage

The HP-BTCS was designed to independently control temperature on opposing sides of the stage. Figure 3.2 shows a schematic of the HP-BTCS. Both ends of the stage have a thermoelectric cooler (TEC) (TE Technology, MI, USA) to transfer heat from the top to the bottom surface of the stage. Copper plates were fastened to the top and bottom of each TEC to uniformly distribute temperature on the top and bottom surfaces. The body of the pressure vessel was used as a heat sink for the bottom of each TEC. Temperature of both the top copper plates were measured by fast-response thermistor elements (TE Technology, MI, USA) with a resolution of 0.01 °C and an accuracy of ±1 °C. A sapphire substrate was used to hold a water sample and bridge the two ends of the stage. The TECs were controlled by two bi-polar PID temperature controllers (TE Technology, MI, USA), with a resolution and a temperature control stability of ±0.01 °C.

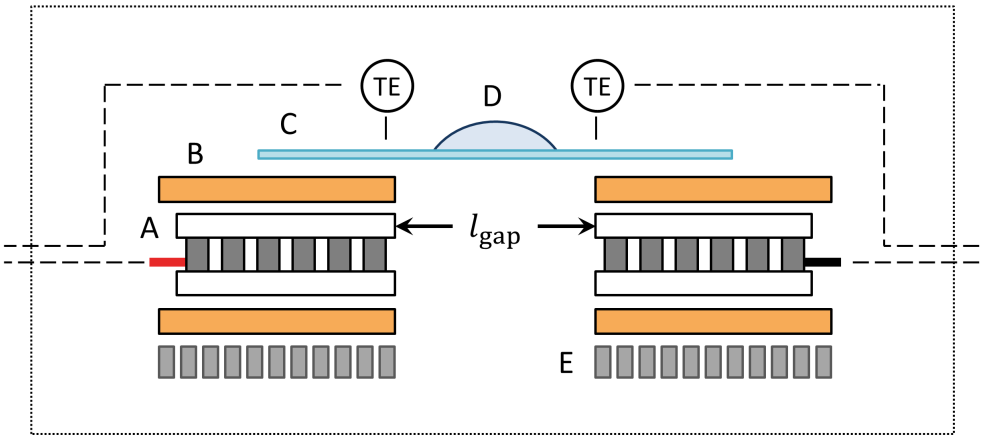

Figure 3.2 – Schematic of the High-Pressure Bilateral Temperature Control Stage. (A) Thermoelectric cooler module. (B) Copper plate. (C) Sapphire substrate. (D) Water droplet. (E) Heat sink.

3.2 Methods

Before each experiment the sapphire substrate was cleaned with liquid detergent and isopropanol. The sapphire was thoroughly rinsed with deionized water after each cleaning step. A small amount of thermal paste was applied to both the top copper plates, where the sapphire was to make contact. The

cleaned sapphire was then set into position on the HP-BTCS. A 20 μL sample of distilled, deionized water was transferred onto the sapphire substrate with a micro pipette. The vessel was then sealed and purged with 99.99% (molar) methane gas (Air Liquide, ON, Canada).

3.2.1 Crystal Formation History

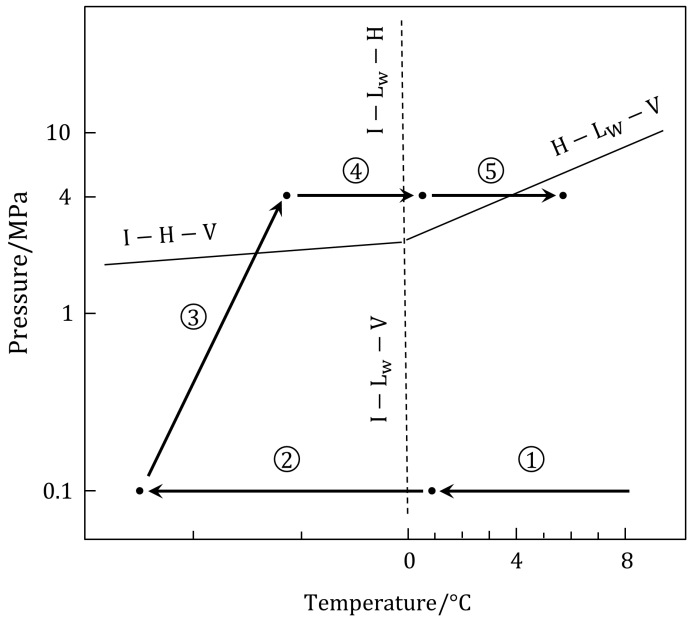

Figure 3.3 – Temperature and pressure trace for ice and initial methane hydrate formation. (1) The vessel is cooled to 1 °C. (2) The HP-BTCS is cooled to −10 °C, forming ice. (3) The pressure is increased past I-H-V. (4) The HP-BTCS is heated past 0 °C, thawing the ice and seeding hydrate formation. (5) The HP-BTCS is heated past H-L_W-V, dissociating the initial hydrate.

The water sample was first frozen at atmospheric pressure then subsequently thawed at a higher pressure in the hydrate stable region to seed hydrate crystal growth Figure 3.3.

At atmospheric pressure the entire vessel was cooled to 1 °C using the coolant jacket. The stage temperature was then uniformly cooled to −10 °C to form ice. After ice had formed the pressure was increased to the experimental

pressure. The jacket temperature was also increased, such that the temperature surrounding the stage was above the Hydrate-Liquid-Vapour (H-L-V) temperature at the experimental pressure. During pressurization, the stage temperature was uniformly heated to −5 °C. While the surrounding temperature stabilized, the camera lens was refocused to account for the change in pressure. The stage was then uniformly heated past 0 °C, where the thawed ice was immediately replaced by methane hydrate. Finally, the stage was heated to 1 °C above H-L-V at the experimental pressure (*e.g.*, 5 °C at 4 MPa), which completely dissociated the initial methane hydrate.

3.2.2 Hydrate Formation

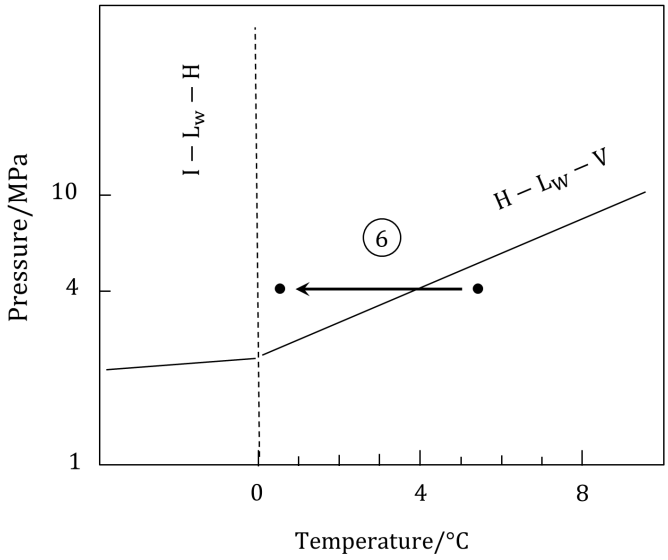

Figure 3.4 – Temperature and pressure trace for hydrate formation. (6) The HP-BTCS was cooled to the experimental temperature conditions at constant pressure, inducing hydrate formation.

For hydrate formation experiments, the pressure and temperature surrounding the stage were maintained constant. The HP-BTCS was used to locally cool the water sample to the experimental temperature conditions (Figure 3.4). Experiments were conducted with a uniform surface temperature and with a constant temperature gradient. Replicates for the uniform surface temperature experiments were carried out for low, medium and high supercooling.

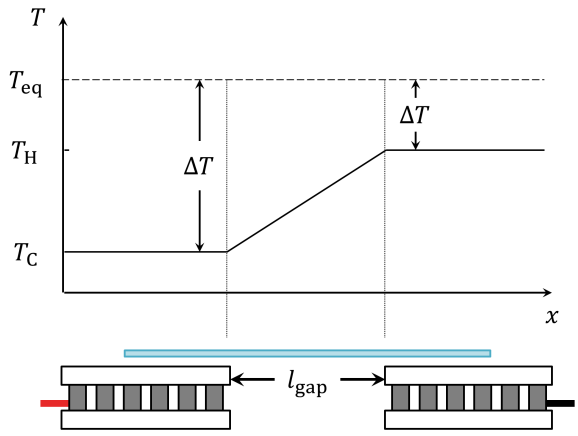

Figure 3.5 – Temperature profile for hydrate formation on a constant temperature gradient. $T_H - T_C = 4$ °C.

For temperature gradient experiments, both sides of the stage were cooled to near the H-L-V temperature, then one side was cooled to obtain a temperature difference of 4 °C across the stage (Figure 3.5). For both uniform surface temperature and constant temperature gradient experiments, hydrate crystal nucleated within five minutes after the stage was cooled below H-L-V. The stage temperature conditions were held constant (±0.01 °C) for the duration of hydrate formation.

3.2.3 Hydrate Dissociation

The pressure and temperature surrounding the stage were constant during hydrate dissociation. Initially, the high temperature on the HP-BTCS was set near the H-L-V temperature and the low temperature was set for a temperature difference of 4 °C across the stage. The high and low setpoint temperatures were increased simultaneously in 0.5 °C increments (Figure 3.6). Each step increase in the setpoint temperatures moved the H-L-V isotherm toward the cold side of the stage. Temperature was held constant at both ends of the stage while the hydrate dissociated in the region of the stage above the H-L-V temperature and the hydrate- water interface stabilized.

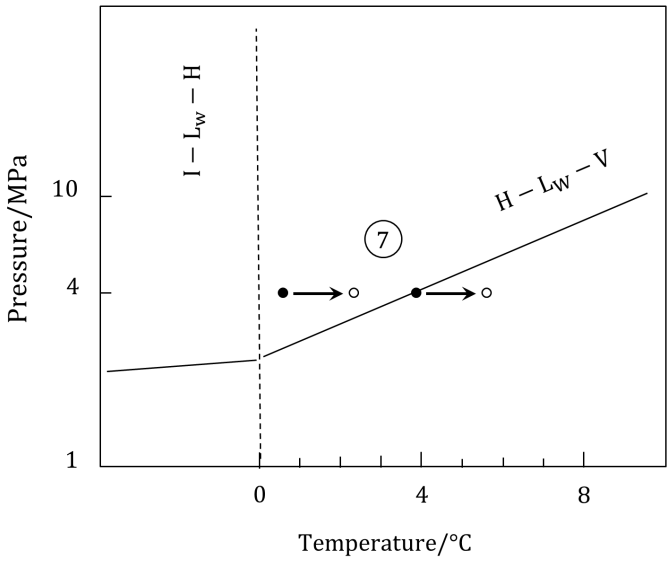

Figure 3.6 – Temperature and pressure trace for a single hydrate dissociation step. (7) The temperature was increased simultaneously on both sides of the HP-BTCS, dissociating the hydrate only in the region of the stage above H-L-V.

Chapter 4

Results

In this chapter, the results of the hydrate formation and dissociation experiments using the High-Pressure Bilateral Temperature Control Stage (HP-BTCS) are reported.

The hydrate formation experiments were designed to assess hydrate growth induced by a temperature-controlled, external surface. Hydrates were formed on a constant temperature surface and a constant temperature gradient surface. The hydrate dissociation experiments were designed as a preliminary assessment of the directional crystallization capabilities of the HP-BTCS. The applied thermal gradient and the two-sided temperature control were used to move the solid-liquid interface position.

Methane was used as the hydrate guest for these experiments. To reduce induction times for hydrate nucleation, all of the hydrate formations were preceded by freezing (ice) and thawing the water droplet. All of the experiments presented in this work are formations with recent crystal structure history. Effects of hydrate formation history are not discussed.

4.1 Hydrate Growth

4.1.1 Constant Surface Temperature

The first set of experiments involved hydrate formation with a constant, uniform stage temperature applied to the water sample. To achieve the constant temperature surface, both sides of the stage were set to same temperature.

These experiments were designed to evenly supercool the water sample to the target driving force for hydrate formation. The purpose of these experiments was to replicate the standard method in literature to correlate driving force and polycrystalline morphology.

Hydrate Growth

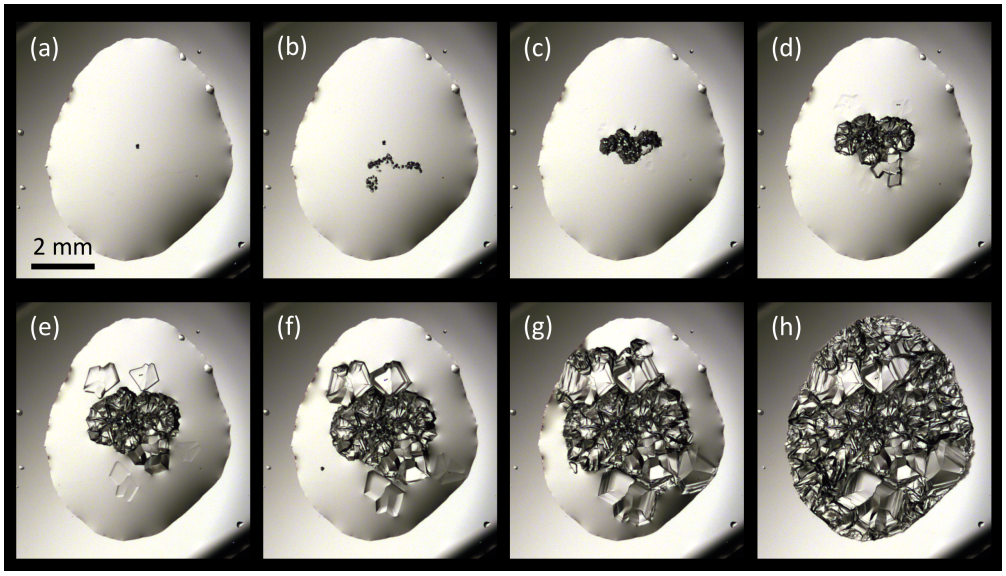

Figure 4.1 – Methane hydrate formation and growth on a water droplet at constant temperature. $p = 4.03$ MPa, $T = 276.2$ K. (a) Water droplet before hydrate formation. (b) Initial hydrate growth points moving toward the centre of the droplet. (c) Continued growth from the initial growth points. (d - g) Single crystals of hydrate form ahead of the growth front. (h) Droplet is completely covered by hydrate after 8 minutes and 52 seconds

Figure 4.1 shows a typical sequence for hydrate formation on water droplets with the HP-BTCS at constant temperature. The hydrate crystals often appear to nucleate at random points in the droplet. These initial growth points exhibited single-crystal geometries corresponding to structure I hydrate. After nucleation the crystals floated to the centre of the droplet. The hydrate film then advanced from these growth points in the centre of the droplet toward the droplet periphery. Once the hydrate film had reached the edge of the droplet, a thin film of hydrate spread onto the sapphire surface. This hydrate film has been referred to as the hydrate halo or the 'bridge effect' (Beltran and Servio,

2010).

Driving Force and Reproducibility

Figure 4.2 is a comparison of methane hydrate films formed at different driving forces, showing consistent morphologies across replicates. Each hydrate was formed at a constant pressure ranging from 4.00 to 4.04 MPa. At constant pressure the driving force for hydrate formation can be simplified as the supercooling for the system (Equation 4.1).

$$\Delta T = T_{eq} - T_{exp} \tag{4.1}$$

Where T_{eq} is the three-phase Hydrate-Liquid-Vapour (H-L-V) equilibrium temperature at the system pressure and T_{exp} is the temperature of the water in the liquid phase.

The low driving force (ΔT = 1.3 K) hydrate films all formed with irregular, geometric growth patterns which resulted in faceted morphologies. Often single crystals of hydrate would form ahead of the primary hydrate film and subsequently attach to the growing interface. Whereas, the high driving force (ΔT = 3.8 K) hydrate films were macroscopically uniform during growth, with an even, circular interface. The resulting hydrate surface had a smoother morphology compared to that of low driving forces. Concentric film growth was also observed for the medium driving force (ΔT = 2.3 K); however, the interface during growth was more jagged. Medium driving forces resulted in film morphologies that were rougher than those of the the high driving force hydrate films. The overall surface was rougher at low driving forces, due to the larger size of distinct crystal facets; however, the facets themselves were significantly smoother than the medium and high driving force surfaces.

Figure 4.3 and Figure 4.5 show magnified views of the low, medium and high driving force hydrate morphologies. The magnification used in Figure 4.2 was only able to resolve individual hydrate crystals across the entire surface for the low driving force hydrates. With the high magnification images, individual hydrate crystals were also observed for the medium and high driving force hydrates.

At higher magnifications, dark channels became apparent on the hydrate film surface (Figure 4.3 and Figure 4.4). These channels extended through the

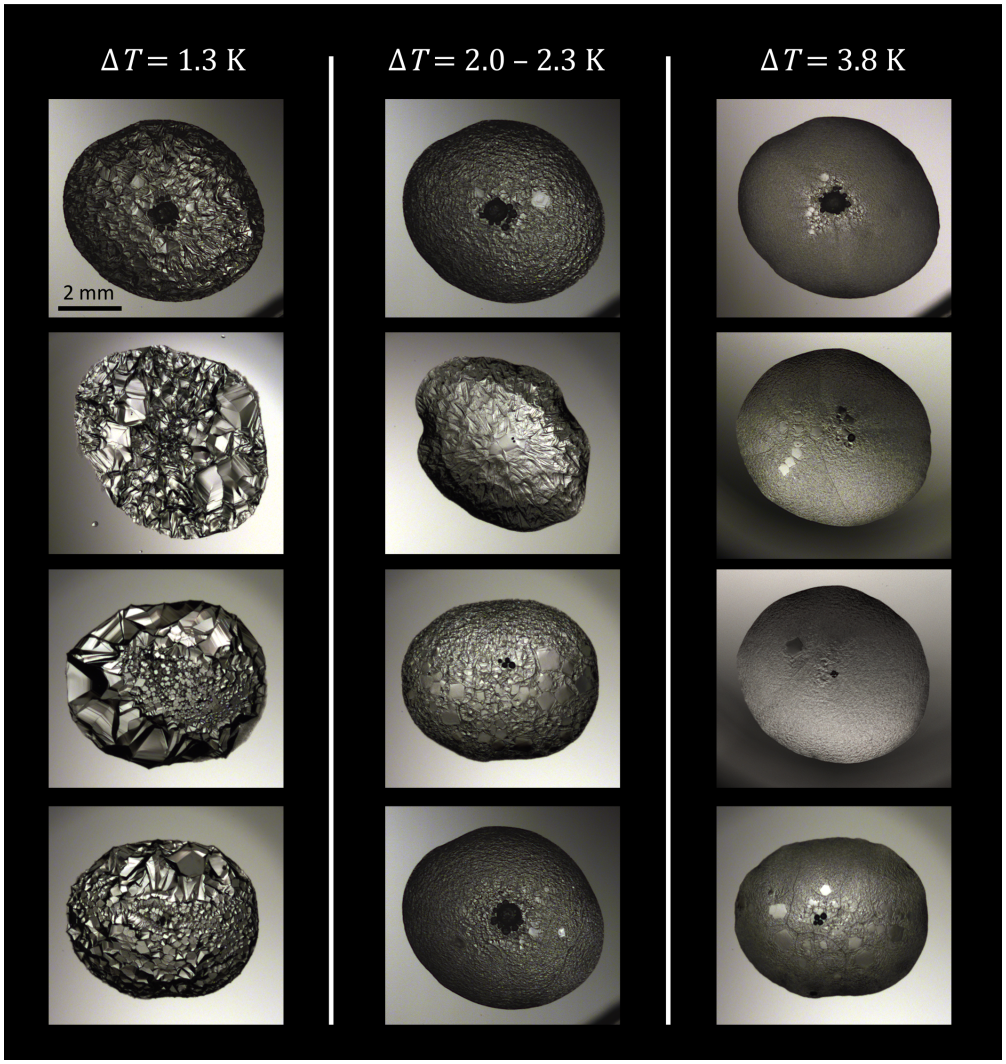

Figure 4.2 – Water droplets completely covered by methane hydrate formed at low (ΔT = 1.3 K, left), medium (ΔT = 2.0 – 2.3 K, middle) and high (ΔT = 3.8 K, right) driving forces, with four replicates for each. p = 4.0 MPa for each hydrate.

surface of the newly formed hydrate up to the boundary of the droplet (Figure 4.5); they were mainly present along boundaries of distinct hydrate crystals.

At the droplet boundary, the channels appeared to extend onto the sapphire

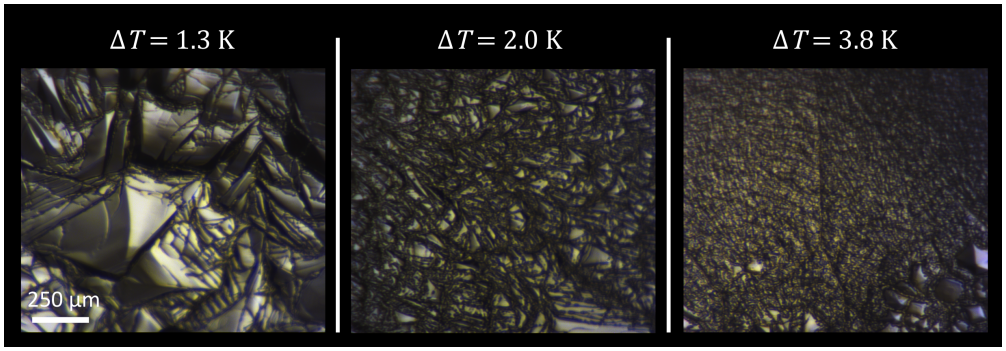

Figure 4.3 – Magnified view of the droplet surface for methane hydrates formed at low (ΔT = 1.3 K, left), medium (ΔT = 2.0 K, middle) and high (ΔT = 3.8 K, right) driving forces. p = 4.0 MPa and for each hydrate.

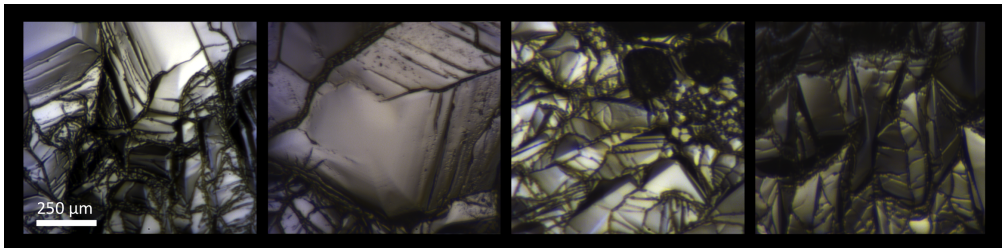

Figure 4.4 – Detail of methane hydrates formed at low driving forces (ΔT = 1.3 K) with dark channels visible on the film surface. p = 4.0 MPa for each hydrate.

surface as the hydrate halo propagated. This channel extension onto the sapphire surface was clearly visible for low driving force hydrates, but not observable for medium nor for high driving force hydrates. The halo morphology Figure 4.5 was found to depend on driving force. The halo at low driving forces had visible dark channels that led to a sharp point at the interface. At medium driving forces, the halo interface had multiple rounded peaks and valleys. High driving forces resulted in a smoother halo interface.

4.1.2 Constant Gradient Surface Temperature

The HP-BTCS was used to apply a constant temperature gradient to the water sample during hydrate formation. This was achieved by maintaining a constant temperature (below HLV) on one side of the slide while maintaining a constant lower temperature at the other end of the slide. Thus, the

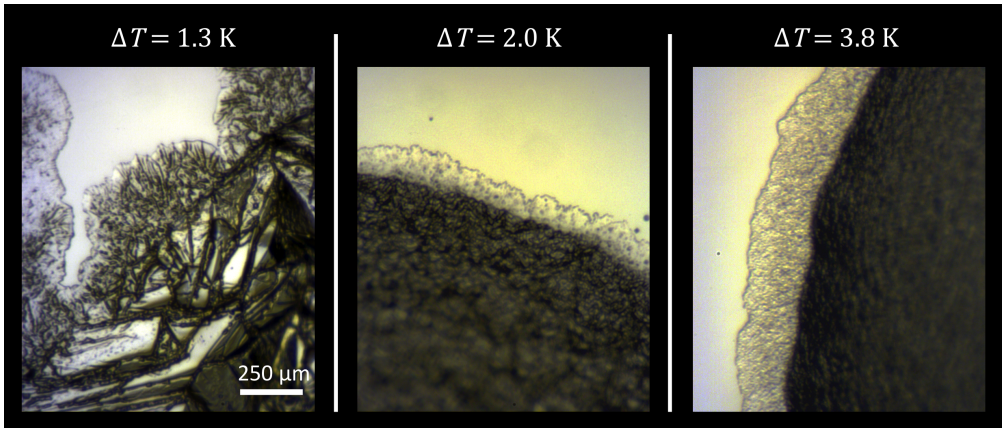

Figure 4.5 – Magnified view of the droplet periphery for methane hydrates formed at low (ΔT = 1.3 K, left), medium (ΔT = 2.0 K, middle) and high (ΔT = 3.8 K, right) driving forces. p = 4.0 MPa for each hydrate.

driving force for hydrate formation increased across the length of the stage (Figure 3.5).

Hydrate Growth

Figure 4.6 shows a typical sequence for hydrate growth on a water droplet while the HP-BTCS applied a temperature gradient. The initial hydrate growth occurred in the same manner as hydrate growth on the constant temperature surface, where initial growth points occurred at random points in the droplet and subsequently floated to the centre on the droplet. Once the initial growth points had reached the centre of the droplet, the hydrate front advanced rapidly toward the cold end of the gradient and slowly toward the hot end of the gradient. The initial hydrate halo grew from the cold end of the droplet boundary where the hydrate film first reached the sapphire surface. This halo growth occurred before the droplet was completely covered by hydrate. Subsequent hydrate halo growth was observed only once the hydrate film had reached the droplet boundary.

Driving Force and Reproducibility

Figure 4.7 shows replicates for methane hydrate film morphology when formed on a temperature gradient. For each experiment the morphology varied across

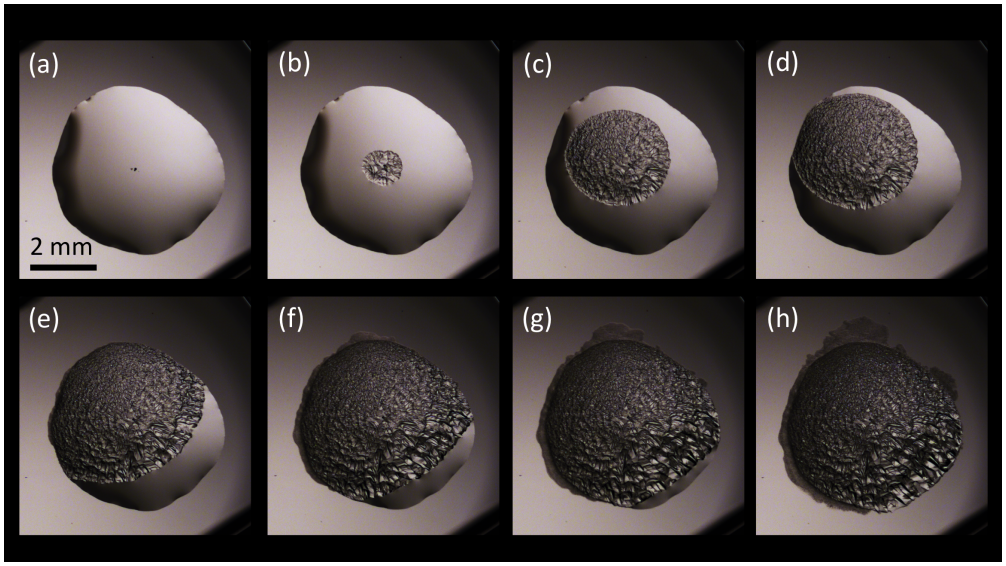

Figure 4.6 – Methane hydrate formation and growth on a water droplet with a temperature gradient. The gradient increased from $T_C = 273.7$ K (upper left) to $T_H = 277.7$ K (lower right). $p = 4.03$ MPa, $T_{HLV} = 277.5$ K. (a) Water droplet before hydrate formation. (b) Hydrate growth after nucleation. (c) Continued growth from the droplet centre. (d) hydrate film reached the cold side of the droplet boundary. (e) initial hydrate halo propagation from the cold side of the droplet boundary. (f - g) Continued hydrate film growth toward the hot side of the gradient. (h) Droplet is completely covered by hydrate after 8 minutes and 46 seconds.

the droplet and was consistent for each replicate. The hydrate film transitioned from a uniform morphology near the cold side of the gradient to a faceted morphology near the hot side of the gradient. These morphologies correspond to the driving force effects observed for the constant surface temperature experiments (Figure 4.2).

Figure 4.8 shows a methane hydrate formed on a droplet that spanned a larger range of the temperature gradient; detailed views of the characteristic driving force morphologies are also shown. The detailed views show the surface roughness decreasing with increasing degree of supercooling. The dark channels observed in Figure 4.3 and Figure 4.4 are also present on the hydrate film.

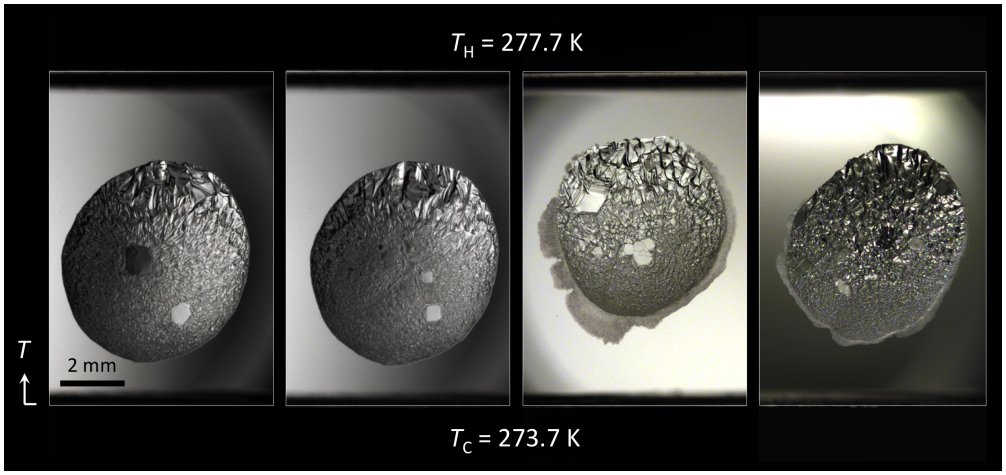

Figure 4.7 – Replicates for methane hydrate morphology on a water droplet with an applied temperature gradient. $p = 4.0$ MPa, $T_C = 273.7$ K, $T_H = 277.7$ K, $T_{HLV} = 277.5$ K.

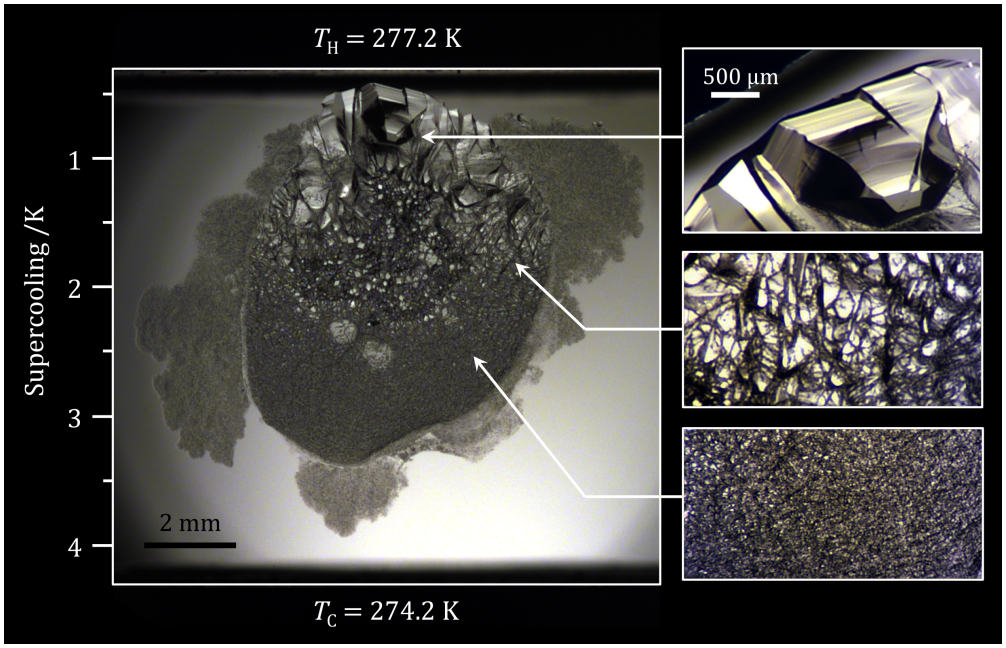

Figure 4.8 – Detail of methane hydrate morphology on a water droplet with an applied temperature gradient. $p = 4.02$ MPa, $T_C = 274.2$ K, $T_H = 277.7$ K, $T_{HLV} = 277.5$ K.

4.2 Film Velocity

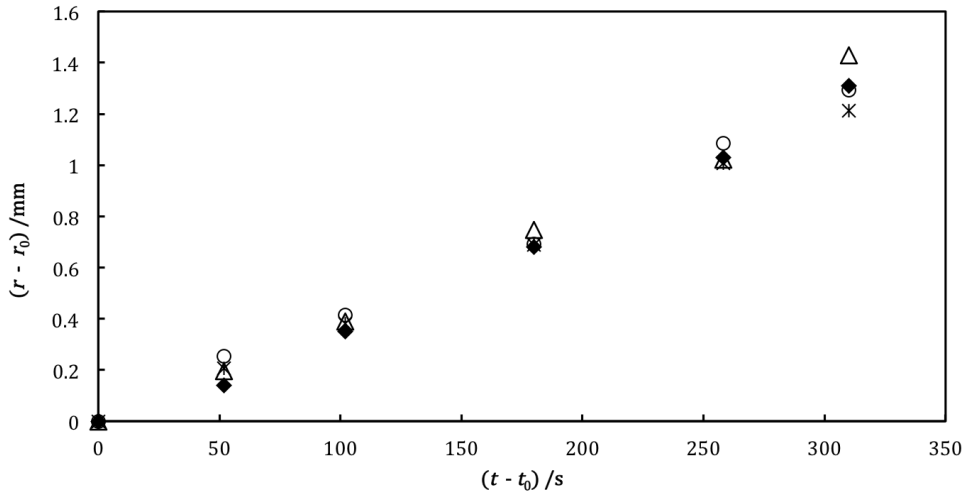

Figure 4.9 – Interface position versus time for a methane hydrate film formed on a constant temperature surface. $\Delta T = 1.3$ K, $p = 4.03$ MPa. Four positions on the film were plotted over time; the markers correspond to these individual positions. Film length was determined relative to a fixed point near the origin of the film. The position-time data was plotted relative to the initial position (r_0) and time (t_0).

Figure 4.9 is a typical plot of multiple film length measurements on a single droplet, at a constant driving force of 1.3 K, over the span of hydrate growth. The film lengths were measured with respect to a fixed point on the hydrate film. Since only the change in interface position over time was desired, the initial lengths and times were used as benchmarks.

Figure 4.10 shows the change in interface position of a hydrate film over time for constant temperature experiments at three different driving forces. The length was determined by the change of position of a point on the hydrate-water interface relative to a fixed point near the origin of the film. The film velocity was constant over the measured time interval. The film velocity was 4.2 ± 0.2 $\mu\text{m} \cdot \text{s}^{-1}$ for the low driving force ($\Delta T = 1.3$ K), 10.5 ± 0.4 $\mu\text{m} \cdot \text{s}^{-1}$ for the medium driving force ($\Delta T = 2.2$ K) and 63.1 ± 1.7 $\mu\text{m} \cdot \text{s}^{-1}$ for the high driving force ($\Delta T = 3.8$ K).

Figure 4.11 shows the hydrate film position versus time plot for hydrate growth on a temperature gradient at constant pressure ($p = 4.03$ MPa). The cold end

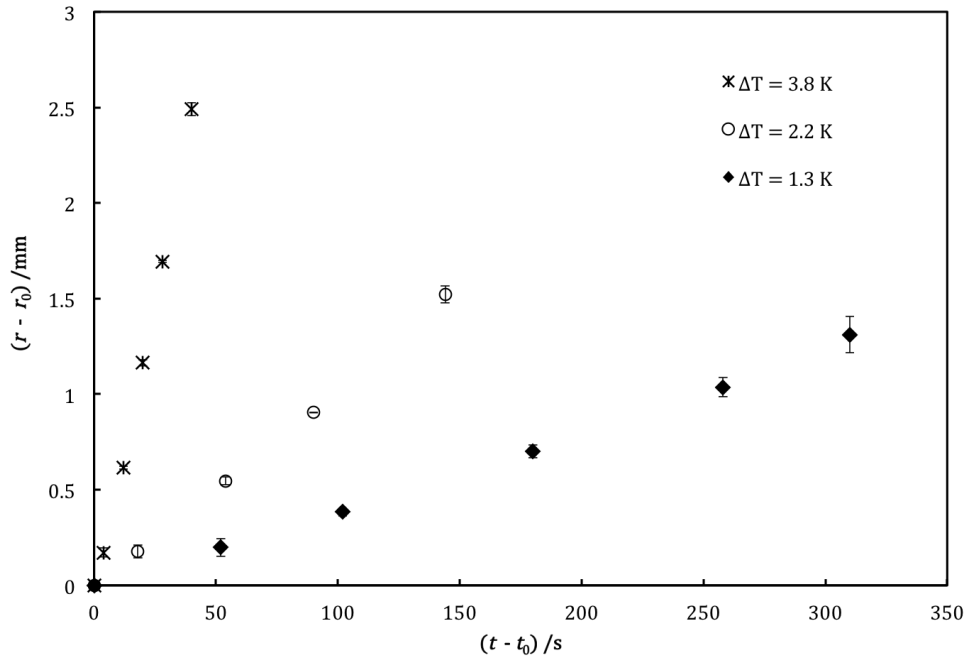

Figure 4.10 – Interface position versus time for methane hydrate films formed on a constant temperature surface at three different driving forces. $p = 4.0$ MPa, $T_{HLV} = 277.5$ K. Film length was determined relative to a fixed point near the origin of the film. The position-time data was plotted relative to the initial position (r_0) and time (t_0). Data points represent the average film length of four measurements in different directions; error bars corresponding to one standard deviation are shown.

of the gradient was set to $T_C = 273.7$ K and the hot end was held at $T_H = 277.7$ K (slightly above $T_{HLV} = 277.5$ K). Since the film growth initiated in the centre of the droplet the plot was divided into two series, growth toward the cold end of the gradient and growth toward the hot end of the gradient. Unlike the constant temperature growth, the position of the interface was not linear with respect to time. The film velocity increased toward the cold end of the temperature gradient and tapered off toward the hot end of the gradient.

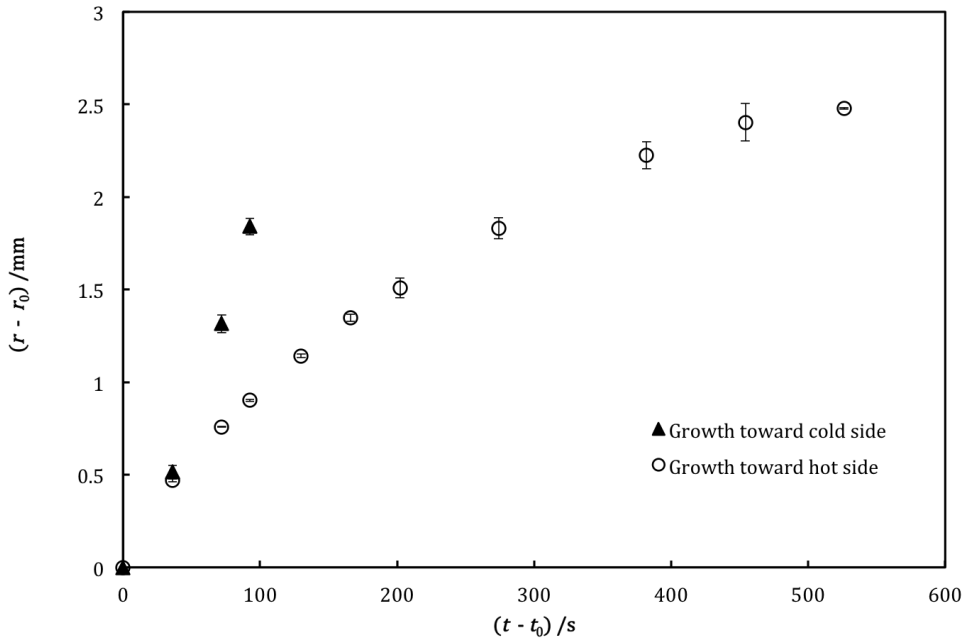

Figure 4.11 – Interface position versus time for a methane hydrate film formed on a temperature gradient, showing growth toward the cold side (T_C = 273.7 K) and the hot side (T_H = 277.7 K) of the gradient. p = 4.0 MPa, T_{HLV} = 277.5 K. Film length was determined relative to a fixed point near the origin of the film. The position-time data was plotted relative to the initial position (r_0) and time (t_0). Data points represent the average film length of three measurements; error bars corresponding to one standard deviation are shown.

4.3 Hydrate Dissociation

The hydrates were dissociated using the temperature gradient controlled by the HP-BTCS. Before dissociation, the temperature gradient was set such that the hot temperature was below the H-L-V equilibrium temperature at the experimental pressure. The boundary setpoint temperatures were then increased simultaneously in equal intervals. This increase in boundary temperatures moved the position of the H-L-V temperature on the stage. The hydrate was observed to dissociate in the region of the stage that was above the H-L-V temperature and remain in the region below the equilibrium temperature. This resulted in the hydrate interface being stationary at the H-L-V

temperature on the stage at a given dissociation step. A typical sequence for the technique is shown in Figure 4.12.

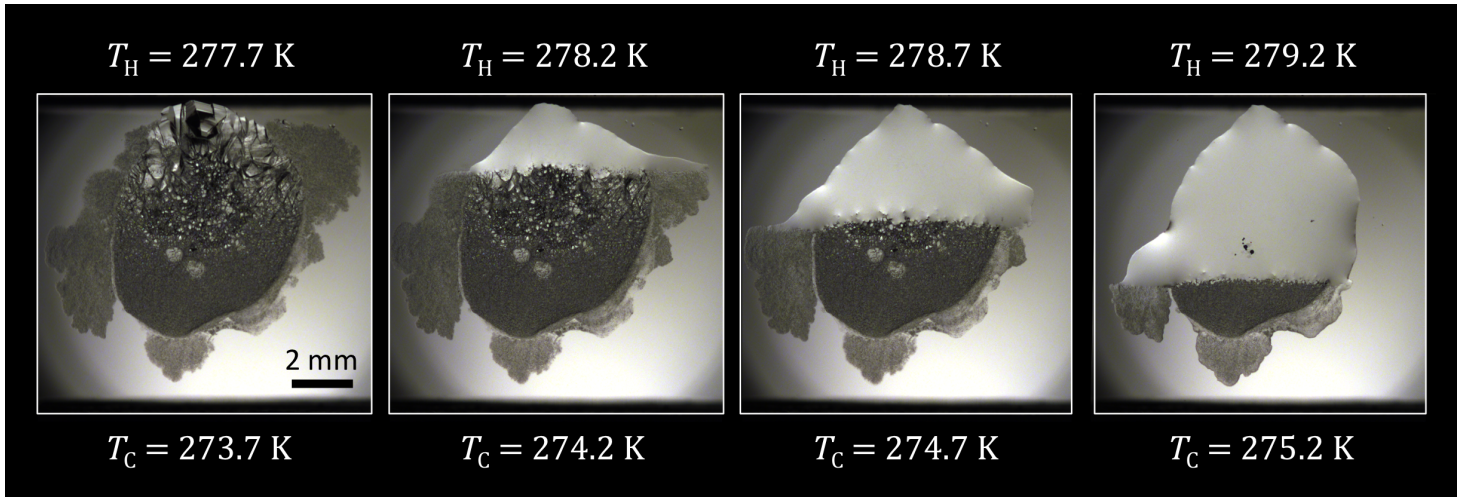

Figure 4.12 – Controlled dissociation sequence of a methane hydrate. The hydrate-water interface appears as a straight line marking the H-L-V temperature. $p = 4.0$ MPa.

Chapter 5

Discussion

In this chapter, the results from the High-Pressure Bilateral Temperature Control Stage (HP-BTCS) experiments are analyzed and discussed. The novel techniques using the HP-BTCS presented in this work are related to characterization and screening of hydrate plug prevention compounds: anti-agglomerates, thermodynamic inhibitors and kinetic inhibitors.

5.1 Morphology

A specific crystal morphology is largely dependant on thermodynamics as well as heat and mass transport. Though factors such as the apparatus, method and experimenter can add significant variation to morphology results, tight control of the system conditions can reduce these variations. Hence, hydrate experimentation with the HP-BTCS was expected to generate reproducible morphologies.

5.1.1 Temperature Control

Typical temperature controlled hydrate formation uses a coolant jacket or bath to control the temperature of the vessel along with the hydrate guest and water (Sloan and Koh, 2008). This can lead to slow temperature response times since the entire pressure vessel must be cooled to the experimental temperature. This slowed response becomes even more apparent for non stirred systems. In this work, a cooling jacket was used to control the temperature of the pressure vessel while the HP-BTCS was used to locally control the temperature of

the sapphire substrate and the water sample within ±0.01°C (Figure 3.1 and Figure 3.2). This design facilitates rapid, precise cooling of the water sample, with response times in the order of seconds.

5.1.2 Driving Force Effects

Uniform Constant Surface Temperature

For the constant temperature experiments, the observed methane hydrate morphologies were comparable to the results of other researchers. As well, we were able to reproduce the reported effect of driving force on hydrate film morphology, where the surface morphology became smoother and more uniform with increasing driving force (Kitamura and Mori, 2013; Li *et al.*, 2014; Saito *et al.*, 2010; Tanaka *et al.*, 2009; Servio and Englezos, 2003a and Beltran and Servio, 2010).

It has been speculated that a transition morphology exists between the uniform, high driving force growth and the faceted, low driving force growth Kitamura and Mori (2013). However, Kitamura and Mori (2013) were not able to reproduce a corresponding transition morphology. The hydrate morphology formed at $\Delta T = 2.0$ K (Figure 4.2) was the best representation of a transition between the uniform growth observed at $\Delta T > 2.3$ K and the faceted growth growth observed at $\Delta T < 1.5$ K. The higher magnification views in Figure 4.3 showed that the transition is due to a decrease in individual grain size. This transition is similar to the crystal size trend reported by Tanaka *et al.* (2009).

Hydrate film growth at the low driving force occurred either by non-uniform lateral growth or by nucleation and attachment of new hydrate crystals to the film. This attachment growth mechanism has also been observed by Li *et al.* (2013). The magnified images of the higher driving forces (Figure 4.3) showed that the hydrate film that appeared to grow uniformly was made up of many small hydrate grains. This implies that the growth occurred by a nucleation and attachment mechanism where the grain size of attached crystals decreased and the number of grains was increased with increasing driving force. This mechanism corresponds to the secondary nucleation model developed by Makogon *et al.* (2007) for methane hydrates, and is a well reported mechanism for crystal growth from supersaturated solutions Mullin (2001).

Constant Gradient Surface Temperature

Previous studies have used individual images of hydrate films formed at a constant driving force to correlate morphology and driving force, similar to the constant surface temperature experiments in this work. As discussed previously, this method can lead to uncertainties regarding transitions in morphology, requiring multiple trial and error runs to obtain a good estimate. The main feature of the HP-BTCS design was that it could apply a temperature gradient to a water sample. This allowed the driving force to vary across a single water sample. The resulting images showed a continuous relation between the driving force and morphology, along with continuous morphological transitions (Figure 4.7 and Figure 4.8). The images showed the significant decrease in crystal size for driving forces from 1.6 to 2.3 K.

Morphology that was representative of a secondary nucleation (polycrystalline) growth mechanism was observed for hydrate growth on the stage where the driving force was above $\Delta T = 1$ K. Detachment of individual hydrate crystals from the interface was observed in the supercooling region from 1 K $\leq \Delta T \leq$ 1.6 K. Makogon *et al.* (2007) stated that this phenomenon occurs when the growth rate is sufficiently slow to allow 'three-dimensional hydrate clusters' to nucleate on and escape from the solidifying interface into the solution, where they independently crystallize and subsequently attach to the interface. At the higher driving forces, and therefore fast growth rates, the clusters nucleated at the interface cannot escape the interface and crystallize attached to the interface. This phenomenon explains why the attachment of secondary crystals was not observed during growth at high driving forces but morphology indicative of secondary crystal growth was observed (at high magnifications) for the hydrate after formation. Growth toward the hot side of the gradient was observed to occur entirely by non-uniform lateral crystal growth below $\Delta T = 1$ K. This was because low driving forces result in fewer nucleation sites with a much slower growth rate (Mullin, 2001), so the probability of independent hydrate crystal formation is small.

5.1.3 Reproducibility

Figure 4.2 and Figure 4.7 show replicates of hydrate morphologies formed on a constant surface temperature using the HP-BTCS. The observed morphologies for a given set of conditions were very reproducible. The only significant variation in surface morphology was due to the number of initial growth points that clustered at the centre of the droplet. Initial growth points were often

observed where small, nearly transparent crystallites had remained in the water after the initial formation-dissociation step. Heating the sample to higher temperatures or for longer periods of time reduced the number of crystallites. Furthermore, it was observed that heating the sample 1 °C above H-L-V for a period of 10 minutes increased induction times to more than several hours. Thus, it would have been desirable to maintain the preheating time (Figure 3.3) constant, presumably obtaining a better control of the number of initial growth points.

5.1.4 Hydrate Propagation onto the Sapphire Surface

All of the experiments in this work showed hydrate growth beyond the original water droplet onto the sapphire surface. This type of growth corresponds to the 'bridge effect' or halo reported by Beltran and Servio (2010). For low degrees of supercooling ($\Delta T < 1.5$ K) the hydrate growth onto the slide propagated with sharp perturbations. As the driving force increased these perturbations became more rounded until they were no longer apparent along the hydrate halo interface. These dendritic-like geometries form due to heat or mass transport limitations (Glicksman, 2012). Though a heat limitation due to the sapphire surface is unlikely because the thermal diffusivity (diffusive transport, $\alpha \sim 1 \times 10^{-5}$ m$^2 \cdot$ s^{-1}) of sapphire surface is high compared to the halo protrusion size (average tip radius) and velocity (advective transport, $L_c \sim 1 \times 10^{-4}$ m and $v_f \sim 1 \times 10^{-5}$ m $\cdot$ s^{-1}) (*i.e.*, the crystal growth Péclet number (Glicksman, 2012) is small for the hydrate growth on the sapphire surface (Equation 5.1)).

$$\begin{aligned} \mathrm{Pe} &= \frac{L_c v_f}{\alpha} \\ &\sim \frac{(1 \times 10^{-4})(1 \times 10^{-5})}{(1 \times 10^{-5})} \\ &\sim 1 \times 10^{-4} \end{aligned} \tag{5.1}$$

5.1.5 Micro-pores

At high magnifications, dark channels − measuring 9 to 14 μm in diameter − became apparent on the surface of the hydrate films (Figure 4.3 and Figure 4.5). These observations seem to support Mori and Mochizuki (1997) water capillarity permeation model for water transport across hydrate films

due to a porous microstructure for gas hydrates. Stern *et al.* (2004) have also noted that hydrates are porous on the micro scale. Hydrate films that grew at higher driving forces exhibited more channels than hydrates formed at low driving forces (Figure 4.3 and Figure 4.5). Channels continued to form as hydrate growth progressed, and this was especially noticeable on the large crystal faces observed at low driving forces. After a few hours, channels covered the entire hydrate surface regardless of the initial formation conditions.

With the instruments used in this study, it was not possible to distinguish the phase present in these channels during hydrate growth. However, it can be speculated that sub-saturated liquid phase fills the channels, as gas bubbles present in the water droplet before hydrate formation slowly disappear after as the hydrate ages. On the contrary, channels appear to grow across the hydrate as it ages. Furthermore, channel propagation occurs regardless of whether gas bubbles were present in the water droplet before formation.

Channels consistently made contact with the sapphire surface at the boundary of the water droplet and were also present in the hydrate halo film on the sapphire surface at low driving forces. It is reasonable to suggest that the pores in the hydrate film could be the transport route for sub-saturated liquid water across the hydrate film to the foreign surface in the halo propagation mechanism proposed by Beltran and Servio (2010).

The increased number of channels at higher driving forces would result in spatially uniform transport of liquid water onto the sapphire surface producing a smooth halo morphology (Figure 4.5). The opposite would explain the dendritic-like halo morphology observed at low driving forces (Figure 4.5), where growth is limited by the transport of sub-saturated liquid water across the hydrate film onto the sapphire surface.

5.1.6 Application

Morphology measurements on a temperature gradient simplify the process to obtain meaningful morphology versus driving force data, since the trend can be observed with a single run. Thus, the HP-BTCS would be a valuable tool to screen additives that modify hydrate grain size and morphology transitions with respect to temperature. Anti-agglomerant evaluation would be a natural candidate for the HP-BTCS, to observe any effect on the transition from continuous crystal growth to adhesive, polycrystalline growth.

5.2 Controlled Hydrate Dissociation

The controlled hydrate dissociation method (Figure 4.12) was important to demonstrate the control over the hydrate interface position - a key factor for the HP-BTCS to operate as a high pressure directional crystallization stage. The dissociation method is also useful as way to measure the temperature gradient across the stage *in situ*, using only the two endpoint thermistors and the position of the interface.

At constant pressure the hydrate interface on the HP-BTCS corresponds to the H-L-V equilibrium temperature isotherm. The solid-liquid interface can be used as a sort of sweeping thermometer that displays the position on the stage of the equilibrium temperature at the system pressure. We can effectively measure the gradient by changing the setpoint temperatures at the boundaries of the gradient and measuring the displacement in the interface.

During the dissociation experiments the step increase in temperature was equal for the cold and hot side. This results in the temperature gradient being equal for each step. Consider this set of linear temperature profiles from dissociation step i to $i+1$:

$$\begin{aligned} T(x) &= g_i x + T_{C,i} \\ T(x) &= g_{i+1} x + T_{C,i+1} \end{aligned} \tag{5.2}$$

Where g_i is the temperature gradient at step i and $T_{C,i}$ is the cold temperature setpoint at step i.

For our system, the interface position ($x_{I,i}$) and the setpoint temperatures ($T_{H,i}$ and $T_{C,i}$) are also known for each dissociation step. Since the temperature gradients are equal for each step, Equation 5.2 can be solved at the hydrate interface where, $T(x_{I,i}) = T_{HLV}$ for g.

$$\begin{aligned} T_{HLV} &= g x_{I,i} + T_{C,i} \\ T_{HLV} &= g x_{I,i+1} + T_{C,i+1} \end{aligned} \tag{5.3}$$

$$\begin{aligned} g &= \frac{T_{C,i+1} - T_{C,i}}{x_{I,i+1} - x_{I,i}} \\ &= \frac{\Delta T_{sp}}{\Delta x_I} \end{aligned} \tag{5.4}$$

Where ΔT_{sp} is the change in the boundary setpoint temperature and Δx_I is the displacement in interface position from step i to $i+1$.

This value of g represents the average temperature gradient over the region traversed by the interface between dissociation steps. For this case, the profile is linear, if the measured gradient is constant between sets of dissociation steps.

For our dissociation experiments the measured gradient was constant between steps, however the measured gradient was consistently lower than that estimated by the setpoint temperatures and the stage gap length (l_{gap})(Equation 5.5).

$$G = \frac{T_H - T_C}{l_{\text{gap}}} \tag{5.5}$$

This implies that the stage gap length scale is smaller than measured (*i.e.*, T_H and T_C are further apart than predicted). This error could be attributed to poor thermistor placement on the stage. For this setup, the thermistors were placed near the centre of the copper plates resulting in a larger separation between the temperature measurement positions compared to the gap between the copper plates. Positioning the thermistors the edge of the copper plates would make the gap length the same for the stage gap and the separation between the thermistors.

Figure 5.1 shows the corrected temperature profile (case II) allowing for temperature profile continuity into copper plates, with a symmetrical correction in the length scale (x_s). The new length scale for the temperature profile was determined by Equation 5.6. Case I in Figure 5.1 corresponds to the temperature profile with the slope given by Equation 5.5.

$$x_s = \frac{T_H - T_C}{g} \tag{5.6}$$

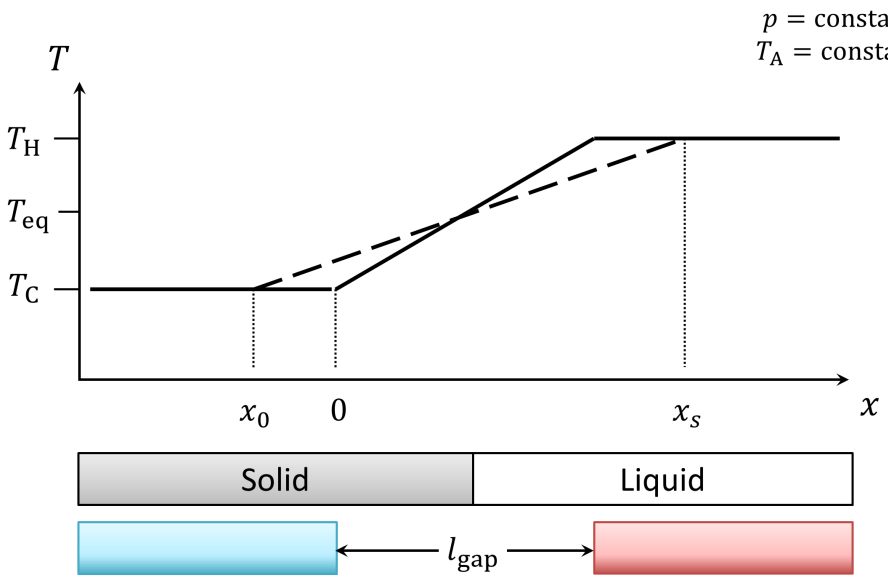

Figure 5.1 – Temperature profiles for the estimated and measured gradients. Case I (solid line) is the profile with the estimated length scale (l_{gap}) and Case II (dashed line) is the profile with the corrected length scale (x_s)

5.2.1 Phase Equilibria

After the temperature profile was measured for the stage, the dissociation experiments were then used to determine the equilibrium temperature (at the system pressure) corresponding to the solid-liquid interface position using Equation 5.7.

$$T_{HLV} = g\left(x_{I,i} + \frac{x_s - l_{\text{gap}}}{2}\right) + T_{C,i} \tag{5.7}$$

The results of phase equilibrium measurements for the dissociation data are summarized in Table 5.1. This value for $H - L_W - V$ agrees within uncertainty with the values compiled by Sloan and Koh (2008) for the methane-water binary system (Table 5.2).

Table 5.1 – Phase equilibrium measurement for methane hydrate. Experimental uncertainties were determined by a coverage factor of $k = 2$ (95% Confidence)

Samples	10
Absolute Pressure	4.043 ± 0.002 MPa
Equilibrium Temperature	277.48 ± 0.16 K

Table 5.2 – Hydrate-Liquid-Vapour phase equilibrium temperature values for methane hydrates at $p = 4.043$ MPa interpolated from data compiled by Sloan and Koh (2008).

	T_{HLV} /K
This Work	**277.48**
de Roo (1983)	277.5
Holder (1987)	277.4
Adisasmito (1991)	277.5
Nakamura (2003)	277.54

5.2.2 Application

The phase equilibrium technique presented here is much simpler and faster than traditional techniques. This is primarily because the equilibrium value is obtained from a stationary interface position as opposed to dynamically searching for dissociation conditions. This method can be used to easily obtain statistically significant data, where each equilibrium measurement requires less than one minute. This would be an excellent assessment tool to quickly compare freezing point depression due to thermodynamic hydrate inhibitors.

5.3 Hydrate Film Velocity

The driving forces used in this work were lower than those studied in the majority of studies available in the open literature for methane hydrate film velocities. The film velocity (v_f) measurements for the constant temperature surface (Figure 4.10) were comparable to those reported by Kitamura and Mori (2013), Taylor *et al.* (2007) and Peng *et al.* (2007) for the medium ($\Delta T = 2.2$ K, $v_f = 10.5 \pm 0.4$ $\mu\text{m} \cdot \text{s}^{-1}$) and high ($\Delta T = 3.8$ K, $v_f = 63.1 \pm 1.7$ $\mu\text{m} \cdot \text{s}^{-1}$) driving forces. Kitamura and Mori noted that they were unable to measure film velocities for the low driving force ($\Delta T = 1.3$ K) films, though our value of 4.2 ± 0.2 $\mu\text{m} \cdot \text{s}^{-1}$ fits within the reported trend. As reported by others (Beltran and Servio, 2010; Kitamura and Mori, 2013; Taylor *et al.*, 2007; Peng *et al.*, 2007 and Freer *et al.*, 2001), film velocity was constant over the period of hydrate growth.

Data for the film velocity of hydrates grown on a constant temperature gradient (Figure 4.11) were unique, since the formation method requires the novel HP-BTCS. As expected, the film velocity was dependent on the position on the stage, with the film accelerating toward the cold side of the gradient and decelerating toward the hot side of the gradient.

The interface position versus time data from Figure 4.11 was correlated with the measured temperature profile across the stage (Equation 5.8) and referenced to the calculated T_{HLV} for the system (see section 5.2). The film velocity was determined by a backward difference from the interface position versus time data (Equation 5.9). Figure 5.2 shows the film velocity versus supercooling.

$$T_{f,i} = g\left(x_{f,i} + \frac{x_s - l_{\text{gap}}}{2}\right) + T_{C,i} \tag{5.8}$$

Where $T_{f,i}$ is the temperature of the liquid ahead of the hydrate film at step i and $x_{f,i}$ is the position of the interface on the stage at step i.

$$v_{f,i,i-1} = \frac{r_{f,i} - r_{f,i-1}}{\Delta t_{i,i-1}} \tag{5.9}$$

Where $v_{f,i,i-1}$ is the average film velocity from step $i-1$ to i, $r_{f,i} - r_{f,i-1}$ is the change in interface position in the direction of growth from step $i-1$ to i and $\Delta t_{i,i-1}$ is the elapsed time from step $i-1$ to i.

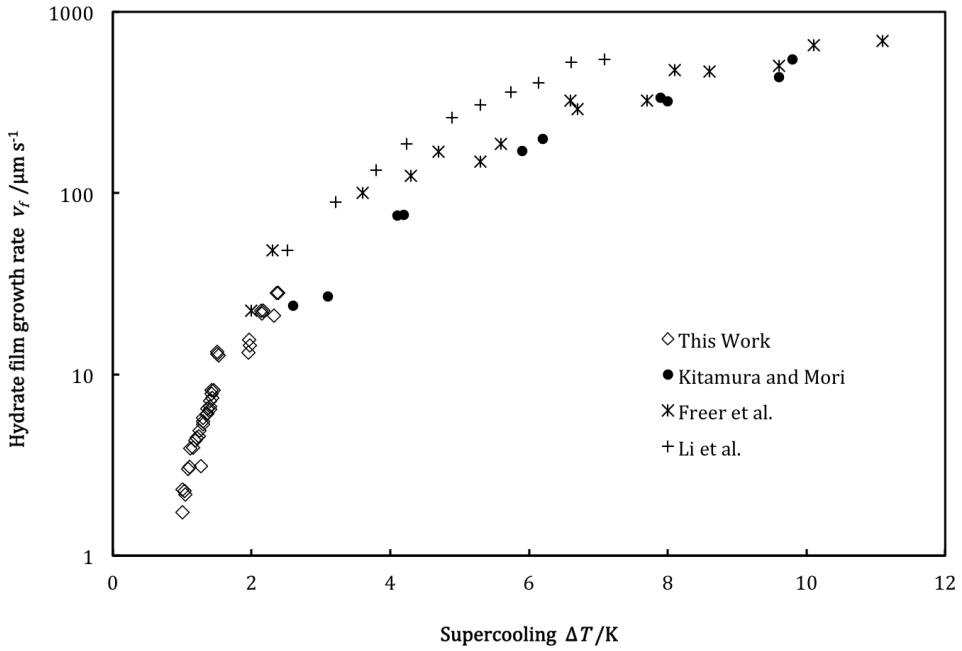

Figure 5.2 – Film velocity versus supercooling for a methane hydrate formed on a temperature gradient. Film velocity was plotted on a logarithmic scale for clarity in the low supercooling region. p = 4.0 MPa, T_C = 273.7 K, T_H = 277.7 K. Film velocity versus supercooling data from Kitamura and Mori (2013), Freer *et al.* (2001) and Li *et al.* (2014) are shown for comparison.

Similar to the continuous morphology analysis on a temperature gradient (see section 5.1.2), film velocity with respect to driving force from was determined from a single experiment. This is in contrast to the traditional method (Figure 4.10), where rate measurements are recorded individually for each driving force to obtain a trend. The temperature gradient method will have a higher uncertainty for temperature compared to the traditional method. This was because temperature was indirectly measured by the method in section 5.2 (as opposed to temperature values obtained directly from a temperature sensor).

5.3.1 Application

The effectiveness of a kinetic hydrate inhibitor can be characterized by its effect on the apparent growth kinetics of the forming hydrate. The HP-BCTS

is capable of measuring apparent kinetics though film velocity measurements like those presented in this work. Compared to traditional methods, the main advantage of the HP-BCTS is that only a single experiment is required to assess changes in the hydrate growth velocity with respect to changes in temperature.

Chapter 6

Conclusions

The objective of the this work was to develop a temperature control stage capable of directional crystallization. The novel, high-pressure, bilateral temperature control stage (HP-BTCS) was designed and used to study gas hydrate growth and dissociation. The design successfully allowed for tight control of the crystallization substrate temperature, independent of the ambient conditions; however, directional crystallization has yet to be tested on the stage.

Using the HP-BTCS, methane hydrate formation was investigated on a surface with a uniform temperature and on a surface with a constant temperature gradient. The uniform temperature experiments showed morphologies with respect to driving force that agreed with data reported by others. The tight control over hydrate formation conditions permitted by the HP-BTCS allowed for closely reproducible film morphologies and the observation of a previously unreported transition point in methane hydrate morphology. A single temperature-gradient experiment showed transitions in morphology with respect to driving force. These transitions were found to be consistently reproducible, and occurred due to a change from continuous crystal growth to polycrystalline, adhesive type growth.

The temperature gradient was also used to successfully control the solid-liquid interface position during gas hydrate dissociation. This is a required feature for the HP-BTCS to function as a high pressure directional crystallization stage. Additionally, the controlled dissociation allowed for the measurement of the temperature gradient and for stationary observations of hydrate-liquid-vapour (H-L-V) equilibrium, providing a simple and fast method for phase equilibrium measurements.

The film velocity was determined for hydrate growth on a uniform temperature surface for three driving forces (p = 4.0 MPa, ΔT = 3.8 K, ΔT = 2.2 K and ΔT = 1.3 K). The measured rates were constant during hydrate formation and were comparable to those reported by others. The film velocity was also determined for hydrate growth on a temperature gradient. The rate was found to accelerate towards the cold end of the stage and decelerate towards the hot end. The temperature gradient was then used to correlate film velocity (apparent growth kinetics) and supercooling with a single formation experiment.

Overall, the ability to observe gas hydrate growth on tightly controlled temperature gradients was found to reduce time consuming multi-trial methods to a single experiment that: (1) quantifies morphology/growth mechanism transitions with respect to temperature, (2) measures the H-L-V equilibrium temperature at the experimental pressure, and (3) correlates the apparent kinetics with respect to temperature. This could be a valuable method to screen the agglomeration, thermodynamic and kinetic effects of a potential hydrate inhibitor/promoter.

6.1 Recommendations for Future Work

Further experiments using the novel HP-BTCS are described below:

1. Considering the speed and simplicity of phase equilibrium measurements using the HP-BTCS, more controlled dissociation experiments should be run at multiple pressures to obtain a complete set of phase equilibria for the methane-water system.
2. The temperature gradient experiments should be repeated at a higher pressure. This will allow for a larger degree of supercooling (above the freezing point of water) at the cold end of the stage. As such, the film velocity measurements will be able to span a larger range of driving forces.
3. The methods described in this work should be repeated for systems with hydrate inhibitors/promoters. The HP-BTCS could be a very useful tool to quickly assess the agglomeration, thermodynamic and kinetic effects.
4. Sapphire is somewhat transparent in the infrared spectrum (up to 5 μm). If possible, thermal (IR) imaging of the stage would be advanta-

geous in order to provide a complete picture of the temperature distribution in the water sample and the stage during hydrate formation.

5. The HP-BTCS was found to be able to control the solid-liquid interface during hydrate dissociation. Temperature controlled, hydrate-formation experiments should be conducted to achieve target growth velocities. The measured film velocities reported in this work should be used as the velocity targets for these experiments. It is possible that the controlled velocity could dictate the resulting hydrate morphology.

Bibliography

Arjmandi, M.; Tohidi, B.; Danesh, A. and Todd, A.C., 2005. Is subcooling the right driving force for testing low-dosage hydrate inhibitors? *Chemical Engineering Science*, **60**: 1313.

ASME, 2010. Boiler and Pressure Vessel Code.

Baumert, J.; Gutt, C.; Shpakov, V.; Tse, J.; Krisch, M.; Müller, M.; Requardt, H.; Klug, D.; Janssen, S. and Press, W., 2003. Lattice dynamics of methane and xenon hydrate: Observation of symmetry-avoided crossing by experiment and theory. *Physical Review B*, **68**: 174301.

Beltrán, J.G. and Servio, P., 2008. Equilibrium studies for the system methane+ carbon dioxide+ neohexane+ water. *Journal of Chemical & Engineering Data*, **53**: 1745–1749.

Beltran, J.G. and Servio, P., 2010. Morphological Investigations of Methane Hydrate Films Formed on a Glass Surface. *Crystal Growth & Design*, **10**: 4339–4347.

Bergeron, S. and Servio, P., 2009. CO_2 and CH_4 mole fraction measurements during hydrate growth in a semi-batch stirred tank reactor and its significance to kinetic modeling. *Fluid phase equilibria*, **276**: 150–155.

Buchanan, P.; Soper, A.K.; Westacott, R.E.; Creek, J.L. and Koh, C.A., 2005. Search for memory effects in methane hydrate: Structure of water before hydrate formation and after hydrate decomposition. *Journal of Chemical Physics*, **123**: 164507.

Christiansen, R.L. and Sloan, E.D., 1994. Mechanisms and kinetics of hydrate formation. *Proc. First International Conference on Gas Hydrates.*

Clarke, M.A. and Bishnoi, P.R., 2005. Determination of the intrinsic kinetics of CO2 gas hydrate formation using in situ particle size analysis. *Chemical Engineering Science*, **60**: 695.

Davidson, D.W.; Garg, S.K.; Gough, S.R.; Handa, Y.P.; Ratcliffe, C.I.; Ripmeester, J.A.; Tse, J.S. and Lawson, W.F., 1986. Laboratory analysis of a naturally occurring gas hydrate from sediment of the Gulf of Mexico. *Geochim. Cosmochim. Acta*, **50**: 619.

Davies, S.R.; Boxall, J.A.; Dieker, L.E.; Sum, A.K.; Koh, C.A.; Sloan, E.D.; Creek, J.L. and Xu, Z.G., 2010. Predicting hydrate plug formation in oil-dominated flowlines. *Journal of petroleum science and engineering*, **72**: 302–309.

Decarie, G., 2012. *A comparative study on the morphology and growth rates of carbon dioxide and methane hydrates*. Master's thesis, Royal Military College of Canada.

Dyadin, Y.A.; Larionov, E.G.; Aladko, E.Y.; Manakov, A.Y.; Zhurko, F.V.; Mikina, T.V.; Komarov, V.Y. and Grachev, E.V., 1999. Clathrate formation in water-noble gas (hydrogen) systems at high pressures. *Journal of Structural Chemistry*, **40**: 790.

Englezos, P. and Bishnoi, P., 1988. Prediction of gas hydrate formation conditions in aqueous electrolyte solutions. *AIChE journal*, **34**: 1718–1721.

Englezos, P.; Kalogerakis, N.; Dholabhai, P.D. and Bishnoi, P.R., 1987. Kinetics of formation of methane and ethane gas hydrates. *Chemical Engineering Science*, **42**: 2647.

Eslamimanesh, A.; Mohammadi, A.; Richon, D.; Naidoo, P. and Ramjugernath, D., 2011. Application of gas hydrate formation in separation processes: A review of experimental studies. *Journal of Chemical Thermodynamics*, **46**: 62–71.

Florusse, L.J.; Peters, C.J.; Schoonman, J.; Hester, K.C.; Koh, C.A.; Dec, S.F.; Marsh, K.N. and Sloan, E.D., 2004. Stable low-pressure hydrogen clusters stored in a binary clathrate hydrate. *Science*, **306**: 469.

Freer, E.M.; Sami Selim, M. *et al.*, 2001. Methane hydrate film growth kinetics. *Fluid Phase Equilibria*, **185**: 65–75.

Glicksman, M.E., 2012. Mechanism of dendritic branching. *Metallurgical and Materials Transactions A*, **43**: 391–404.

Gudmundsson, J.S. and Borrehaug, A., 1996. Frozen hydrate for transport of natural gas. *Proc. Second International Conference on Gas Hydrates*.

Gupta, A.; Lachance, J.; Sloan, E. and Koh, C., 2008. Measurements of methane hydrate heat of dissociation using high pressure differential scanning calorimetry. *Chemical Engineering Science*, **63**: 5848–5853.

Haynes, W.M., 2012. *CRC handbook of chemistry and physics*. CRC press.

Hester, K. and Brewer, P., 2009. Clathrate hydrates in nature. *Annual review of marine science*, **1**: 303–327.

Hong, H. and Pooladi-Darvish, M., 2005. Simulation of depressurization for gas production from gas hydrate reservoirs. *Journal of Canadian Petroleum Technology*, **44**.

Howe, S.; Nanchary, N.; Patil, S.; Ogbe, D.; Chukwu, G.; Hunter, R. and Wilson, S., 2004. Economic analysis and feasibility study of gas production from Alaska North Slope gas hydrate resources. *Natural Gas Hydrates: Energy Resource Potential and Associated Geologic Hazards*.

Incropera, F.P., 2011. *Fundamentals of heat and mass transfer*. John Wiley & Sons.

Kang, S.P. and Lee, H., 2000. Recovery of CO2 from flue gas using gas hydrate: thermodynamic verification through phase equilibrium measurements. *Environmental Science and Technology*, **34**: 4397.

Kelland, M.A., 2006. History of the development of low dosage hydrate inhibitors. *Energy & Fuels*, **20**: 825–847.

Kitamura, M. and Mori, Y.H., 2013. Clathrate-hydrate film growth along water/methane phase boundaries an observational study. *Crystal Research and Technology*, **48**: 511–519.

Klauda, J. and Sandler, S., 2005. Global distribution of methane hydrate in ocean sediment. *Energy & Fuels*, **19**: 459–470.

Kneafsey, T.; Tomutsa, L.; Moridis, G.; Seol, Y.; Freifeld, B.; Taylor, C. and Gupta, A., 2005. Methane Hydrate Formation and Dissocation in a Partially Saturated Sand–Measurements and Observations. Technical report, Ernest Orlando Lawrence Berkeley National Laboratory, Berkeley, CA (US).

Kneafsey, T.; Tomutsa, L.; Moridis, G.; Seol, Y.; Freifeld, B.; Taylor, C. and Gupta, A., 2007. Methane hydrate formation and dissociation in a partially saturated core-scale sand sample. *Journal of Petroleum Science and Engineering*, **56**: 108–126.

Kobayashi, T.; Imura, N.; Ohmura, R. and Mori, Y.H., 2007. Clathrate hydrate formation by water spraying in a methane+ ethane+ propane gas mixture: Search for the rate-controlling mechanism of hydrate formation in the presence of methylcyclohexane. *Energy & fuels*, **21**: 545–553.

Koh, C.A.; Sum, A.K. and Sloan, E.D., 2012. State of the art: natural gas hydrates as a natural resource. *Journal of Natural Gas Science and Engineering*, **8**: 132–138.

Körber, C.; Rau, G.; Cosman, M. and Cravalho, E., 1985. Interaction of particles and a moving ice-liquid interface. *Journal of Crystal Growth*, **72**: 649–662.

Kvenvolden, K., 2002. Methane hydrate in the global organic carbon cycle. *Terra Nova*, **14**: 302–306.

Lederhos, J.P.; Long, J.P.; Sum, A.; Christiansen, R.L. and Sloan, E.D., 1996. Effective kinetic inhibitors for natural gas hydrates. *Chemical Engineering Science*, **51**: 1221.

Lee, J.D.; Lee, Y.C.; JO, H.H. and Hu-Kab, C., 2010. Gas hydrate reactor comprising thermoelectric module. US Patent App. 12/916,278.

Li, S.L.; Sun, C.Y.; Liu, B.; Feng, X.J.; Li, F.G.; Chen, L.T. and Chen, G.J., 2013. Initial thickness measurements and insights into crystal growth of methane hydrate film. *AIChE Journal*, **59**: 2145–2154.

Li, S.L.; Sun, C.Y.; Liu, B.; Li, Z.Y.; Chen, G.J. and Sum, A.K., 2014. New Observations and Insights into the Morphology and Growth Kinetics of Hydrate Films. *Scientific reports*, **4**.

Linga, P.; Kumar, R. and Englezos, P., 2007. Gas hydrate formation from hydrogen/carbon dioxide and nitrogen/carbon dioxide gas mixtures. *Chemical Engineering Science*, **62**: 4268–4276.

Liu, Z.; Muldrew, K.; Wan, R.G. and Elliott, J.A., 2003. Measurement of freezing point depression of water in glass capillaries and the associated ice front shape. *Physical Review E*, **67**: 061602.

Long, J.P. and Sloan, E.D., 1996. Hydrates in the ocean and evidence for the location of hydrate formation. *Int. J. Thermophysics*, **17**: 1.

Maeda, N.; Wells, D.; Becker, N.C.; Hartley, P.G.; Wilson, P.W.; Haymet, A.D.J. and Kozielski, K.A., 2011. Development of a high pressure automated lag time apparatus for experimental studies and statistical analyses

of nucleation and growth of gas hydrates. *Proc. Seventh International Conference on Gas Hydrates*.

Makogon, I., 1997. *Hydrates of hydrocarbons*. Pennwell Corporation.

Makogon, Y.F., 1981. *Hydrates of Natural Gas*. PennWell Books, Tulsa.

Makogon, Y.F.; Melikhov, I.; Kozlovskaya, E. and BozhevolNov, V., 2007. Secondary nucleation in the formation of methane crystal hydrate. *Russian Journal of Physical Chemistry A*, **81**: 1645–1649.

Malone, R., 1985. Gas hydrates topical report. *DOE/METC/SP-218, US Department of Energy*: 33–50.

Mao, W.L.; Mao, H.K.; Goncharov, A.F.; Stuzhkin, V.V.; Guo, Q.Z.; Hu, J.Z.; Shu, J.F.; J., R.; Hemley; Somayazulu, M. and Zhao, Y.S., 2002. Hydrogen clusters in clathrate hydrate. *Science*, **297**: 2247.

Miers, H.A. and Isaac, F., 1907. The Spontaneous Crystallisation of Binary Mixtures. Experiments on Salol and Betol. *Proc. Roy. Soc. Lond.*, **A79**: 322.

Mochizuki, T. and Mori, Y.H., 2006. Clathrate hydrate film growth along water/hydrate former phase boundaries numerical heat-transfer study. *Journal of Crystal Growth*, **290**: 642.

Mohammadi, A.; Tohidi, B. and Burgass, R., 2003. Equilibrium data and thermodynamic modeling of nitrogen, oxygen, and air clathrate hydrates. *Journal of Chemical & Engineering Data*, **48**: 612–616.

Mori, Y.H. and Mochizuki, T., 1997. Mass transport across clathrate hydrate films a capillary permeation model. *Chemical engineering science*, **52**: 3613–3616.

Moridis, G.; Seol, Y. and Kneafsey, T., 2005. Studies of reaction kinetics of methane hydrate dissociation in porous media. In *Fifth International Conference on Gas Hydrates*.

Moudrakovski, I.L.; McLaurin, G.E.; Ratcliffe, C.I. and Ripmeester, J.A., 2004. Methane and carbon dioxide hydrate formation in water droplets: Spatially resolved measurements from magnetic resonance microimaging. *Journal of Physical Chemistry B*, **108**: 17591.

Mullin, J.W., 2001. *Crystallization*. Butterworth-Heinemann.

Muraoka, M. and Nagashima, K., 2012. Pattern Variety of Tetrahydrofuran Clathrate Hydrates Formed in Porous Media. *The Journal of Physical Chemistry C*.

Ohmura, R.; Ogawa, M.; Yasuka, K. and Mori, Y.J., 2003. Statistical study of clathrate-hydrate nucleation in a water/hydrochlorofluorocarbon system: Search for the nature of the memory effect. *Journal of Physical Chemistry B*, **107**: 5289.

Park, Y.; Kim, D.; Lee, J.; Huh, D.; Park, K.; Lee, J. and Lee, H., 2006. Sequestering carbon dioxide into complex structures of naturally occurring gas hydrates. *Proceedings of the National Academy of Sciences*, **103**: 12690–12694.

Peng, B.; Dandekar, A.; Sun, C.; Luo, H.; Ma, Q.; Pang, W. and Chen, G., 2007. Hydrate film growth on the surface of a gas bubble suspended in water. *The Journal of Physical Chemistry B*, **111**: 12485–12493.

Radler, M., 2000. World crude and natural gas reserves rebound in 2000. *Oil & Gas Journal*, **98**: 121–123.

Rawn, C.; Rondinone, A.; Chakoumakos, B.; Circone, S.; Stern, L.; Kirby, S. and Ishii, Y., 2003. Neutron powder diffraction studies as a function of temperature of structure II hydrate formed from propane. *Canadian Journal of Physics*, **81**: 431–438.

Rehder, G.; Kirby, S.; Durham, B.; Stern, L.; Peltzer, E.T.; Pinkston, J. and Brewer, P., 2004. Dissolution rates of pure methane hydrate and carbon-dioxide hydrate in undersaturated seawater at 1000-m depth. *Geochimica et Cosmochimica Acta*, **68**: 285.

Ripmeester, J.A.; John, S.T.; Ratcliffe, C.I. and Powell, B.M., 1987. A new clathrate hydrate structure. *Nature*, **325**: 135–136.

Rodger, M., 2000. Gas Hydrates: Challenges for the Future. *Ann. NY Acad. Sci.*: 474.

Rubinsky, B. and Ikeda, M., 1985. A cryomicroscope using directional solidification for the controlled freezing of biological material. *Cryobiology*, **22**: 55–68.

Saito, K.; Kishimoto, M.; Tanaka, R. and Ohmura, R., 2010. Crystal growth of clathrate hydrate at the interface between hydrocarbon gas mixture and liquid water. *Crystal Growth & Design*, **11**: 295–301.

Servio, P. and Englezos, P., 2002. Measurement of dissolved methane in water in equilibrium with its hydrate. *Journal of Chemical & Engineering Data*, **47**: 87–90.

Servio, P. and Englezos, P., 2003a. Morphology of methane and carbon dioxide hydrates formed from water droplets. *AIChE Journal*, **49**: 269.

Servio, P. and Englezos, P., 2003b. Morphology study of structure H hydrate formation from water droplets. *Crystal Growth & Design*, **3**: 61.

Sloan, E.D. and Koh, C.A., 2008. *Clathrate Hydrates of Natural Gases*. CRC Press, Boca Raton, FL.

Sloan, E.D., 2003. Fundamental principles and applications of natural gas hydrates. *Nature*, **426**: 353–363.

Soloviev, V., 2002. Global estimation of gas content in submarine gas hydrate accumulations. *Russian Geology and Geophysics*, **43**: 609–624.

Song, K.Y.; Kobayashi, R. *et al.*, 1987. Water content of CO2 in equilibrium with liquid water and/or hydrates. *SPE Formation Evaluation*, **2**: 500–508.

Staykova, D.; Kuhs, W.; Salamatin, A. and Hansen, T., 2003. Formation of porous gas hydrates from ice powders: diffraction experiments and multi-stage model. *The Journal of Physical Chemistry B*, **107**: 10299–10311.

Stern, L.A.; Kirby, S.H. and Durham, W.B., 2003. Temperature, pressure, and compositional effects on anomalous or self preservation of gas hydrates. *Canadian Journal of Physics*, **81**: 271.

Stern, L.A.; Kirby, S.H.; Circone, S. and Durham, W.B., 2004. Scanning electron microscopy investigations of laboratory-grown gas clathrate hydrates formed from melting ice, and comparison to natural hydrates. *American Mineralogist*, **89**: 1162–1175.

Sum, A.K.; Burruss, R.C. and Sloan, E.D., 1997. Measurement of clathrate hydrates via Raman spectroscopy. *The Journal of Physical Chemistry B*, **101**: 7371–7377.

Susilo, R.; Ripmeester, J.A. and Englezos, P., 2007. Characterization of gas hydrates with PXRD, DSC, NMR, and Raman spectroscopy. *Chemical engineering science*, **62**: 3930–3939.

Suzuki, T.; Muraoka, M. and Nagashima, K., 2011. Foreign particle behavior at the growth interface of tetrahydrofuran clathrate hydrates. *Journal of Crystal Growth*, **318**: 131–134.

Tanaka, R.; Sakemoto, R. and Ohmura, R., 2009. Crystal growth of clathrate hydrates formed at the interface of liquid water and gaseous methane, ethane, or propane: variations in crystal morphology. *Crystal Growth and Design*, **9**: 2529–2536.

Taylor, C.J.; Miller, K.T.; Koh, C.A. and Sloan Jr, E.D., 2007. Macroscopic investigation of hydrate film growth at the hydrocarbon/water interface. *Chemical Engineering Science*, **62**: 6524–6533.

Thompson, H.; Soper, A.; Buchanan, P.; Aldiwan, N.; Creek, J. and Koh, C., 2006. Methane hydrate formation and decomposition: Structural studies via neutron diffraction and empirical potential structure refinement. *The Journal of chemical physics*, **124**: 164508.

Tréhu, A.; Ruppel, C.; Holland, M.; Dickens, G.; Torres, M.; Collett, T.; Goldberg, D.; Riedel, M. and Schultheiss, P., 2006. Hydrates. *Oceanography*, **19**: 124.

Trofimuk, A.; Cherskiy, N. and Tsarev, V., 1973. Accumulation of natural gases in zones of hydrate formation in the hydrosphere. *Doklady Akademii Nauk SSSR*, **212**: 931–934.

Tulk, C.; Ripmeester, J. and Klug, D., 2000. The application of Raman spectroscopy to the study of gas hydrates. *Annals of the New York Academy of Sciences*, **912**: 859–872.

Turner, D.; Miller, K. and Sloan, E., 2009. Direct conversion of water droplets to methane hydrate in crude oil. *Chemical Engineering Science*, **64**: 5066–5072.

Uhlmann, D.; Chalmers, B. and Jackson, K., 1964. Interaction Between Particles and a Solid-Liquid Interface. *Journal of applied physics*, **35**: 2986–2993.

Vysniauskas, A. and Bishnoi, P., 1983. A kinetic study of methane hydrate formation. *Chemical Engineering Science*, **38**: 1061–1072.

Waite, W., 2002. Thermal conductivity measurements in porous mixtures of methane hydrate and quartz sand. *Geophysical Research Letters*, **29**: 2229.

Wilson, P.W.; Lester, D. and Haymet, A.D.J., 2005. Heterogeneous nucleation of clathrates from supercooled tetrahydrofuran (THF)/water mixtures, and the effect of an added catalyst. *Chemical Engineering Science*, **60**: 2937.

Winters, W.; Pecher, I.; Waite, W. and Mason, D., 2004. Physical properties and rock physics models of sediment containing natural and laboratory-formed methane gas hydrate. *American Mineralogist*, **89**: 1221–1227.

Xu, Y.; Zeng, Y.; Ding, J. and YANG, X., 2007. Progresses on Researches of Gas Hydrate Anti-agglomerates. *Natural Gas Industry*, **27**: 102.

Yamamoto, Y.; Komai, T.; Kawamura, T.; Yoon, J.H.; Kang, S.P. and Okita, S., 2002. Studies on the separation and purification of guest component. *Proc. Fourth International Conference on Gas Hydrates*, **19**: 428.

Yousif, M., 1998. Effect of underinhibition with methanol and ethylene glycol on the hydrate-control process. *SPE Production & Facilities*, **13**: 184–189.

Zerpa, L.E.; Sloan, E.D.; Sum, A.K. and Koh, C.A., 2012. Overview of CSMHyK: A transient hydrate formation model. *Journal of Petroleum Science and Engineering*, **98**: 122–129.

Appendix A

Directional Crystallization Stage Design

The temperature controlled directional crystallization method proposed in this work does not use a motor to control crystal growth rate. Thermoelectric cooler modules (TECs) will be used for temperature control on opposite sides of a thermally conductive substrate. This assembly is the temperature control stage that will hold and crystallize the sample. The TECs will be controlled individually by PID controllers. The high and low temperatures (T_H and T_C) at either end of the stage can be set such that the solid-liquid equilibrium temperature for the crystallizing system lies between them. This allows for stationary observation of the solid-liquid interface. Changing the set point at either end of the stage will result in a displacement in the solid-liquid interface. The crystal growth rate (v_f) should be proportional to the rate of change in the the high and low setpoints ($\Delta T_{sp,H}$ and $\Delta T_{sp,C}$) over the temperature gradient (Equation A.1). This compact setup can easily be fitted into a pressure vessel to study hydrate systems with gasses like methane or carbon dioxide.

$$v_f = \frac{dx_I}{dt} \propto \frac{{}^{dT_{sp}}/_{dt}}{G(x)} \tag{A.1}$$

where v_f is the crystal growth rate, x_I is the position of the solid-liquid interface, ${}^{dT_{sp}}/_{dt}$ is the rate of change in the setpoint temperature and $G(x)$ is the temperature gradient.

To simplify measurements with this method, the temperature gradient must be constant. A constant gradient is achieved when the gap is small. Though,

a larger gap provides a larger viewing area for video acquisition. The maximum gap length will be larger if the slide material has a high thermal conductivity. The desired temperature profile over the gap length is shown in Figure A.1.

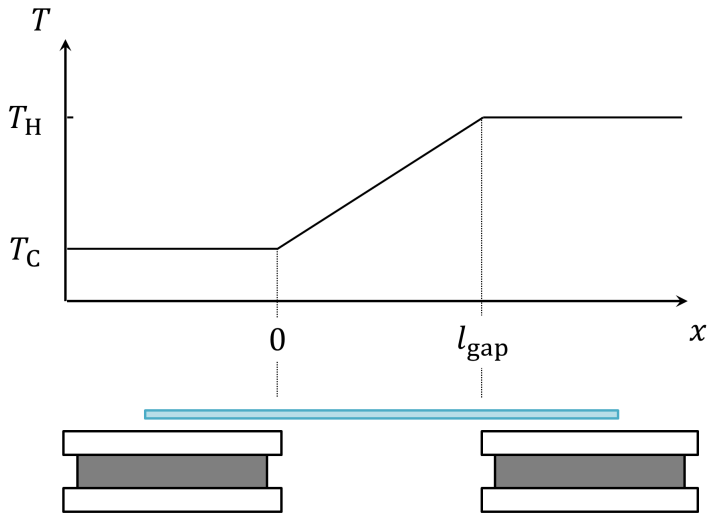

Figure A.1 – Temperature profile for the High Pressure Bilateral Temperature Control Stage

A.1 Heat Transfer

A.1.1 Stage

A simple heat transfer model was set up for this stage to determine the maximum gap length. Non-dimensional temperature and length are defined in Equation A.2 and Equation A.3 respectively.

$$\theta(x) = \frac{T(x) - T_C}{T_H - T_C} \tag{A.2}$$

$$\xi = \frac{x}{l_{gap}} \tag{A.3}$$

where x is the position on the slide, l_{gap} is the gap length, $T(x)$ is the temperature at point x and T_C and T_H are the cold and hot end temperatures.

The heat transfer through the slide can be considered one-dimensional if the Biot number for the slide and the surroundings is small (Equation A.4). Assuming constant properties, Equation A.5 is the one-dimensional, steady state, macroscopic heat balance for the slide.

$$\mathrm{Bi} = \frac{h_a t}{k_s} \tag{A.4}$$

where t is the thickness of the slide, h_a is the average heat transfer coefficient for free convection of the surrounding atmosphere and k_s is the thermal conductivity of the slide.

$$\frac{d^2\theta}{d\xi^2} - m^2(\theta - \theta_\infty) = 0 \tag{A.5}$$

$$m = l_{gap}\sqrt{\frac{2h_a}{k_s t}} \tag{A.6}$$

where θ_∞ is the non-dimensional temperature surrounding the slide.

For imaging, the slide is required to be transparent. As such, sapphire was chosen as the slide material for its high thermal conductivity and transparency.

Equation A.5 was then solved for $\theta(\xi)$ with boundary conditions $\theta(\xi = 0) = 1$ and $\theta(\xi = 1) = 0$. Figure A.2 shows the temperature profile in a sapphire slide as the gap length was increased. The temperature profile was determined to be sufficiently linear for a gap length of 10 mm.

Figure A.3 is a simple schematic of the High Pressure Bilateral Temperature Control Stage (HP-BTCS) design. A sapphire slide bridges the two bases of the stage. Each base consists of a TEC between two copper plates. The copper plates evenly distribute heat onto the sample slide and the heat sink. A thermistor is used on each side of the stage to output temperature reading to a PID controller.

A.1.2 Water Droplet

To assess the heat transfer through the water sample uniformly cooled (*i.e.*, no temperature gradient) by the sapphire stage, a one-dimensional micro-

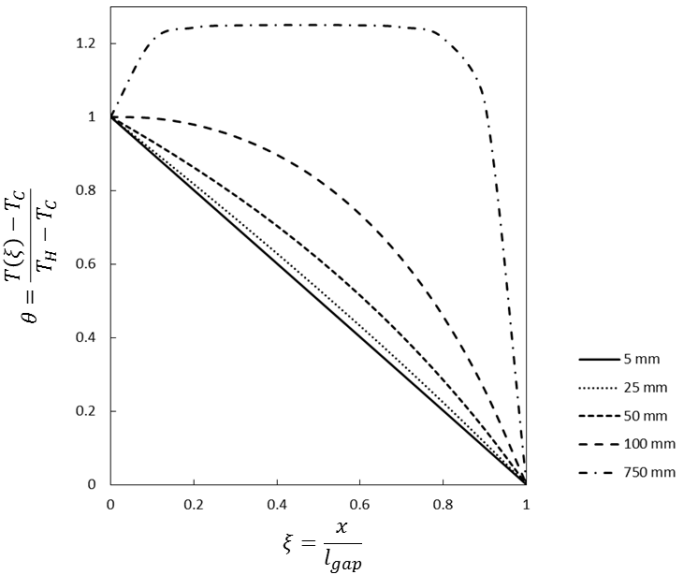

Figure A.2 – Calculated temperature profile along the TEM stage for different gap lengths for the case when $T_\infty > T_H$. Note that $\theta = 1$ represents T_H and $\theta = 0$ represents T_C.

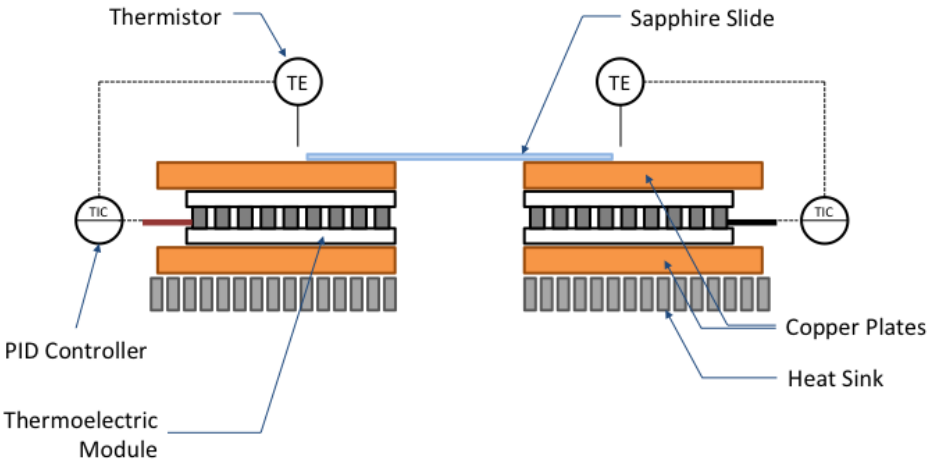

Figure A.3 – Schematic of the High Pressure Bilateral Temperature Control Stage

scopic heat balance was used to estimate the temperature at the apex of a water droplet. Figure A.4 is a schematic of the temperature profile in the z-direction (normal the sapphire surface) for the maximum thickness of the water droplet.

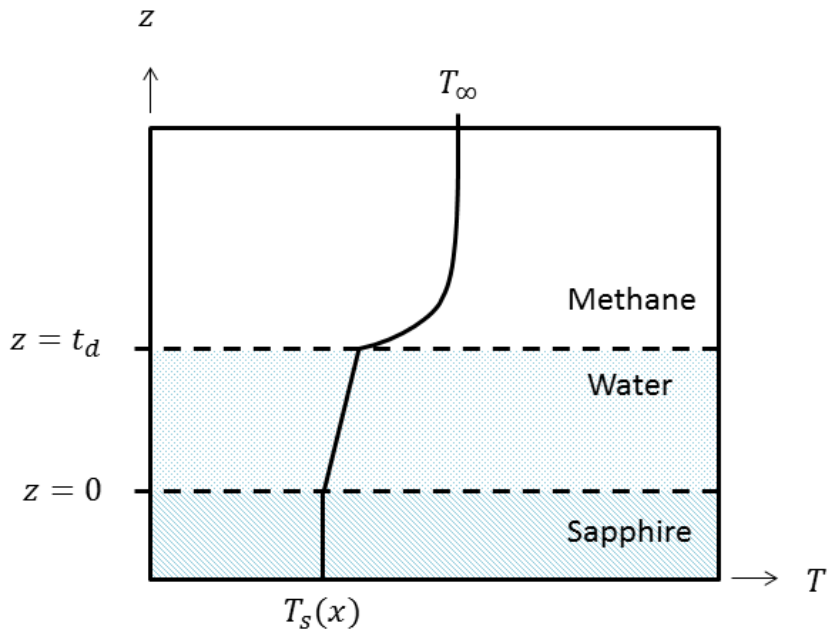

Figure A.4 – Schematic of the temperature profile in the direction normal the HP-BTCS for the maximum thickness of the water droplet

Non-dimensional temperature and length are defined in Equation A.7 and Equation A.8 respectively.

$$\theta(z) = \frac{T(z) - T_\infty}{T_s - T_\infty} \tag{A.7}$$

$$\zeta = \frac{z}{t_d} \tag{A.8}$$

where z is the position in the water sample, t_d is the thickness of the water sample, $T(z)$ is the temperature at point z, T_s is the sapphire surface temperature and T_∞ is the bulk temperature of the surrounding atmosphere.

The steady state balance for the water phase is:

$$\frac{d^2\theta}{d\zeta^2} = 0 \tag{A.9}$$

The corresponding sapphire temperature and convective boundary conditions are given by Equation A.10 and Equation A.11 respectively.

$$\theta(0) = 1 \tag{A.10}$$

$$-\frac{k_l}{t_d}\left.\frac{d\theta}{d\zeta}\right|_{\zeta=1} = h_a\ \theta(1) \tag{A.11}$$

where k_l is the thermal conductivity of the water.

From Equation A.9 and Equation A.10, the dimensionless gradient in the water droplet is given by Equation A.12.

$$\frac{d\theta}{d\zeta} = \theta(1) - 1 \tag{A.12}$$

Substituting Equation A.12 into Equation A.11 gives an expression for the dimensionless surface temperature of the water in terms of the Biot number for the water and surrounding atmosphere (Equation A.13 and Equation A.14). The difference in temperature from the sapphire surface to the water droplet surface (ΔT_s) is given by Equation A.15.

$$\theta(1) = \frac{1}{\mathrm{Bi} + 1} \tag{A.13}$$

$$\mathrm{Bi} = \frac{h_a t_d}{k_l} \tag{A.14}$$

$$\Delta T_s = \left(\frac{1}{\mathrm{Bi} + 1} - 1\right)(T_s(x) - T_\infty) \tag{A.15}$$

Example

Table A.1 summarizes the conditions for a water sample cooled on the stage pressurized in an atmosphere of methane and the estimated temperature difference across the water sample.

Table A.1 – Summary of the heat transfer conditions and the estimated maximum temperature difference across the water droplet

p	4.0	MPa
T_s	2.5	°C
T_∞	4.5	°C
t_d	1.2	mm
h_a	19	$\mathrm{Wm^{-2}K^{-1}}$
k_l	0.56	$\mathrm{Wm^{-1}K^{-1}}$
Bi	0.04	
ΔT_s	0.08	°C

Thermodynamic properties for water and methane were obtained from the CRC Handbook (Haynes, 2012). Correlations used for h_a were obtained from Incropera (2011).

Appendix B

Pressure Vessel Design

This appendix outlines the design requirements and stress analysis calculations for the pressure vessel to hold the High-Pressure Bilateral Temperature Control Stage (HP-BTC). The calculations follow those outlined in the ASME Boiler and Pressure Vessel Code (BPVC) (ASME, 2010).

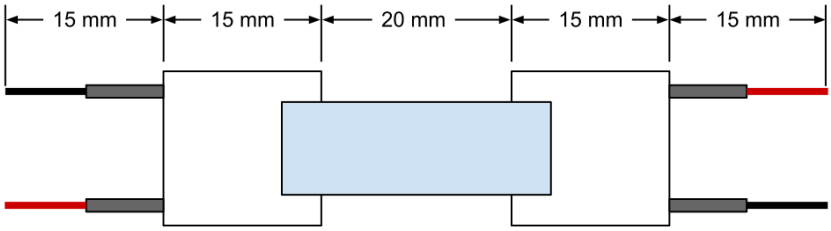

Figure B.1 – Thermoelectric cooler modules and sapphire slide with relevant dimensions

B.1 Design Requirements

The inside radius of the vessel must be large enough to fit the stage with the thermoelectric cooler modules in various orientations (dimensions are shown in Figure B.1). The design pressure must be greater than the most severe pressure expected in normal operation.

Table B.1 – Design requirements for the TEM Stage Vessel

Inside Radius	R_i	1.625 in.
Internal Pressure	P	3000 psi

B.2 Stress Analysis

B.2.1 Material Properties

The material selection is summarized in Table B.2. 316 Stainless steel was chosen as the body material for its corrosion resistance and high strength. The bolting material was chosen to be the same as the vessel to reduce corrosion between the two. Buna-N was selected as the o-ring material for its low cost and compatibility with hydrocarbons like methane. Sapphire was selected as the window material because of its high transmittance in the visual spectrum, making it ideal for the optical measurements required. The sapphire widows are housed in a 1 inch male NPT fitting. Since this is a pre-manufactured part, the calculations for the windows only concerns the threaded holes required in the lid and bottom of the vessel.

Material properties were obtained from the BPVC Section II and Appendix 2. The metal properties are shown in Table B.3 and the o-ring properties are in Table B.4. The design stress intensity values, which include a factor of safety, were used in the stress analysis calculations.

Table B.2 – Vessel component materials

Vessel	**Bolts**	**O-ring**	**Sight Windows**
316 Stainless Steel	316 Stainless Steel	Buna-N	Sapphire

B.2.2 Corrosion Allowance

The vessel may at some point be cooled in a bath of ethylene glycol and water (50 % (v/v) solution). This environment is not very corrosive to 316 Stainless Steel. However, additional material must be added to the minimum required thickness at account for any possible corrosion over time. This allowance is calculated in Table B.5. Corrosion values were obtained from the BPVC Section II.

Table B.3 – Allowable stress for bolting and vessel materials at 37.8°C

Vessel	**316 Stainless Steel**		
	Maximum Allowable Stress	σ	30 000 psi
	Design Stress	S	10 000 psi
	Factor of Safety	sf	3
Bolts	**316 Stainless Steel**		
	Maximum Allowable Stress	σ	30 000 psi
	Design Stress	S_B	10 000 psi
	Factor of Safety	sf	3

Table B.4 – O-ring properties

Yield Point Stress	y	900 psi
Gasket Seating Factor	m	1

Table B.5 – Corrosion allowance for 316 stainless steel

Corrosion	2 mil/year
Vessel Lifespan	20 years
Allowance	0.0400 in.

B.2.3 Thin Walled Vessel

Nomenclature

E	Weld joint efficiency
P	Design pressure
R_i	Vessel inside radius
R_o	Vessel outside radius
S	Design stress
t	Minimum required thickness or design thickness
t_{sc}	Minimum required thickness plus corrosion allowance

Assumptions:
(1) the minimum required thickness is less than 1/10 R_i

Maximum Stress
The design thickness is the greater of that required by circumferential stress

(Equation B.1) or longitudinal stress (Equation B.2) (BPVC, Section VIII, Division 1, Part UG-27).

Circumferential Stress

$$\begin{aligned} t &= \frac{PR_i}{SE - 0.6P} \\ &= \frac{(3000)(1.625)}{(10000)(1) - 0.6(3000)} \frac{[\text{psi}][\text{in.}]}{[\text{psi}]} \\ &= 0.5945 \text{ in.} \end{aligned} \tag{B.1}$$

Longitudinal Stress

$$\begin{aligned} t &= \frac{PR_i}{2SE - 0.4P} \\ &= \frac{(3000)(1.625)}{2(10000)(1) - 0.4(3000)} \frac{[\text{psi}][\text{in.}]}{[\text{psi}]} \\ &= 0.2593 \text{ in.} \end{aligned} \tag{B.2}$$

The circumferential stress dominates. Therefore the minimum required thickness for a thin vessel is 0.5945". Allowing for corrosion this becomes:

$t_{sc} = 0.6339$ in.

However, t is larger than 1/10 R_i, which makes assumption (1) not valid. Therefore thick vessel calculations must be used.

B.2.4 Thick Walled Vessel

Nomenclature

E	Weld joint efficiency
P	Design pressure
R_i	Vessel inside radius
R_o	Vessel outside radius
S	Design stress
t	Minimum required thickness or design thickness
t_{sc}	Minimum required thickness plus corrosion allowance
Z	$= \frac{SE+P}{SE-P}$

Maximum Stress

When comparing Equation B.1 and Equation B.2, it is clear that the circumferential stress, for this case, will always be greater than the longitudinal stress.

The minimum required thickness for the thick wall vessel can be assumed to be that required by circumferential stress (Equation B.3). The equations for thick walled vessels are found in the BPVC, Section VIII, Division 1, Appendix 1-1.

Circumferential Stress

$$\begin{aligned} t &= R_i \left(Z^{1/2} - 1 \right) \\ &= (1.625) \left(\sqrt{\frac{(10000)(1) + (3000)}{(10000)(1) - (3000)}} - 1 \right) \text{ [in.]} \left[\frac{\text{psi}}{\text{psi}} \right]^{1/2} \\ &= 0.5895 \text{ in.} \end{aligned} \tag{B.3}$$

The minimum thickness required is therefore 0.5895". Allowing for corrosion this becomes:

$t_{sc} = 0.6300$ in.

B.2.5 Bolt Loads

Nomenclature

A_m	Minimum bolting area
A_B	Minimum bolting area
b_0	Gasket seating width, $b_0 = \frac{w}{8}$
b	Effective gasket seating width, b = b_0 when w $\leq 1/4$"
D_B	Bolt circle diameter
d_B	Bolt diameter
d	Inside vessel diameter
G	Gasket mean diameter
m	Gasket seating factor
n	Number of bolts required
P	Design pressure
S_B	Design stress for bolting material
W_{M1}	Operating load
W_{M2}	Gasket seating force
w	O-ring width
y	Yield point stress

Maximum Bolt Load

When considering bolt loads there are two design conditions: (1) operating load (Equation B.4) and (2) gasket seating force (Equation B.5). The most

severe will be the resulting bolt load (BPVC, Section VIII, Division 1, Appendix 2-5). The inner diameter of the o-ring is 1/8" greater than the inside diameter of the vessel. The o-ring dimensions are outlined in Table B.6.

Table B.6 – Gasket dimensions and related bolt load calculation parameters

Buna-N O-Ring			
	Width	w	1/8 in.
	Inside diameter	ID	3.375 in.
	Mean diameter	G	3.500 in.
	Gasket seating width	b_0	1/64 in.
	Effective gasket seating width	b	1/64 in

1) Operating Load

$$\begin{aligned} W_{M1} &= \frac{\pi}{4}G^2P + 2b\pi GmP \\ &= \left(\frac{\pi}{4}(3.5)^2(3000) + 2(1/64)\pi(3.5)(1)(3000)\right)\left([\text{in.}]^2\ [\text{psi}]\right) \\ &= 29894\ \text{lb}_f \end{aligned} \tag{B.4}$$

2) Gasket Seating Force

$$\begin{aligned} W_{M2} &= \pi bGy \\ &= \left(\pi(1/64)(3.5)^2(900)\right)\left([\text{in.}]^2\ [\text{psi}]\right) \\ &= 155\ \text{lb}_f \end{aligned} \tag{B.5}$$

$W_{M1} < W_{M2}$, therefore the operating load dominates.

Minimum Bolting Area

The minimum bolting area is determined from W_{M1} by Equation B.6.

$$\begin{aligned} A_m &= \frac{W_{M1}}{S_B} \\ &= \frac{(29894)}{(10000)}\ \frac{[\text{lb}_f]}{[\text{psi}]} \\ &= 2.9894\ \text{in.}^2 \end{aligned} \tag{B.6}$$

Number of Bolts

The number of bolts required of a given size is determined by the ratio of the A_m to the area per bolt (Equation B.7). The solution is always rounded up to the nearest integer.

$$\begin{aligned} n &= \frac{A_m}{A_B} \\ &= \frac{4A_m}{\pi d_B^2} \end{aligned} \tag{B.7}$$

Using Equation B.7, Table B.7 summarizes the number of 316 stainless steel bolts required for some common bolt diameters.

Table B.7 – Number of bolts required for various bolt diameters

Bolt Diameter / in.	Number of Bolts Required	Actual Bolted Area / in.^{2}
1/2	16	3.142
5/8	10	3.068
3/4	7	3.093

Bolts larger in diameter than 3/4" are too big for the vessel and too many bolts are required to use 1/2" bolts. There are a total of 8 ports required around the circumference of the vessel. Having 8 bolts would allow for these ports to be spaced symmetrically around the circumference. Therefore a total of 8 bolts 3/4" in diameter will be used.

Bolt Circle

The minimum bolt circle diameter is determined by Equation B.8.

$$\begin{aligned} D_B &= d + 2t_{sc} + d_B \\ &= (3.25) + 2(0.6300) + (0.75) \text{ [in.]} \\ &= 5.2600 \text{ in.} \end{aligned} \tag{B.8}$$

B.2.6 Reinforcement of Openings in a Pressure Vessel

Nomenclature

arc	Actual centre to centre distance between openings
arc_{min}	Minimum centre to centre distance between two unreinforced radial openings
$d_{o,i}$	Nominal diameter of opening i
r_{total}	Total radius of the vessel
θ	Radial angle between openings

TEM Stage Vessel Openings

There are a total of 8 radial and 2 axial holes required for this vessel. The dimensions and function of these ports are outlined in Table B.8.

Table B.8 – Openings in the TEM Stage Vessel

Thread Size	Nominal Size / in.	Quantity	Description
Radial			
1/8" NPT	0.405	2	RTD probe, surrounding temperature measurement
1/8" NPT	0.405	1	Gas in
1/8" NPT	0.405	1	Gas out
1/8" NPT	0.405	1	Pressure measurement
1/8" NPT	0.405	1	Plug
1/4" NPT	0.540	2	Power lead gland fittings, TEM and thermistor wire sealing
Axial			
1"NPT	1.315	2	Top and bottom sight windows

Rules concerning openings in pressure vessels were taken from the BPVC, Section VIII, Division 1, Part UG-36.

Radial Openings

The minimum distance between two unreinforced openings (1 and 2) is given by Equation B.9. Since there are 8 ports space symmetrically, the centre to centre angle will be 45°.

$$arc_{min} = (1 + 1.5 \cos \theta)(d_{o,1} + d_{o,2}) \tag{B.9}$$

The minimum distance between 1/8" NPT and 1/4" NPT openings:

$$\begin{aligned} arc_{min} &= (1 + 1.5\cos\theta)(1/8\text{" NPT} + 1/4\text{" NPT}) \\ &= \left(1 + 1.5\cos\left(45\left[\frac{\pi}{180}\right]\right)\right)(0.405 + 0.540)\text{ [in.]} \\ &= 1.9473\text{ in.} \end{aligned} \tag{B.10}$$

The minimum distance between 1/8" NPT and 1/8" NPT openings:

$$\begin{aligned} arc_{min} &= (1 + 1.5\cos\theta)(1/8\text{" NPT} + 1/8\text{" NPT}) \\ &= \left(1 + 1.5\cos\left(45\left[\frac{\pi}{180}\right]\right)\right)(0.405 + 0.405)\text{ [in.]} \\ &= 1.6691\text{ in.} \end{aligned} \tag{B.11}$$

The actual distance between openings:

$$\begin{aligned} arc &= \theta r_{total} \\ &= \left(45\left[\frac{\pi}{180}\right]\right)(3.500)\text{ [in.]} \\ &= 2.7489\text{ in.} \end{aligned} \tag{B.12}$$

Therefore extra material is not required for the radial openings.

Axial Openings

Openings in flat circular heads are restricted to a maximum of half the shortest unsupported length ($d/2$). If the opening is larger than one quarter of the shortest unsupported length ($d/4$), extra material is required to compensate for the opening. For both the top and the bottom openings, the shortest unsupported length is 3.25". From Table B.8, the nominal diameter of each axial opening is 1.315". Since $d/2 > 1.315\text{"} > d/4$, the openings are not too large but require reinforcing.

The method described in part UG-39(d) will be used to reinforce the openings. When calculating the minimum thickness for the lid and the bottom, replace the coefficient C with 2C for both.

B.2.7 Flat Heads

Nomenclature

C	a factor depending on the method of attachment
d	vessel inside diameter
d_e	diameter or short span (dependent on the method of attachment)
E	Weld joint efficiency
h_G	Gasket moment arm
P	Design pressure
S	Design stress of body material
t_b	Minimum thickness of the bottom flat head
t_{bc}	t_b plus corrosion allowance
t_t	Minimum thickness of the top flat head
t_{tc}	t_t plus corrosion allowance
t	Minimum required shell thickness
t_{total}	Total shell thickness

Flat head calculations follow the method outlined in the BPVC, Section VIII, Division 1, Part UG-34.

Vessel Lid

The lid design corresponds to sketch (k), a bolted flange with a narrow gasket (part UG-34 of the BPVC). The minimum thickness (Equation B.13) it the greater of that required by the operating load (Equation B.4) or gasket seating (Equation B.5). In subsection B.2.5, it was determined that the operating load dominates. The value for the constant C in Equation B.13 is 0.3. Additional material is required from subsection B.2.6, C in Equation B.13 was replace with 2C. For this type of head parameter d_e corresponds to the mean gasket diameter. The moment h_G is the difference between the mean gasket radius and the bolt circle radius as shown in Figure B.2. The minimum thickness is then:

$$\begin{aligned} t_t &= d_e\sqrt{\frac{2CP}{SE} + \frac{1.9W_{M1}h_G}{SEd_e^3}} \\ &= 3.5\sqrt{\frac{(0.6)(3000)}{(10000)(1)} + \frac{1.9(29894)(0.8800)}{10000)(1)(3.5)^3}}\ [\text{in.}]\left[\frac{[\text{psi}]}{[\text{psi}]}\right]^{1/2} \\ &= 1.9061 \text{ in.} \end{aligned} \tag{B.13}$$

Including the corrosion allowance, the minimum thickness will be:

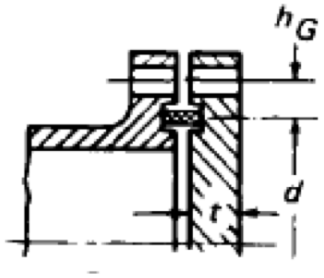

Figure B.2 – Schematic of a bolted flat head with a narrow-faced gasket showing the h_G edge moment.

$t_{tc} = 1.9461$ in.

Vessel Bottom
The bottom of the vessel corresponds to sketch (b-2) a forged circular head integral with the vessel (part UG-34 of the BPVC), shown in Figure B.3.

This type of head also requires that the inner joint between the body and the head be curved. The radius depends on the total shell thickness. For $t_{total} \leq 1.5$" the radius is 0.375", else the radius is equal to $0.25t_{total}$ but need not be larger than 0.75". This vessel will be machined out a 7" diameter cylinder; t_{total} will be 1.875", therefore the radius is given by:

$$\begin{aligned} r_b &= 0.25t_{total} \\ &= 0.25(1.875) \text{ [in.]} \\ &= 0.4690 \text{ in.} \end{aligned} \tag{B.14}$$

The minimum thickness is determined by Equation B.15. The value of C for this type of head is $0.33t/t_{total}$ with a minimum value of 0.20.

$0.33t/t_{total} = 0.111$
Therefore, C = 0.20

Since, additional material is required from subsection B.2.6, C was replaced by 2C in Equation B.15. The parameter d_e for this type of head corresponds to the vessel inside diameter.

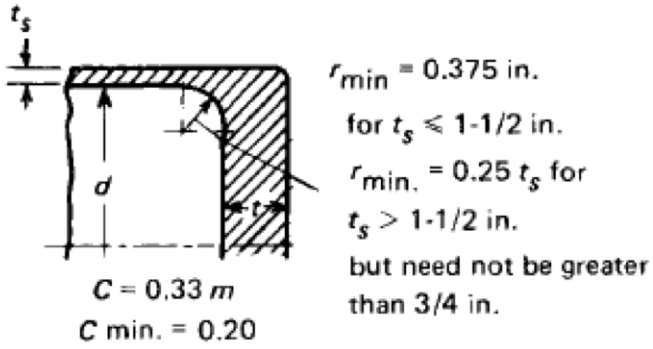

Figure B.3 – Schematic of an integral flange head.

$$\begin{aligned} t_b &= d_e\sqrt{\frac{2CP}{SE}} \\ &= 3.25\sqrt{\frac{(0.4)(3000)}{(10000)(1)}}\ [\text{in.}]\left[\frac{[\text{psi}]}{[\text{psi}]}\right]^{1/2} \\ &= 1.1258 \text{ in.} \end{aligned} \tag{B.15}$$

Including the corrosion allowance, the minimum thickness will be 1.1658". However, this is less than the total thickness of the shell body (1.875"). Part UG-34 of the BPVC requires that the thickness of the plate be greater than that of the shell. To compensate for this, t_{bc} is rounded to 2.000".

$t_{bc} = 2.000$ in.

B.3 Summary

Table B.9 – Summary of pressure vessel calculations

Vessel Body	
Material	316 Stainless Steel
Outside diameter	7.0000 in.
Inside diameter	3.2500 in.
Minimum wall thickness	0.6300 in.
Bolts	
Material	316 Stainless Steel
Size	3/4" - 16
Number	8
O-ring	
Material	Buna-N
Width	0.125 in.
Inside diameter	3.375 in.
Openings	
Radial openings	8
Axial openings	2
Vessel Heads	
Top plate thickness	1.9461 in.
Bottom plate thickness	2.0000 in.

B.4 Drawings

B.4.1 Pressure Vessel Body

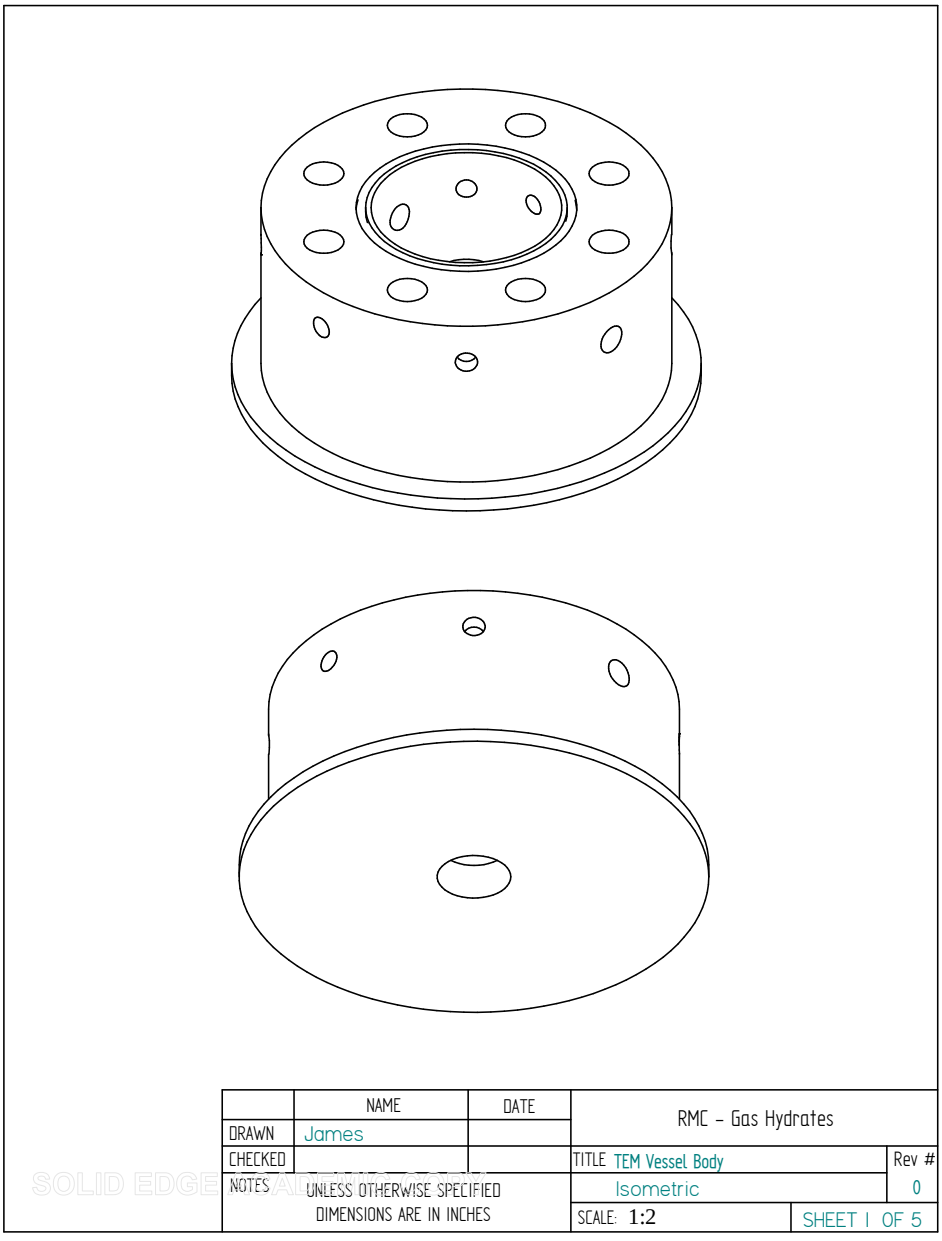

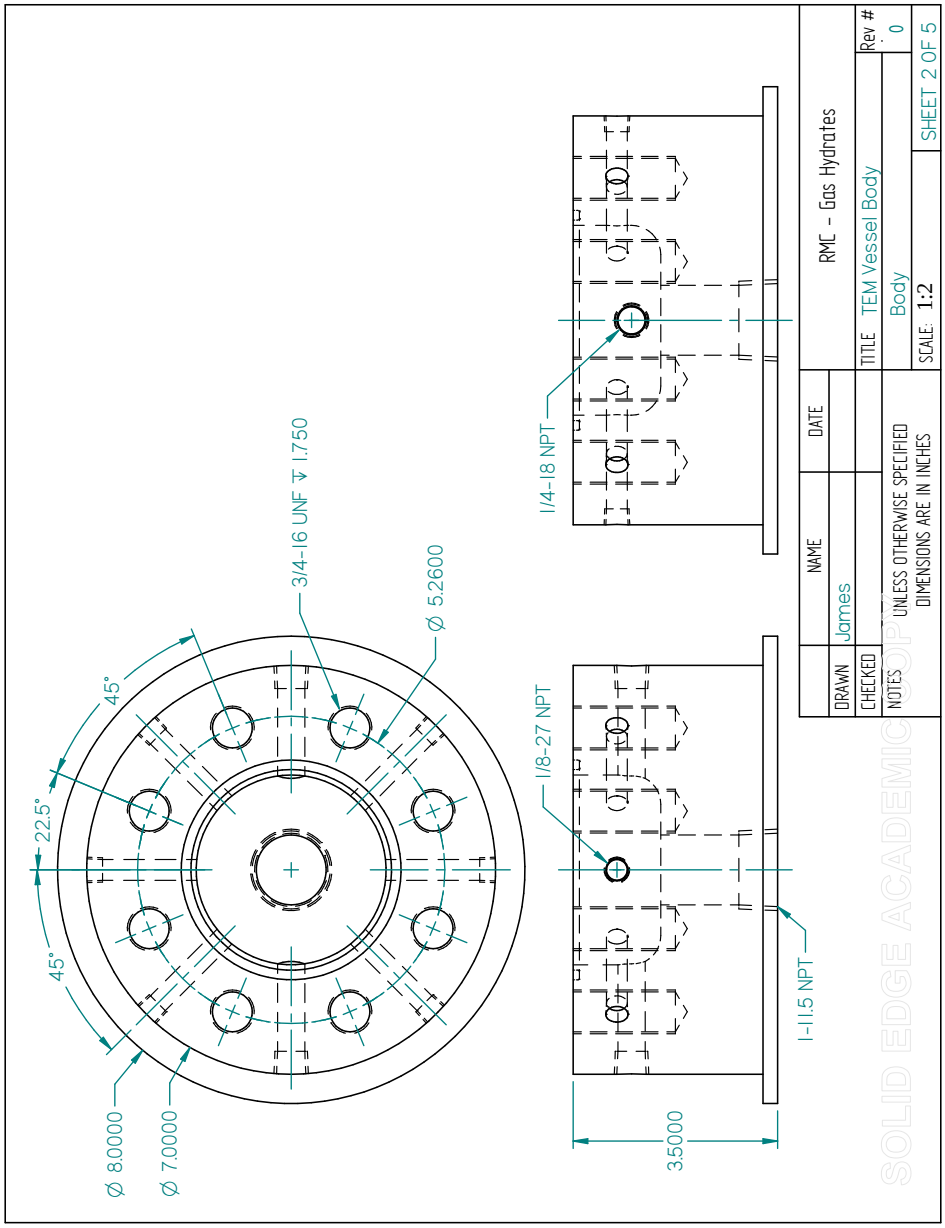
3/4-16 UNF ↧ 1.750
Ø 5.2600
45°
22.5°
45°
Ø 8.0000
Ø 7.0000
1/4-18 NPT
1/8-27 NPT
1-11.5 NPT
3.5000
RMC - Gas Hydrates
NAME
DATE
DRAWN
James
CHECKED
NOTES
UNLESS OTHERWISE SPECIFIED
DIMENSIONS ARE IN INCHES
TITLE TEM Vessel Body
Body
SCALE: 1:2
Rev # 0
SHEET 2 OF 5
SOLID EDGE ACADEMIC COPY

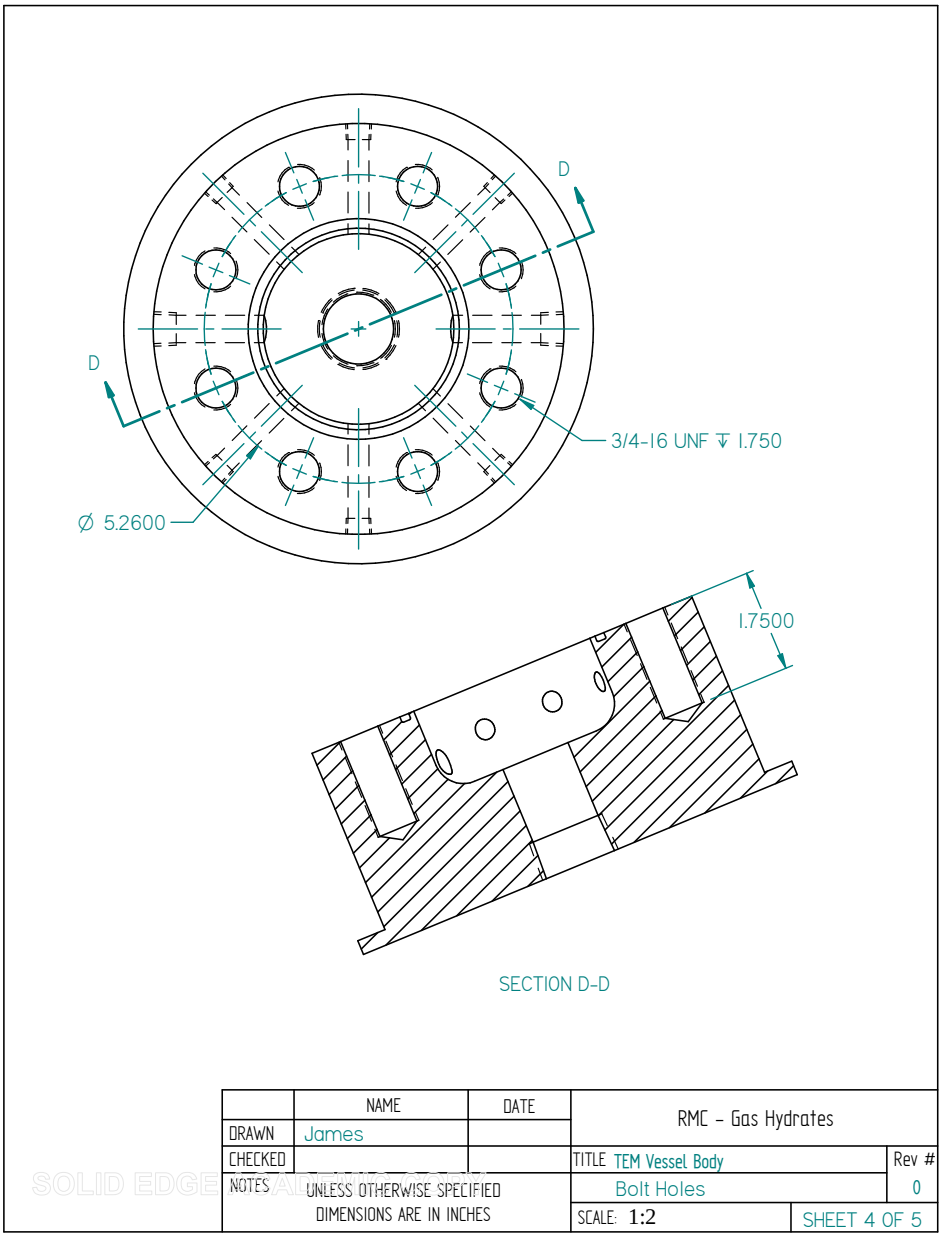

	NAME	DATE	RMC - Gas Hydrates	
DRAWN	James			
CHECKED			TITLE TEM Vessel Body	Rev #
NOTES	UNLESS OTHERWISE SPECIFIED DIMENSIONS ARE IN INCHES		Bolt Holes	0
			SCALE: 1:2	SHEET 4 OF 5

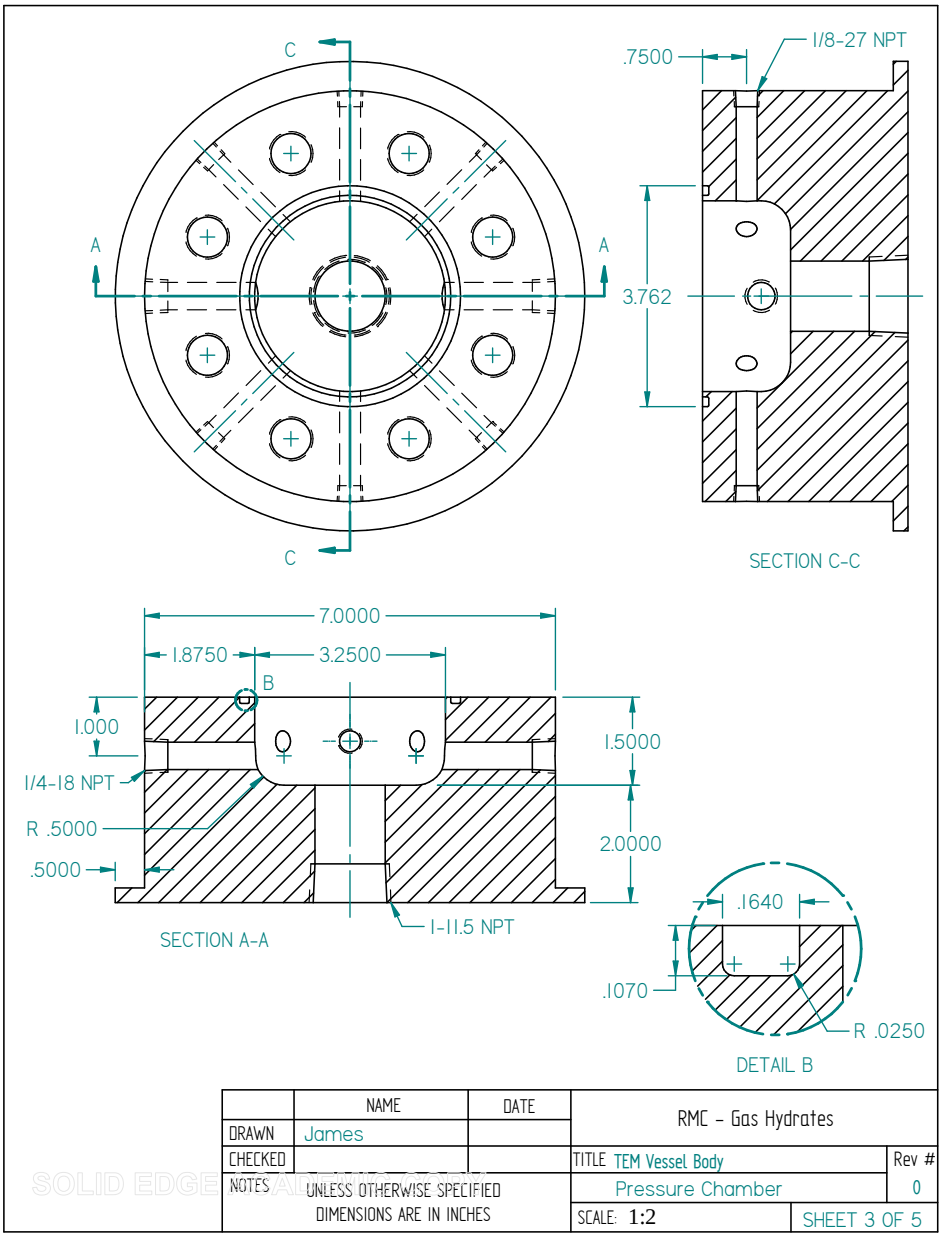
C
A
A
C
.7500
1/8-27 NPT
3.762
SECTION C-C
7.0000
1.8750
3.2500
B
1.000
1.5000
1/4-18 NPT
R .5000
.5000
2.0000
1-11.5 NPT
SECTION A-A
.1640
.1070
R .0250
DETAIL B
NAME
DATE
DRAWN
James
CHECKED
NOTES
UNLESS OTHERWISE SPECIFIED
DIMENSIONS ARE IN INCHES
RMC - Gas Hydrates
TITLE TEM Vessel Body
Rev #
Pressure Chamber
0
SCALE: 1:2
SHEET 3 OF 5

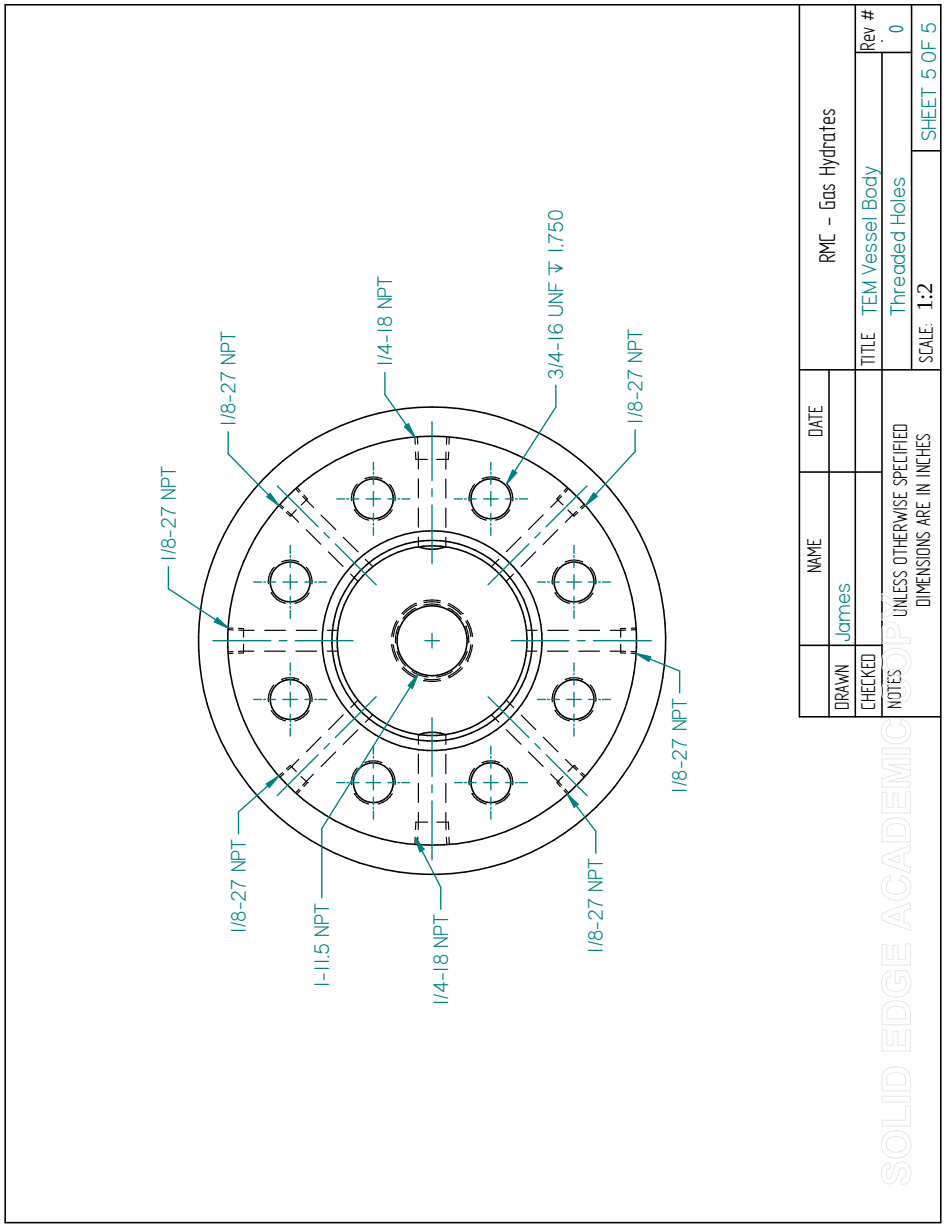
1/8-27 NPT
1/8-27 NPT
1/4-18 NPT
3/4-16 UNF ∓ 1.750
1/8-27 NPT
1/8-27 NPT
1/8-27 NPT
1-11.5 NPT
1/4-18 NPT
1/8-27 NPT
RMC - Gas Hydrates
NAME
DATE
DRAWN
James
CHECKED
NOTES:
UNLESS OTHERWISE SPECIFIED
DIMENSIONS ARE IN INCHES
TITLE TEM Vessel Body
Threaded Holes
Rev # 0
SCALE: 1:2
SHEET 5 OF 5
SOLID EDGE ACADEMIC COPY

B.4.2 Pressure Vessel Lid

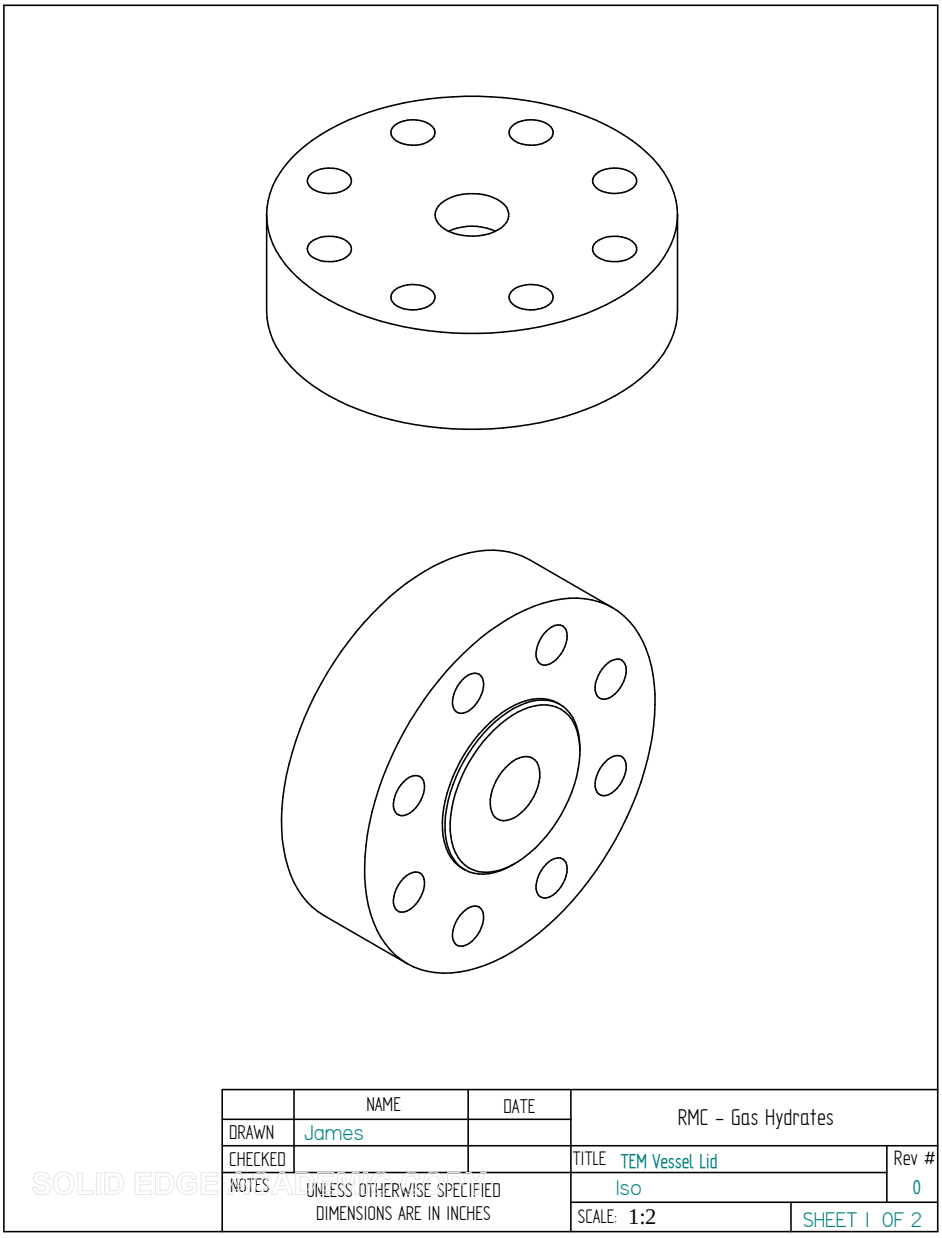

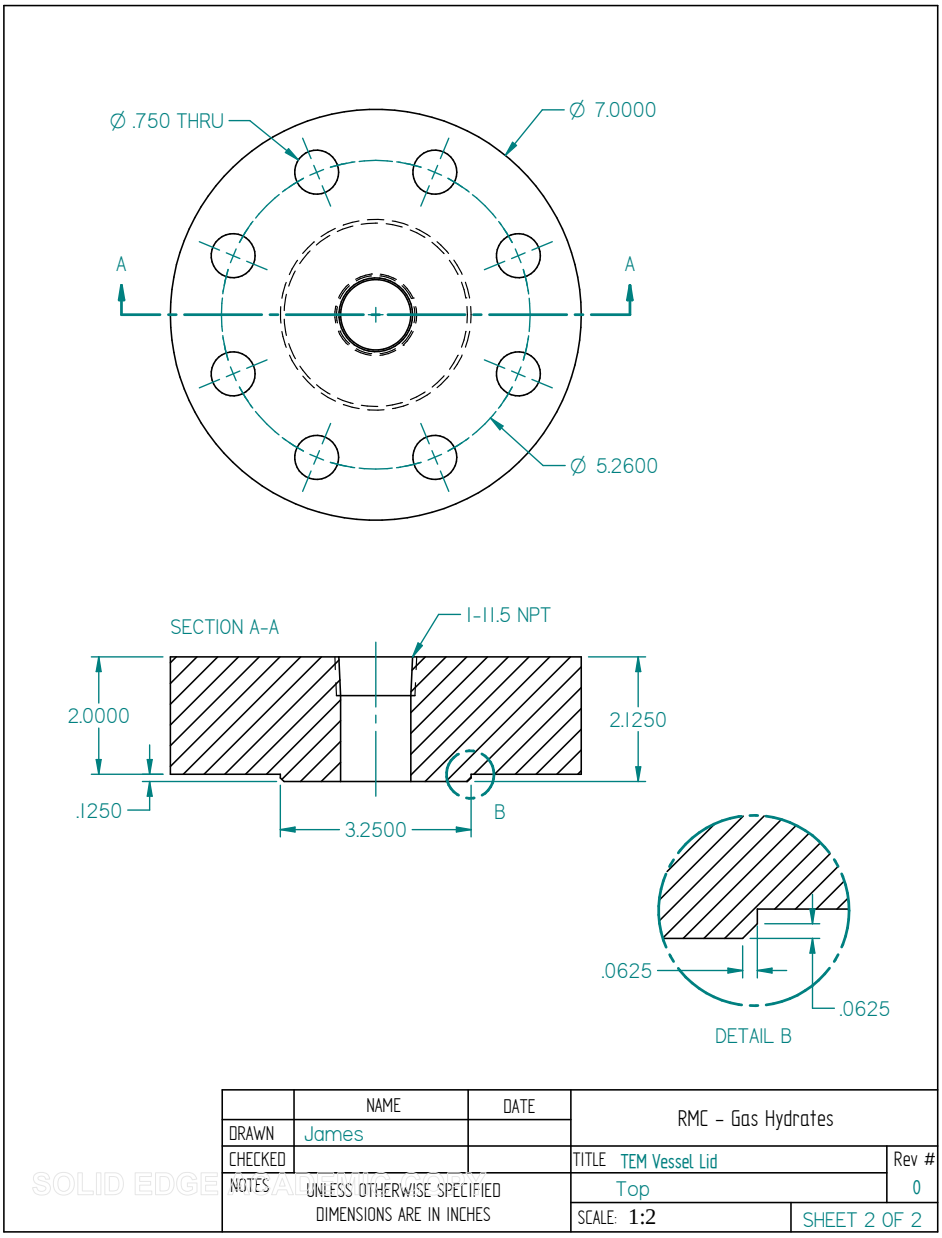
Ø .750 THRU
Ø 7.0000
A
A
Ø 5.2600
SECTION A-A
1-11.5 NPT
2.0000
2.1250
.1250
3.2500
B
.0625
.0625
DETAIL B
NAME
DATE
DRAWN
James
CHECKED
NOTES
UNLESS OTHERWISE SPECIFIED
DIMENSIONS ARE IN INCHES
RMC - Gas Hydrates
TITLE TEM Vessel Lid
Rev #
Top
0
SCALE: 1:2
SHEET 2 OF 2